Kaunas University of Technology
Faculty of Mathematics and Natural Sciences

Pilot Study of 3D Printable PMMA for Medical Physics Applications

Master's Final Degree Project

Maria Rosa Rojas Noguera
Project author

Assoc. Prof. Benas Gabrielis Urbonavičius

Supervisor

Kaunas, 2025

Kaunas University of Technology

Faculty of Mathematics and Natural Sciences

Pilot Study of 3D Printable PMMA for Medical Physics Applications

Master's Final Degree Project

Medical Physics (6213GX001)

Maria Rosa Rojas Noguera

Project author

Assoc. Prof. Benas Gabrielis Urbonavičius

Supervisor

Assoc. Prof. Brigita Abakevičienė

Reviewer

Kaunas, 2025

Kaunas University of Technology

Faculty of Mathematics and Natural Sciences

Maria Rosa Rojas Noguera

Pilot Study of 3D Printable PMMA for Medical Physics Applications

Declaration of Academic Integrity

I confirm the following:

1. I have prepared the final degree project independently and honestly without any violations of the copyrights or other rights of others, following the provisions of the Law on Copyrights and Related Rights of the Republic of Lithuania, the Regulations on the Management and Transfer of Intellectual Property of Kaunas University of Technology (hereinafter – University) and the ethical requirements stipulated by the Code of Academic Ethics of the University;

2. All the data and research results provided in the final degree project are correct and obtained legally; none of the parts of this project are plagiarised from any printed or electronic sources; all the quotations and references provided in the text of the final degree project are indicated in the list of references;

3. I have not paid anyone any monetary funds for the final degree project or the parts thereof unless required by the law;

4. I understand that in the case of any discovery of the fact of dishonesty or violation of any rights of others, the academic penalties will be imposed on me under the procedure applied at the University; I will be expelled from the University and my final degree project can be submitted to the Office of the Ombudsperson for Academic Ethics and Procedures in the examination of a possible violation of academic ethics.

Maria Rosa Rojas Noguera

Confirmed electronically

Rojas Noguera, Maria Rosa. Pilot Study of 3D Printable PMMA for Medical Physics Applications. Master's Final Degree Project/ supervisor Assoc. Prof. Benas Gabrielis Urbonavičius; Faculty of Mathematics and Natural Sciences, Kaunas University of Technology.

Study field and area (study field group): Medical Technologies (Health Sciences).

Keywords: 3D printing, PMMA, Quality Assurance, CT phantom, Hounsfield Units (HU), Additive manufacturing, Phantom Design.

Kaunas, 2025. 84.

Summary

This pilot study investigates the feasibility of using Polymethyl Methacrylate (PMMA) filament and Fused Deposition Modeling (FDM) technology to build a medical physics phantom motivated by the growing demand for cost-effective, customizable, available alternatives to commercial phantoms used in quality assurance (QA) and quality control (QC) protocols in medical imaging. In this study, PMMA was selected given its favorable radiological characteristics, proved suitability for radiological imaging applications, and compatibility with FDM printing technology. A printing protocol developed for 100% infill printing of PMMA in a FDM Zortrax M300 was followed but various printing challenges such as warping, layer adhesion failures, and thermal stability were encountered which led to limited printable dimensions achievable in the z axis. A radiological evaluation was performed for assessment of the samples attenuation properties in terms of achievable Hounsfield Units (HU) within the soft-tissue-equivalent range. Although greater variability compared to their commercial counterpart was observed, no high-density structure was identified in the prints, contradicting earlier observations that were likely due to CT imaging border artifacts. Additionally, the presence of air pockets observable in the Ct images highlights the potential for printing internal air cavities which could be beneficial in future designs. The study outlines the technical limitations related to printability and structural integrity of 100% infill FDM AM using PMMA whilst also provides practical recommendations for future research including dimension constraints, material behavior under CT, and printing and scanning environments considerations.

Maria Rosa, Rojas Noguera. Bandomasis 3D spausdinamo PMMA bandomasis tyrimas medicinos fizikos reikmėms. Magistro krypties studijų baigiamasis projektas / vadovas doc. dr. Benas Gabrielis Urbonavičius; Kauno technologijos universitetas, Matematikos ir gamtos mokslų fakultetas.

Studijų kryptis ir sritis (studijų krypčių grupė): Medicinos technologijos (Sveikatos mokslai).

Reikšminiai žodžiai: 3D spausdinimas, PMMA, kokybės užtikrinimas, kompiuterinės tomografijos fantomas, Hounsfieldo vienetai (HU), pridėtinė gamyba, fantomo dizainas.

Kaunas, 2025. 84 p.

Santrauka

Šiame bandomajame tyrime tiriamos galimybės naudoti polimetilmetakrilato (PMMA) termoplastiką ir trimačio spausdinimo technologiją medicinos fizikos fantomui sukurti, nes didėja ekonomiškai efektyvių, pritaikomų, prieinamų alternatyvų komerciniams fantomams, naudojamiems kokybės užtikrinimo (KĮ) ir kokybės kontrolės (KK) protokoluose medicininių vaizdų srityje, poreikis. Šiame tyrime PMMA buvo pasirinktas atsižvelgiant į jo palankias radiologines savybes, įrodytą tinkamumą radiologiniams vaizdams gauti ir suderinamumą su FDM spausdinimo technologija. Buvo laikomasi sukurto spausdinimo protokolo, skirto 100 % užpildui iš PMMA spausdinti FDM Zortrax M300, tačiau buvo susidurta su įvairiomis spausdinimo problemomis, tokiomis kaip deformacijos, sluoksnių sukibimo sutrikimai ir terminis stabilumas, dėl kurių buvo pasiekti riboti spausdintini matmenys z ašyje. Atliktas radiologinis įvertinimas, siekiant įvertinti bandinių slopinimo savybes, išreikštas pasiekiamais Hounsfieldo vienetais (HU) minkštųjų audinių ekvivalento diapazone. Nors pastebėtas didesnė savybių variacija, palyginti su komerciniais analogais, atspauduose nenustatyta didelio tankio struktūros, o tai prieštarauja ankstesniems pastebėjimams, kurie greičiausiai buvo susiję su kompiuterinės tomografijos vaizdavimo ribų artefaktais. Be to, KT vaizduose pastebėtos oro ertmės išryškina galimybę spausdinti vidines oro ertmes, kurios galėtų būti naudingos būsimiems projektams. Tyrime aprašomi techniniai apribojimai, susiję su 100 % užpildo FDM AM spausdinimo galimybėmis ir struktūriniu vientisumu naudojant PMMA, taip pat pateikiamos praktinės rekomendacijos būsimiems tyrimams, įskaitant matmenų apribojimus, medžiagos elgseną veikiant kompiuterinei tomografijai ir spausdinimo bei skenavimo aplinkos aspektus.

Table of contents

List of Figs

List of tables

List of abbreviations and terms

Abbreviations:

AM – Additive Manufacturing;

CBCT – Cone Beam Computed Tomography;

CT – Computed Tomography;

FDM – Fused Deposition Modeling;

HU – Hounsfield Unit;

IAEA – International Atomic Energy Agency;

PMMA – Polymethyl Methacrylate;

QA – Quality Assurance;

QC – Quality Control;

ROI – Region of Interest;

RT – Radiation Therapy

3D – Three-dimensional.

Terms:

Voxel – Volumetric pixel (3D unit in medical imaging).

Infill – Internal density pattern in 3D printed objects.

Edge Artifact – Artificial signal at boundaries in CT imaging caused by a reconstruction or partial volume effects.

Introduction

The term phantom is often used to refer to a model that resembles the human body [1]. More precisely, in medical physics, a phantom not only shall resemble the body anatomy but also its radiological properties and behavior. Water has been the choice for most studies due to its affinity to soft tissue and reproducible radiation properties and availability [2, 3]. Ideally, medical physics phantoms must have similar radiological properties than the anatomic structure it mimics. In recent years, the advance of AM has introduced new opportunities for medical physics applications and has proven its suitability for modeling of medical images, helping identify abnormalities, teaching, and learning [4]. As medical institutions look for cost-effective alternatives to expensive commercial phantoms, 3D printing has emerged as a promising tool to support this goal. 3D printing offers, also, the advantage of customizable pieces, overcoming traditional manufacturing fixed geometries [5]. PMMA is one of the most widely used materials in medical imaging and dosimetry as it exhibits favorable radiological behavior and tissue equivalent attenuation properties [6] and it was the first to be recommended by the IAEA [7]. PMMA stands for polymethyl methacrylate, and it is currently used in quality assurance programs in radiotherapy. In 3D printing context, PMMA is compatible with additive manufacturing and fused deposition modelling, a 3D printing technology available in our lab. These characteristics make PMMA the ideal candidate for exploring the feasibility of 3D printing phantoms using FDM technology.

Computed tomography scan, commonly known as CT, is a radiological imaging study that granted physicist Allan MacLeod Cormack and electrical engineer Godfrey Hounsfield the Nobel Prize in Physiology or Medicine in 1979 [8]. This image modality stands out for materials evaluation due to its sensitivity to structural details and density variations. The suitability of a 3D printed sample can be evaluated based on its CT imaging which allows us to assess its radiological consistency, and Hounsfield Unit (HU) values. Therefore, a PMMA 3D printed phantom calls for 100% infill density as internal air gaps could lead to inhomogeneities that may be perceived by the CT scan and make it unsuitable for the study. Commercially available PMMA phantoms exhibit excellent homogeneity in its structure. However, studies have shown that relying on 100% infill in FDM printing may increase porosity and reduce structural integrity making fine tuning of the printing settings an exhausting and outmost necessary task [9]. This pilot study aims to evaluate the feasibility of printing a medical physics phantom using PMMA filament via Fused Deposition Modeling, with specific focus on achieving CT imaging performance including HU values and homogeneity that approaches commercial phantom standards while also identifying technical limitations in the printing fabrication process.

Aim: to develop a practical approach to 3D printable PMMA for medical and scientific applications.

Tasks:

1. Analyze potential use cases for 3D printable phantom in medical physics.

2. Develop a protocol designed for 3D printing PMMA for various geometries relevant in medical and scientific applications and validate it with a pilot study.

3. Test applicability of homogenous fillers for composite phantom structures for dosimetric and quality assurance procedures.

1. Literature review

Mosby's Medical Dictionary defines phantom as "a mass of material similar to human tissue used to investigate the effect of radiation beams on human beings." [10] This definition clearly differentiates an anatomical educational model commonly used as a visual representation of the body and a phantom, by stating that a phantom is used in at least one medical application using radiation. The structural characteristics and the material composition of a phantom strictly depend on the purpose it is meant to serve. Features like size and shape can vary drastically from one model to another. Phantoms can be as complex or as simple as the anatomic part they represent. In certain cases, a detailed internal anatomy would be superfluous, while in others, detailed internal structures are necessary to accurately simulate the procedure of concern [10]. Anthropomorphic phantoms, as the name state, are designed to closely resemble the shape, and sometimes size, of the human body. These phantoms can be highly detailed and simulate males, females, adults or children anatomy. Whereas other simplistic geometries such as the computed tomography dose index (CTDI) measurements phantom display simple shapes.

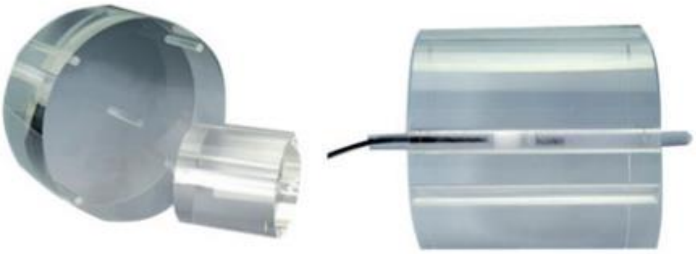

(a)

(b)

Fig. 1 (a) Head and Body CT dosimetric phantom (b) Anthropomorphic phantom resembling a human male body [10]

With the discovery of X rays by Roentgen, researchers threw themselves into applications for radiation phenomena. In the medical field, and after the consequences of radiation exposure were unveiled, people were reluctant to volunteer to receive radiation for experimental reasons. There are two branches of the use of radiation in the medical field: therapy and diagnostic. As defined by the Cancer Research Institute of the United Kingdom, "radiotherapy means the use of radiation, usually x-rays, to treat cancer"[11]. Radiation therapy is mostly used to try to cure cancer, reduce the chance of cancer coming back, or help relieve disease symptoms. The second branch of radiation use in medicine, diagnostic, permits physicians to view the body's parts [12]. The influence of radiation in medicine relies on the capability of X-rays to penetrate objects, deposit energy, and/or produce images representing structures within the body or even anatomical functions. Safety and accuracy, two outstanding discussion topics in medical physics, rely on the use of phantoms cable of mimic the response of the human body to a radiation field as radiation dose cannot be directly measured in patients for ethical reasons.

The common method to assess the dose delivered to a patient during a CT scan procedure can usually be performed in two different ways: direct measurements in a physical phantom or simulation in a "virtual patient" using commercially available software. In the direct measurement method, a physical CT phantom is required and implemented during the procedure. Dosimeters are placed within the phantom's cavities, and it is later irradiated by a CT scanner [13]. Dose measures as well as other features, are then assessed and compared to approved international standards that validate the correct functioning of the imaging machine, the operational safety and verification that the scanner accurately reproduces the scanned subject, ensuring no unintended information is added or omitted in the final images.

Suboptimal performance of the CT scanner device is not consistent with the ALARA principle (As Low as Reasonably Achievable) as it promotes misdiagnosis and artifacts that may lead to over exposure. Moreover, it can compromise the well-being of the patient and subject it to unnecessary extra dose. Thus, quality assurance, and therefore medical radiation phantoms, should be of outmost interest in any radiation therapy or imaging institution.

Whilst in the beginning the main focus of phantom development was for dosimetry purposes, a number of phantoms for imaging systems were as well fabricated. Mammography phantoms can be traced back to the 1970s but literature shows evidence of imaging phantoms existence as early as the 1940s [10]. The relevance and importance of tissue mimicking devices is demonstrated in **Fig. 2** which shows the number of articles from 1992 to 2022 listed in Scopus and published in English with the terms phantom and imaging for a total of 8,688 [14].

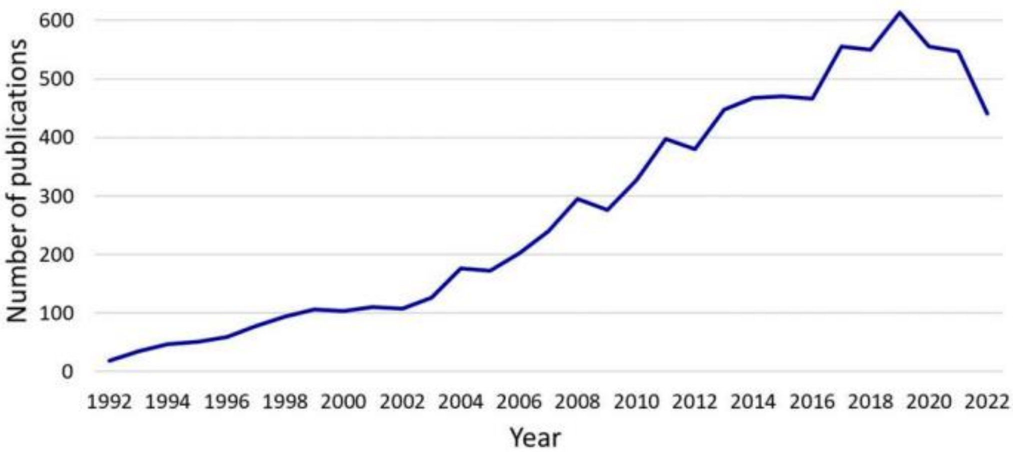

Fig. 2 Research articles with the terms phantom and imaging published per year between 1992 and 2022 listed in the Scopus database [14]

A phantom is not a term limited to the human body and can also be the model of an animal. Weather motivated by dosimetry, calibration, or quality assurance, the purpose is always to control and evaluate the imaging or treatment procedure. Education and training, new technologies investigations, simulations, and developments of new measurements devices are also listed in phantom purposes. Clinical and preclinical trials often rely on them for simulations on human-free environments that also avoid animal testing.

In 1986, the European Organization for Research and Treatment of Cancer (EORTC), launched its first QA program [15]. The study covered 17 institutions evaluated in terms of dosimetric intercomparison and dose assessment on anatomical phantoms [16, 17]. A final report published by Horiot et al in 1993 [18] describes the minimum requirements for QA in radiotherapy. In modern times, virtual phantoms are often used in computer simulations or in conjunction with physical ones. Nevertheless, physical tests for validation are still unavoidable [14]. This cutting-edge technology allowed for the development of current treatment planning systems (TPS) born in the need of easy access to radiotherapy services. TPS results must always be sustained by a medical physicist or other expert in the field, and the strength of such systems relies on two main points: the robustness of the dose calculation algorithm and the quality of the contouring software [15].

1.1. Relevant materials in medical phantoms

The one decisive factor in the designing and choosing of the materials for the phantom fabrication is the purpose the phantom is to serve. In general terms, phantoms are intended to emulate human tissue [19]. The material of choice, in the presence of incident radiation from the medical device, must behave in the same way or as similar as possible to the real human tissue. Nowadays, there are a variety of phantoms that serve various purposes in medical radiation. The simplest material for phantoms is water and it was the first tissue equivalent material used for radiation measurements as it has unit density similar to human body [19]. The reason for this is quite simple, water is generally easily available, inexpensive, and its density can be maintained with satisfactory accuracy in any shape and size of containers. Furthermore, the human body is made of 70% of water with an effective atomic number of 7.42 [19]. In most dose measurement methods, water is accepted as the standard material for soft tissue equivalence [20].

Water is extensively used in homogeneous phantoms. This type of phantom is characterized by having uniform material composition for simulation of tissue providing uniform dose distribution. In these phantoms no inserts of other materials are present and are usually of basic geometric shapes and often used in quality assurance measurements. They are easily accessible and in many cases are made of radiation safe water-containers [21]. A disadvantage of homogeneous phantoms is that they are not able to represent human anatomy and structures [22].

Other water equivalent materials commonly used in the field are PMMA acrylic, polystyrene, and polymer gel. Polymethyl methacrylate (PMMA) is the preferred choice in commercially available phantoms given its response to radiation and robustness to physical extenuation. The composition of these materials and other water-equivalent phantom materials alternatives can be visualized in **Table 1**. Selection, characterization, testing, and evaluation of tissue mimicking materials is by itself an area of continuous active research among groups performing phantom studies.

Table 1. Composition of elements for water-equivalent phantom materials [19].

Materials	H	C	N	O	Cl	Ca	Mass density (Kg/m^3)	Zeff	N
PMMA Acrylic	8	60.0		32.0			1170	6.24	3.25
Polystyrene	7.7	92.3					1060	5.69	3.24
Solid Water	8.1				0.1	2.3	1042	8.06	3.34
Virtual Water	8.1	67.2	2.4	19.9	0.1	2.3	1070	8.06	3.48
Polymer Gel	10.42	10.45	2.44	76.68			1050	7.37	3.49
Water	11.19			88.81			1000	7.42	3.343

Whilst water still stands as a widely accepted phantom standard material, the radiation dose measurements calculated by the treatment planning systems (TPS) on patient's CT scans, shows to be different from the calculated in water phantoms this due to the heterogeneity natural of the body [19]. The International Atomic Energy Agency (IAEA) recommends in its Technical Repot Series 398 on Absorbed dose in External Beam Radiotherapy, the use of polymethyl methacrylate (PMMA) as a water substitute and it is currently most widely used in radiation dosimetry [7]. The agency recommendation is to perform the relative dose measurements necessary in water tank phantoms as they remarkably simulate soft tissue for most energies. Unfortunately, the calibration setting and preparation of the water tank phantoms for the equipment calibrations tend to be inconvenient and time consuming as they require filling, positioning and draining [23] and so, are usually used for quarterly or annual quality assurance tests. On the other hand, waterproof dosimeters are prone to be more expensive and less available. Radiochromic films and other dosimeters could step in to solve this dilemma, but they usually take longer to reveal, or present other features inconveniences.

The common alternative to water tank phantoms, solid phantoms, require assessment of the difference in absorption and scattering properties compared to its standard counterpart, this because of its impurities and possible inhomogeneities. Regulations on this matter tend to vary from international, national, and local regulatory entities and internal controls. Whilst the IAEA recommends an accuracy of 3% [24], the International Commission of Radiation Units (ICRU) states in its Report number 44 that correction factors are required if uncertainties are greater than 1% [25]. Studies have shown that common materials for solid phantom are not water equivalent and therefore require correction factors [26, 27].

Not only radio-medical applications may require human dummies, magnetic resonance Imaging or MRI holds a spot in the evaluation of the scanner's performance, image acquisition protocols and monitoring for these devices [21]. In this, images are generated by applying a strong magnetic field that causes protons in the body to align with the field. Then, pulsed radiofrequency current momentarily disturbs the alignment and, as the proton returns to the previous stage, it releases energy that is detected by the MRI sensors [28]. In some cases, contrast agents are administered to the patient to enhance image output. Magnetic resonance employs gels to achieve human tissue magnetic behavior in the construction of anthropomorphic phantoms [29]. Nickel chloride or other solutions can also fill some phantom structures given its highly MRI-visible characteristics.

The most recent comprehensive data set of the International Agency for Research on Cancer estimates that in 2020 the global burden of cancer (GLOBOCAN) was 19.3 million new cancer cases and projects that by 2040 at least 28.4 million cancer cases will be recorded [30, 31]. The radiation treatment planning process begins with performing a CT scan imaging of the compromise anatomical region to identify and delineate the target tumor and the organs at risk. While some people argue about the high dose delivered by CT scans, the benefit justifies the risk. Upon the installation of a new CT scanner, quality control of the medical imaging machine must be performed, and its performance and safety must be evaluated and pass the relevant regulatory requirements.

The European guidelines on quality criteria for computer tomography highlight the key parameters for assessing the performance of the CT scanner, such parameters can be assessed using suitable test phantoms. These measurements should be conducted regularly in order to guarantee the correct functioning of the scanner during its use. The European Guidelines on quality criteria for computed tomography include a list of the general principles associated with good imaging techniques and the physical parameters involved for good imaging performance [32]:

a) Test phantoms should allow you to check the mean CT number, uniformity, noise, spatial resolution, slide thickness, dose and position of the couch.

b) The accuracy of the CT number.

c) The linear relation between the measured CT number and the linear attenuation coefficient of each element of the scanned object.

d) CT number should be uniform within a narrow limit of a homogeneous body scan.

e) The noise, measured as the statistical fluctuation the CT number of a picture of a homogeneous body in an area of about 10% of the cross-sectional of the body, should be evaluated based on the medical problem studied and the patient dose considered reasonable.

f) Spatial resolution should be evaluated both at high and low contrast.

g) The slice thickness should not exceed certain deviation to avoid distorting effects.

h) CT number and uniformity should stay stable over time.

i) Deviations in the longitudinal position and backlash of the patient couch should also be evaluated and both criteria tolerances are set as ± 2 mm.

The American Association of Physicist in Medicine (AAPM) recommends measuring this performance parameter with separate phantoms [33] except for noise and uniformity. The American College of Radiology (ACR) and the IAEA Human Health Series number 19 state that to guarantee the correct performance of the CT scanner measurements of the CT number of multiple objects, contrast scale, contrast-to-noise ratio (CNR), spatial resolution, magnitude of image noise, and uniformity, are mandatory variables to be measured to accredit the status of the device [34, 35]. When talking about quality assurance in terms of image quality in computed tomography, there are three main parameters involved: detecting suboptimal performance using standardized metrics, guiding corrective actions, and ensuring feasibility within clinical constrains [34-36]. Multidetector CT QA protocols are well stablished [37] whilst those for cone-beam CT (CBCT) are still developing [38-41]. Emerging technologies like high resolution CT and photon-counting present challenges for the conventional QA metrics, specifically regarding spatial resolution which often exceeds the capabilities of the commonly used phantoms[36]. CBCT applicability over a wide range of departments like radiation therapy [42], surgery [43], interventional radiology [44], breast [45], and musculoskeletal imaging [46], makes it an elevated challenge to develop a general protocol. Efforts towards a general protocol for QA of CBCT include the SEDENTEXCT report [41], EFOMP-ESTRO-IAEA protocol [40], AAPM TG179 and TG238 [38, 39].

Suitable phantoms are key parameters in performance assessment. Oliveria et al studied 37 phantoms and found that only two of them measured all six image quality parameters [47]. The widely used ACR phantom relies partly on subjective assessments, and its size limits its applicability in CBCT [48, 49], other phantoms like the Catphan, offer a more quantitative approach but still holds limitations. The AAPM in its report TG238 recommends several approaches to overcome these gaps [39]. Efforts made to overcome these gaps can be seen in the development of updated phantoms that better suit the needs like the Corgi Phantom which displays a modular and configurable design that addresses these limitations and allows for dose and image quality evaluations on both MDCT and CBCT. It allows assessment of image uniformity, HU accuracy, spatial resolution, and cone-beam artifacts and includes automated software analysis to support routine clinical use [50]. The International Society of Radiographers and Radiological Technologist ISRRT has developed a guidance document on QA/QC in CT stating the standard image quality tests and the frequency of testing, using as references the computer tomography quality control manual of the American College of Radiology, the IAEA quality assurance program for computer tomography, the European guidelines on quality criteria for computed tomography, and the International Electrotechnical Commission’s evaluation and routine testing in medical imaging departments part 2-6, such guidance is displayed in **Table 2** together with specifications from the Lithuanian hygiene norm 78:2009.

Table 2. QA/QC tests in CT

QC test	Aim	Instrument	Measurement	Acceptance criteria	Frequency
Image noise [51]	Assess noise of images	Water phantom	SD of CT numbers (central ROI)	≤ ± 5 HU	Daily
Visual check of artifacts [51]	Early detection of artifacts	Water phantom	Visual screen	No artifacts visible	Daily
Patient-positioning accuracy (laser and table) [51]	Ensure laser light and slice position concurrence	Alignment phantom	Planned vs. laser cross	≤ ± 1 mm	Monthly
Slice thickness / collimation width [51]	Ensure accurate collimation-slice width during scanning	Slice width insert.	Measured vs. nominal	≤ 1 mm or ≤ 20% (whichever larger)	Monthly

Homogeneity CT numbers [51]	Evaluation of CT number homogeneity	QC cylindrical water phantom	Average density of central ROI and of 4 periphery ROIs	Δ ≤ ± 4 HU	Monthly
CT number Accuracy [51]	Ensure accuracy and reproducibility of CT numbers	Multi-material QC phantom	Water 0 ± 4 HU; Air −1000 ± 10 HU; Bone/Teflon +1000 ± 15 HU	As listed in measurements	Weekly
Contrast resolution [51]	Low contrasts resolution	Low contrast module	Visible 0.5% holes	≥ 6 of 7 holes visible	Weekly
Spatial resolution [52]	Evaluate the system ability to visualize the most distinct structure in size	QC phantom	Determining the minimal distinct structure on an axial image of 1-2 mm thickness using High resolution reconstruction	Not exceed 0,7 lp/mm or manufacturer's reference values	Monthly
Accuracy of CT table movement on Z axis [52]	Ensure accurate patient movement on Z axis during scanning	Ruler and a sandbag of recommended weight	Deviation of value during 300 mm craniocaudal and caudocranial CT table movement at 10 mm intervals	Must not exceed ±2 mm or manufacturer's reference values	Monthly
Artifact Interference [52]	Visualize artifacts prior to their interference	QC phantom with high atomic number structures mimicking high density anatomical structures	Check for artifacts on 10 mm axial image	Presence of all artifacts interfering with diagnostic information are recorded	3 months
Dosimetry – CTDI [51, 52]	Evaluate CTDI consistency with manufacturer's reference values	16 cm and 32 cm diameter phantoms and 10 cm CT pencil ionization chamber	Measurement using scanning parameters and exposure factors for all protocols (AEE is not to be used during QC)	Consistent with manufacturer's reference values and within DRLs	3 months

Precision of Measurements [52]	Ensure correct and reproducible measurements on images	QC phantom	Measurement of dimensions, distance, and densities on 10 mm axial image	Must not exceed ± 1 mm or manufacturer's reference values	Annually
Leakage Radiation [51]	Ensure patient and staff safety	Survey meter	Measurement of dose rate or total dose around gantry at 1 m	≤ 1 mGyh^{-1}	Annually
Phantom Backscatter [52]	Ensure patient and staff safety	Survey meter and special patient backscatter cylinder	Measurement of instantaneous dose rate 1 m from phantom at angles -90°, -45°, 0°, 45°, 90° around the gantry	Recommended values by national authorities	Annually

In addition to these core image quality and dosimetry evaluations, the ISRRT QA/QC guidance document also emphasizes daily checks of several other parameters which includes visual verification of restricted areas and pregnancy signals for radiation protection of the public and staff, ensure the correct functioning of red-light exposure indicators, door safety locks, gantry control systems, and CT table movement. Gantry tils, emergency stop functions, audiovisual communication systems, and acoustic signals should also be included in the operational safety checks. Alignment of the patient positioning laser and functioning of the cooling systems must be monitored. Whilst these parameters do not directly impact on the image quality, they are still essential for the safe and consistent clinical workflow [52]. Modern CT systems allow automated QC testing and self-diagnostic assessments. All measurements must be documented according to institutional and national regulations, the acceptance criteria must be based on both manufacturer specifications and regulatory standards, in some scenarios the frequency of the QC tests may depend on local, regional or national requirements.

A CT head and body phantom used in CT QA and QC protocols consist of a solid acrylic cylinder with 16 cm diameter for the head phantom, and 32 cm diameter for the body phantom. Unfortunately, the high cost of commercialized phantoms can be a deterring issue for resource-limited healthcare centers and oncology hospitals. The search for inexpensive or more affordable materials comparable to the PMMA standard has been widely investigated in the oncology field. The goal of potentially lowering the cost for facilities and thus reducing the overall expenses triggers debate in the scientific field. The development of alternatives for tissue mimicking and radiologically accurate components could represent a solution in access to QC for CT [53].

1.2. Traditional manufacturing vs. 3D printing

Additive manufacturing has been around for decades, though in its early days it was very expensive and not feasible for the general market or end users. This technology is said to have been officially born in 1983 when Charles W. Hull successfully printed a teacup on a stereolithography system which he himself built, and in 1989 Scott S. Crump at the company Stratasys, Inc., took the first steps towards the development of FDM printing technologies [54].

Contrary to traditional manufacturing which usually refers to subtractive manufacturing (SM) and formative manufacturing techniques where machines remove material through mechanical techniques or casted molds [55], In 3D-printing, a computer-aided design is translated into a three-dimensional object by slicing it into several two-dimensional plans where the layers of material are deposited [56]. Materials ranging from plastics, rubbers, ceramics, glass, concretes, and even metals are suitable to be use in AM. Despite this technology existing from decades ago, it is only in the lates 2010 when it has captured the attention of experts and the general public.

According to the Wohlers Associates report 2025, the global additive manufacturing industry grew 9.1%, reaching USD $21.9 billion, and by 2034 it is expected that it reaches $115 billion [57]. A detailed market review for this technology in ats subdivisions can be found in **Fig. 3.**

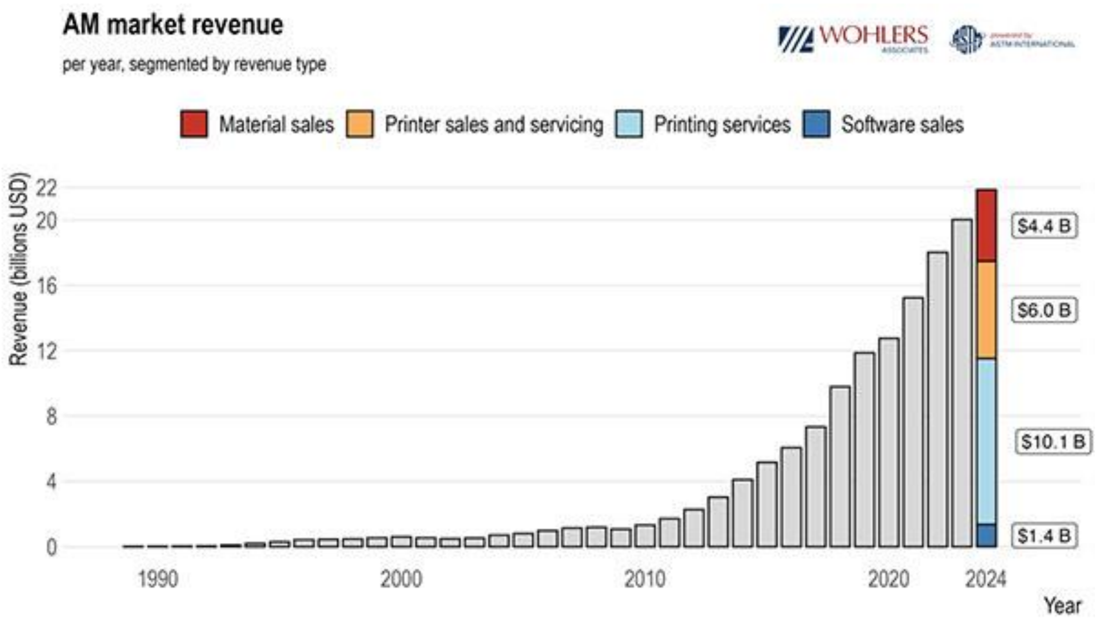

Fig. 3 AM market revenue per year [57]

Fundamentally, 3D printing consists of the formation of a full model part by successive printing of the layers that compose it. The workflow of the process starts by designing and generating a model of the object or structure to be created, usually using software tools like CAD. Then the file is exported as standard tessellation language (.stl) which converts the continuous geometry of the CAD generated geometry into small triangles [58]. The next steps consist of creating the 3D model into 2D slices that can be read by the printer, this is done through a model slicing software. The final digital product is accessed by the printer and the layering printing process beings [59].

An overview of the most used 3D printing technologies includes Fused Deposition Modelling (FDM), Direct Ink Writing (DIW), Selective Laser Sintering (SLS), Inkjet printing, Stereolithography (SLA) and other light-based systems, and Electron Beam Melting (EBM) [60]. The two most relevant printing technologies in the medical field are stereolithography (SLA) and fused deposition modelling (FDM). SLA is a high-end technology that uses lasers to cure layers or resin. It starts by lowering the platform in a tank filled with the liquid photopolymer resin, the platform is placed precisely at layer high level above the surface. Then galvanometers direct the UV laser through a transparent window at the bottom of the resin tank drawing a cross section of the 3D model and selectively hardening the material. When a layer is completed, the part is peeled from the tank and fresh resin is let to flow beneath and the process starts again [56, 61]. The thickness of the layer is controlled by the energy of the light source and the exposure time [62]. The solidification of the layer inside the resin is due to photopolymerization. In this process lights initiate a chain polymerization that causes a photo-crosslinking of the macromolecules supported by the crosslinkers that bond polymer chains [63]. SLA printers use advantage of the phenomenon of photoinitiator systems that convert light energy into radicals or cations that drive polymerization. Typically, photoinitiators with high molar attenuation coefficients at UV wavelengths over 400 nm are used [64]. The major process parameters influencing SLA printing outcomes are the cure depth which depends on the energy of light the resin is exposed to, the energy which is controlled by the laser power, and the time the resin is being exposed to the light [59].

FDM technology comes as a sub-category of DIW. In direct ink writing the ink flows through the nozzle and is directly deposited in the printing platform where it solidifies through evaporation of solvents, chemical changes or cooling [65]. FDM works by depositing a continuous flow of melting material over a built platform layer by layer until the part is completed [66]. This additive manufacturing technology's material comes in the form of a plastic filament or metal wire which is unwound from a coil and supplies to produce the part. Printing resolution, choice of materials, and surface finishing are some of the drawbacks of this method [60]. Viscosity of the filament as well as the nozzle size determine the achievable resolution, whilst surface finish and porosity mainly depend on the Z-axis movement of the system and the adherence between layers. The nozzle temperature, bed temperature, and layer height are parameters determining the mechanical behavior and physical performance of 3D printing parts [67]. A similar approach to this is seen in the droplet-based printing technique, where the ink is deposited in drops as needed.

In FDM technique, the nozzle directly deposits the material on the bed (See **Fig. 4** (c) and (d)). Therefore, bed calibration is one of the most important settings considerations. Poor bed calibration results in inconsistent distance between the nozzle and the building platform translating into uneven part's layer thickness, warping, and potential collisions between the nozzle and the bed or the printed parts [59]. The printer nozzle can be changed and adapted to the printing needs. Larger nozzle hole diameter allows for shorter production time [68]. Nozzle speed, which is the speed the nozzle moves while depositing the melted filament over the bed, relative density of the material related to the printing infill selected, geometry of the structure infill, nozzle temperature which is the temperature of melting of the material, and bed temperature, related to the temperature of the building platform and directly affect the adhesion of the layers, are greatly important settings to be considered when printing. Ferretti et al conducted an extensive analysis on the influence of printing parameters on the performance of FDM 3D printed pieces. They identified that layer slicing can significantly influence defects in printed parts and underscored the importance of setting optimization to minimize defects and enhance outcomes, suggesting that such could help extend the applicability of the technique in industry [69].

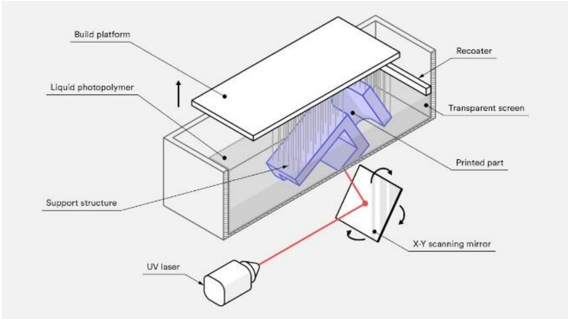

(a)

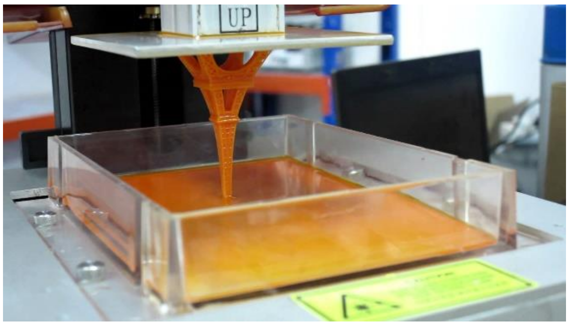

(b)

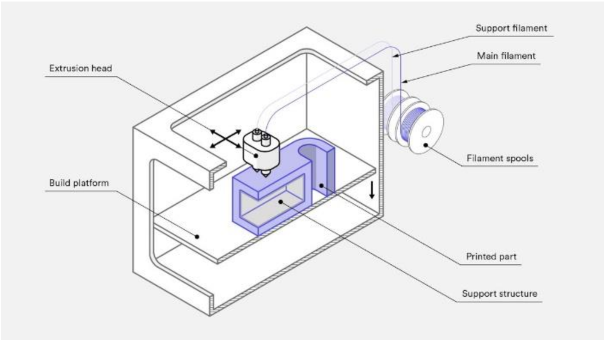

(c)

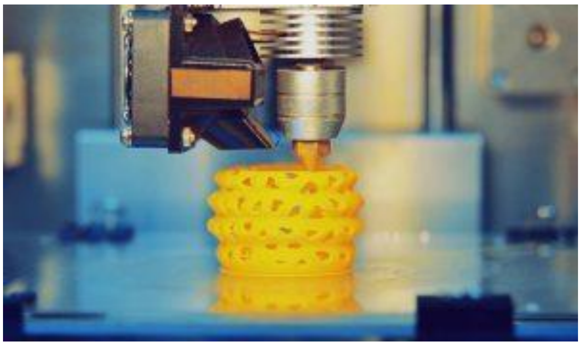

(d)

Fig. 4 Printing systems schematics and printing samples (a) and (b) SLA. (c) and (d) FDM [61, 66, 70, 71].

Electron beam melting (EBM) uses an electron beam to selectively irradiate a powder target bed. The heat from the beam melts and fuses the metallic powder layer by layer to build up the model [72]. It typically takes place inside the machine in vacuum and at very high temperatures. The powder is preheated, and the electron beam is used to fuse and melt together the powder layer by layer to eventually build a semi-solid block of powder that has the solid part inside covered in this powder cake. This cake is commonly called the agglomerate and is removed by a blasting process [73, 74]. The technique allows for reduced warping and distortion, greater design flexibility, better dimensional accuracy and more efficient post-processing [75]. Compared to FDM or DIW systems, EBM allows to create structures that behave similar to a bulk material [76] in terms of density, mechanical strength, and other physical properties, meaning that the final structure behaves as if it was made of a solid, continuous material, lacking internal porosity, layer separation, or weaker inter-layer bonds common in the other two techniques mentioned above. Regardless of the structure, sacrificial material is not required as the final model is embedded within the powder cake [77].

Selective laser sistering or SLS similar to EBM, also use a high-power source to irradiate the target powder bed [78]. In this widely adopted AM technology, the fusion of particles occurs through various mechanisms including solid-state sintering, chemically induced biding, liquid-phase sistering (which involves partial melting), and full melting depending on the material properties and process parameters [79]. This printing mechanism involves a laser supply unit, a scanning system to direct the laser beam, a powder dispensing system, and a sintering platform where the part is formed. The printing process is the core difference between SLS and EBM. Printing beings by spreading an even and thin layer of powder on the building platform using a roller or a blade. The laser then selectively scans the powder according to the geometry of the digital model. Once the layer is completed, the platform is lowered, and a new layer of powder is deposited. This process is repeated layer by layer until the full part is built [80]. On a microscopic level, the laser causes molecular diffusion leading to the cohesion of particles and the development of the layers. Once the part is completed the unsintered powder is brushed or blasted away having served its support and thermal buffer function [59]. **Table 3** shows an extensive summary of five different 3D printing technologies.

Table 3. 3D printing technologies comparison

Parameter	FDM	SLA	SLS	EBM [81]	DIW
Printing mechanism	Extrusion of thermoplastic filament [82]	VAT photopolymerization [83]	Laser sintering of powder [84]	Powder bed fusion using electron beam in vacuum environment	Deposition of melted thermofilament [59]
Material form	Filament [59]	Liquid resin [59]	Powder [59]	Metal powder	Filament [59]
Energy source	Heated nozzle [82]	UV laser [63]	CO_2 laser [85, 86]	High power electron beam (max. 3 kW)	Pneumatic, mechanical extrusion [59]
Materials example	PLA, ABS, PEEK, nylon, etc. [59]	PEG, PCL, polycarbonate-based [59]	PA12, TPU, PP, etc. [59]	Ti_6Al_4, cobalt, nickel, aluminum, tool steel	Magneto-active composites [87]
Layer resolution	0.05-0.5 mm [59]	0.01-0.25 mm [59]	0.05-0.03 mm [59]	50-150 µm	0.2-0.4 mm [88]
Part resolution (min)	≈ 40 µm[69]	≈ 10 µm [89]	≈ 20 µm [90]	±0.1 mm/100 mm, Ra: 20-50 µm	≈ 15 µm [88]
Surface finish	Poor [91]	Excellent [91]	Rough [91]	Rougher than SLM, post processing needed	Rough [88]
Support structure required	Yes [59]	Yes [59]	No [59]	No (unsintered powder provides support)	Yes [59]
Post-processing need	Minimal [59]	Yes (post-curing) [92]	Moderate [59]	Yes, often machining, sandblasting, or HIP	Yes [59]
Print orientation impact	Yes [93]	Yes [94]	Yes [95]	Yes, differences in microstructure and grain orientation	Yes [59]

Key influencing parameters	Nozzle temperature, bed temperature, speed, raster angle [67, 96-98]	Cured depth, layer thickness, exposure time [99, 100]	Laser power, scan speed, hatch spacing [101, 102]	Beam powder, scanning speed, focus offset, preheating, powder size	Ink rheology, filler distribution [87]
Mechanical anisotropy	Yes [93]	Yes [94]	Yes [103]	Yes, microstructure anisotropy and building direction influence	Yes [59]
Applicatio ns	Low-cost prototyping, functional parts [59]	Dental, biomedical, high-resolution parts [59]	High-strength functional parts [59]	Biomedical implants, aerospace components	4D printing, soft robotics [87]

Finally, traditional manufacturing includes a wide range of methods, but the general workflow starts with a solid block or rods of raw material that is shaped into the final product by cutting, milling, frilling, or other processes (formative method) or, the material is shaped using molds or dies (formative method). The process starts with the designing and drawing of the part, then machining, milling, welding, or molding the material until the final product is finalized.

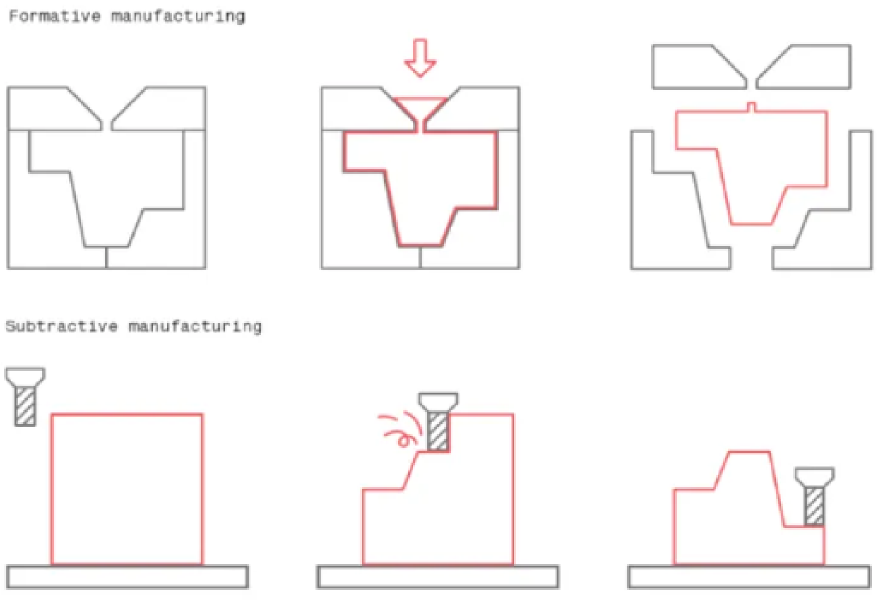

Fig. 5 Types of traditional manufacturing [104]

The current advances in 3D printing permitted its implementation in industry. At first, 3D printing could not offer the same capabilities as traditional manufacturing, and in the cases it did, these benefits came at high costs. Currently, as the 3D printing industry continues to grow and progress, the affordability and adaptability of this technology is also developing. AM has shown to have the potential to become the norm over the decades to come. AM machines do not require expensive arrangements or setups to produce small batches of products. However, the initial investment of acquiring a printer is high [105]. Whilst entry-level printers range from 200$ to 1,000$; an industrial 3D printer can cost anywhere between 10,000$ and 100,000$ [106]. Leaving aside this initial investment, materials cost is another relevant aspect to consider. 3-D printing companies are trying to force the filament prices down by creating competition in the market, making the technology more suitable for mass production.

Whereas AM is not generally suitable for mass production, it offers advantages in producing complex parts without assembling steps. Therefore, complex geometries are easier to achieve [105]. The medical industry takes particular advantage of this feature and uses it for manufacturing implants and prothesis through the replication of pieces based on body parts imaging [107]. Lastly, 3D printing particularly excels in mass customization, it easily outperforms conventional methods by enabling the production of highly individualized products with fast adaptation and no lead time. Popular known products now being manufactured using AM include Invisalign brace molds [108], hearing aids, and phone cases [105].

3D is relatively slow compared to standard manufacturing and it takes hours to produce a product. Also, the size of the object is a major key in the production process. A printer is only capable of producing pieces smaller than the size of the machine case limiting the variety of parts that can be produced. Furthermore, while 3D-printers often perform tasks without human intervention, it may still require supervision, initial settings, and manual calibrations in certain occasions. Mohsen Attaran conducted a review of the advantages of additive manufacturing over traditional manufacturing and summarized his findings in **Table 4**.

Table 4. Advantages of AM over traditional manufacturing [56]

Areas of application	Advantages
Rapid prototyping	Accelerates prototyping reducing time to market Reduces cost involved in product development
Production of spare parts	Reduces repair times Reduces labor cost Avoid costly warehousing
Small volume manufacturing	Small batches production is cost-efficient
Customized unique items	Enables mass customization at low costs Quick production of customized replacement parts
Complex work pieces	Produces high-complexity pieces at low costs
On site and on demand manufacturing of customized replacement parts	Eliminates storage and transportation costs Prevent downtimes saving money Reduces repair costs Shortens supply chain
Rapid repair	Significant reduction in repair time Allows to modify repaired components to the latest design

1.3. 3D printing in medicine

Currently, 3D printing represents an opportunity for the medical and pharmaceutical industry to create more specific drugs, enable rapid production of medical implants and change the way surgeons and physicians plan procedures [109]. 3D printing capability of recreating patient-specific anatomies represents a tool to significantly improve research knowledge and increase the level of understanding of the disease. For printing of patient-specific models or implants, high-resolution scanned images are required. This information can be obtained through computer tomography and cone-beam CT, two techniques mostly used for bone or denser structures, and magnetic resonance imaging which allows imaging of soft tissues [110]. Different anatomical structures require different printing techniques and materials to better mimic the tissue or better recreate the mechanical properties of the modelled part [111]. The mechanical properties of bones are easy to replicate through 3D printing techniques. Materials like acrylonitrile butadiene styrene (ABS) [112], plasters powder [113], and hydroquinone [111] have been used in the past. Soft tissues represent a bigger challenge. Multimaterials composite might be a solution to replicate the mechanical properties of soft tissue.

3D printing has been successfully applied in healthcare throughout several fields. These applications span from preoperative planning with patient-specific anatomical models, to the development of biocompatible implants, simulation platforms, and bioprinted tissue. Some application examples include but are not limited to thoracic surgical simulations where pulmonary arteries were printed for surgical planning, education and device testing [114], substantial benefits of 3D printing in cardiac education, surgery planning, modelling and device information has been explored [115], a potential step towards liver tissue engineering was taken by Jeon et al. by evaluating the feasibility of using 3D printing to construct multilayered hepatic structures with improved liver-specific function [116], a systematic literature review has highlighted the application of 3D printing in neurosurgery including tissue engineering implants [117], custom-made artificial bones have been developed using inkjet printing for maxillofacial reconstruction [118], 3D printing has found its applicability in ophthalmology and offers future possibilities in bioprinting of ocular tissue [119], airway splints, nasal cartilage, articular protheses, and tympanic membrane 3D printed fabrication in otolaryngology [120], designing and fabrication of implants and protheses in orthopedic surgery to match patient’s anatomy, specifically for complex or irregular bone structures [121], 3D custom implants and protheses are also used in plastic surgery specially in skull and facial bone reconstruction for asymmetrical or irregularity corrections [122], it can enhance podiatric care by improving the design and affordability of custom-made prosthetic devices or shoe fillers for patients with amputations [123], 3D printed splints have been used in pediatric and adult patients with airway collapse, offering structural support that degrades over time [124], it use in revolutionary implementations like hepatology transplantation was assessed by Zein et al. [125], applications in urology was thoroughly reviewed by Soliman et al. emphasizing its potential to transform organs replacement, patient-specific modeling, surgical training, and tissue engineering [126], 3D printed was successfully used for planning a stent-grafting procedure for an aortic aneurysm with sharp neck angulation, in this case, a physical model was printed allowing for the surgical team to better asses anatomical challenges and improve the selection of the devices for endovascular repair [127].

In the pharmaceutical sector, 3D printing may allow for personalized medicine. Customized dosage could be tailored to individual’s therapeutic needs or combination of therapies, addressing the current limitations present in conventional manufacturing which relies on mass production of fixed-dose units. These methods are still in developing phase but promise to overcome the rigidity of large-scale systems and play a key role in personalized and precision medicine [110].

There is a wide range of materials that can be used in additive manufacturing including but not limited to plastics, rubbers, ceramics, glass, and metals [128]. Besides the part-specific requirements, the materials of choice also must not generate toxic substances while processing apart from being biocompatible and biodegradable [129]. The pharmaceutical sector has found used in lactose to fill or dilute 3D powder bed printing and SLA in 3D printed tablets [130], polylactic acid (PLA) is a biodegradable polymer often used in implants, scaffolds and drug delivery systems and has been approved to use by the United States Food and Drug Administration (FDA) [131], PVA or polyvinyl alcohol is a water soluble thermoplastic that has been used as suppository shell for controlled drug release [132], hydroxypropyl methylcellulose (HPMC) was used by Yiliang and his team in the preparation of semi-solid tablets with active pharmaceutical ingredients loading at ambient temperature [133], gelatin has been used for decades in pharmaceutical formulations and it has been found to be compatible with 3D printing allowing to construct drug delivery systems [134].

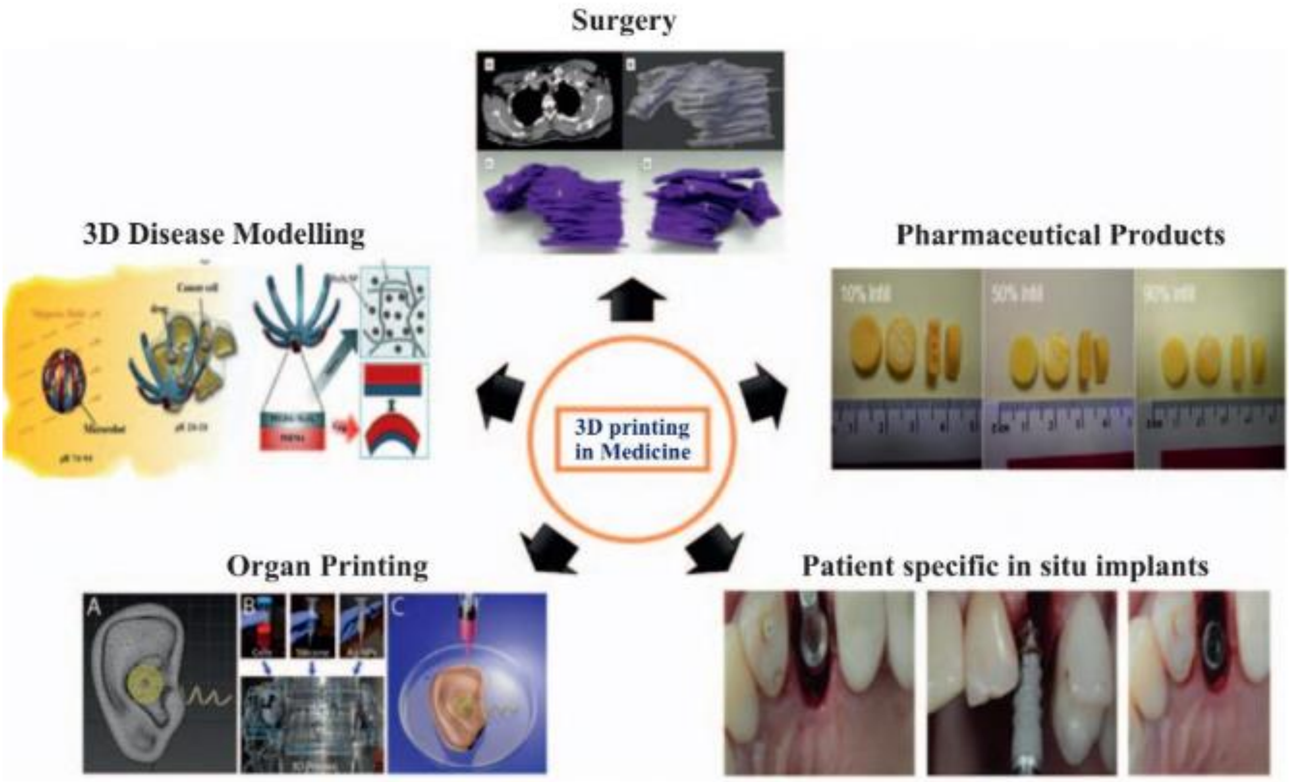

Fig. 6 Applications of 3D printing in medicine [110]

Anatomical structures need to fulfill different functions than pharmaceutical requirements, these functions are oriented towards mechanical properties, tissue mimicking qualities, and design-specific features. Photopolymer resins have been used to replicate bones and dental models [135], stainless steel, titanium, aluminum, cobalt, and other common metals are used to print implants and fixations [136], and bone surfaces for orthopedic modelling benefits of paper, plastic and sheet metals printing [121]. Generally, metals alloys are commonly used in implants printing given their durability, high strength, and relatively easy processing [136-139]. Bioceramics and bioactive glasses are present in orthopedics developments due to their mechanical properties and extended life, for example, zirconia is used as a material for joint replacements [140].

Table 5. 3D-printing technologies, materials and medical applications [109]

Technology	Material	Medical use
Stereolithography (SLA), digital light processing (DLP)	Photopolymer resin	Bone, dental models, dental implant guides, hearing aids
Multijet modelling (MJM)	Plastics, polymers, polypropylene, HDPE, PS, PMMA, PC, ABS, HIPS, EDP	Medical models, dental casts, dental implant guides
Powder bed and inkjet head 3D printing (PDIH), plaster-based 3D printing (PP)	Stainless steel, polymers, ABS, PA, PC, ceramics: glass	Color models especially color coding of anatomy
Fused deposition modelling (FDM), fused filament fabrication (FFF)	Plastics, polymers, ABS, nylon, PC, AB	Medical instruments and devices, rapid prototyping exoskeleton
Selective laser sintering (SLS), direct metal laser sintering (DMLS), selective heat sintering (SHS), selective laser melting (SLM), electron beam melting (EBM)	Powder-based materials. common metals and polymers, nylon, stainless steel, titanium, aluminum, cobalt chrome, steel, chrome, and copper	Models that require a lattice, medical devices such as implants and fixations
Laminated object manufacturing (LOM), ultrasonic consolidation (OC)	Paper, plastic, and sheet metals	Orthopedic modelling of bone surfaces
Laser metal deposition (LMD)	Cobalt, chrome, titanium	Limited. Commonly used to repair existing parts and build very large parts

1.4. 3D printed phantoms

Fabrication of 3D printed phantoms requires knowledge of the properties of the tissue to mimic. 3D printing of surgical training phantom has been extensively evaluated. One of its most notorious advantages is allowing for training on repeatable simulations that are not possible on living patients. A study conducted by Larcher et al. exposed that for a surgeon to be considered proficient in partial nephrectomy robotic-assisted surgery, it is needed around 150 surgical experiences [141]. Whilst a simulation with a 3D model cannot replace in vivo scenarios training, it does allow for familiarization with the procedure. 3D printing can provide cost-effective, realistic models for trainees to work with. Ploch et al. developed a synthetic gelatin-based neurological model which was presented to 10 neurosurgeons and trainees to assess its effectiveness for surgical training. The feedback unveiled that 100% of the participants affirm their educational value and 95% endorse its utility in surgical training and teaching [142]. A similar study was conducted by Mery et al. involving a 3D-printed cerebrovascular model designed for aneurysm clipping practice, in this study 97% of the participating trainees highlighted the value of the model in surgical education [143].

The unique quality of 3D printing in replicating individual patient-features presents a great advantage in surgical planning. Visualizing the individual anatomy of the patients increases the accuracy in surgical planning resulting in better operations outcomes and lowering the surgery risks to the patient [144]. 4 out of 5 surgeons admitted to having changed their approach to surgery after seeing the anatomy model on kidney tumor surgery according to the review conducted by Glybochko et al. [145].

In oncological procedures, medical phantoms are used for validation and verification of imaging systems. In this field the main characteristic to replicate is the radiological properties of the anatomic part. Several studies have tried to replicate realistic attenuation properties for imaging phantoms using different 3D printing materials and techniques [146]. Nylon has been used in SLS to replicate lung tumors. However, the radiation attenuation properties achieved were poor [147]. On the other hand, an agar-gelatin tumor developed by Sramek et al. achieved great radiological properties compared with the patient's tumor it replicated, but it lacks the geometrical characteristics of the head and neck carcinoma [148]. Other materials such as polyethylene terephthalate (PET-G), polylactic acid (PLA) filament acrylonitrile-butadiene-styrene (ABS) have also been tested for replicating imaging tumor phantoms [146].

In an oncology case study, a 75 year old patient diagnosed with non-small cell lung cancer by biopsy underwent a chest CT scan and the paramediastinal lung lesion present was segmented according to HU ranges (air, lung interstitium, fat, muscle, muscle, vascular, skin, bone, and lesion). Based on this, a patient anatomy mimicking 3D printed phantom was developed using FDM technique and PLA material. Comparative CT studies between the patient and the printed model were performed and the results showed excellent agreement between them in terms of volume, but the model lacked accuracy in delineation of the tissue. Unfortunately, attenuation properties measured in HU values were poor in the printed model. It is also mentioned that creating a full-size thoracic phantom presented significant challenges given the complexity of the structure [149]. **Fig. 7** shows the result of this study in terms of attenuation properties. It is perceived that whilst the phantom did not reach the required HU values, it was able to replicate complex anatomical structures.

A similar study to the one conducted in this report was conducted by Se An Oh et al. who evaluated the feasibility if fabricating variable infill phantoms using 3D printing for QA in radiotherapy. In this study, several samples of different infills of 3D printed PLA using FDM technique were tested regarding its radiation attenuation properties in terms of HU. In the study the authors report that low density attenuation was successfully achieved, but high-density structures such as bones could not be mimicked [150].

Remarkable results were achieved by Dancelwicz and his team who printed phantom inserts to mimic various body tissues using a FDM and SLA printers. The thorough review of radiological achievable properties of materials involved printing different infills of samples made of ABS, standard PLA, photoluminescent PLA, woodfill, bronzefill and copperfill plastic filaments, as well as blends of bronze and copper powder in PLA plastic. CT images at 80 kVp and 120 kVp of the commercial phantom and the printed one were performed for evaluation and comparison. Their results provide useful information on radiation attenuation mimicking 3D printable materials comparable with various body tissues and structures [151].

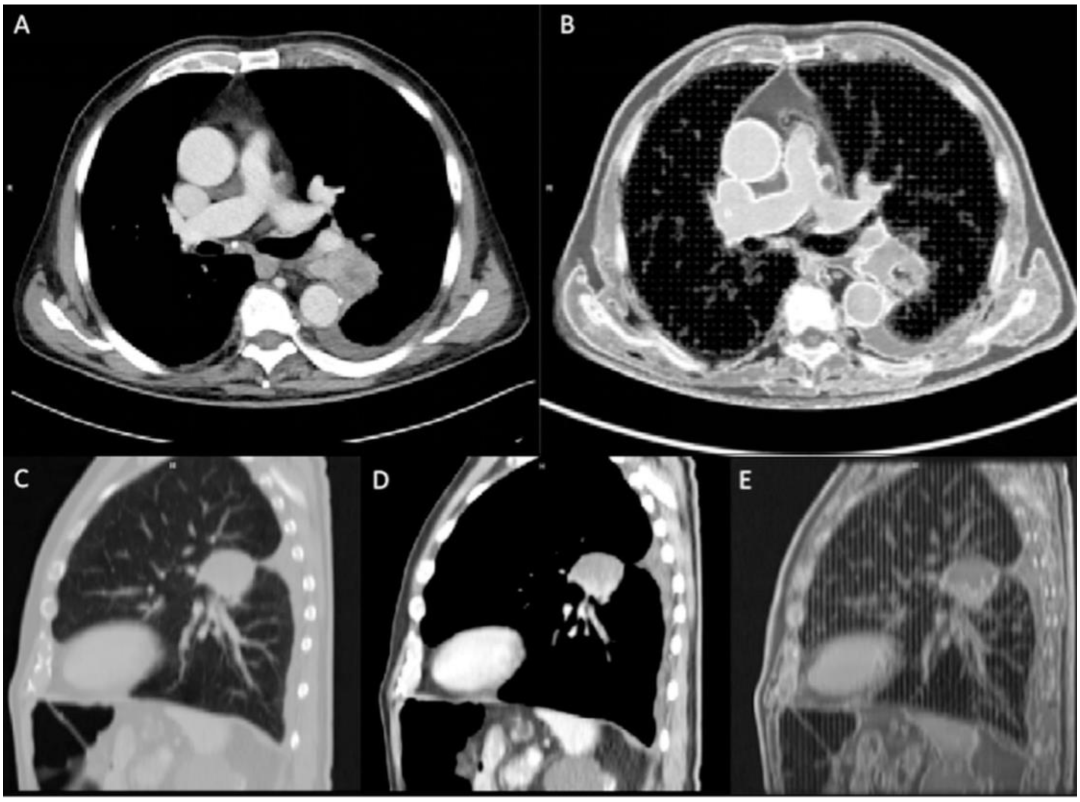

Fig. 7 CT comparison between the patient (A, C, D) and the phantom (B, E) on an axial and sagittal plane [149]

A 3D printed phantom for QC was constructed by another team and evaluated in terms of imaging performance using MRI, CT, PET/MT, and PET/CT and comparing the results with commercial phantoms. FDM, SLA, and Polyjet techniques were implemented. A completed printed CT QC phantom of 20 cm of diameter with customizable internal inserts was fabricated, and its suitability for high contrast resolution test, uniformity test, and thickness test was evaluated [152]. This workflow seems to be standard in evaluation of performance of printed phantoms for radiology purposes as it is seen in many scientific publications. On this line of work Villani et al carried out a systematic study of PLA and ABS printed plates at several infill densities and irradiated the samples with 50-120 kVp diagnostic X-rays [153]. From this study they confirmed that full solid pieces (100% infill) PLA can reproduce the mass-attenuation curve of commercial PMMA slabs. This study is especially relevant for QA phantom development as it shows that controlled fillings can emulate certain tissues without chemical doping and proved that 100% infill provides a robust substitute for conventional water equivalent PMMA.

From a manufacturing technique standpoint, the study showed that 100% infill PLA printing was possible and does not present challenges whereas ABS was reported to suffer warping. On the other end of the spectrum, low infill densities produced image artifacts and anisotropic attenuation. Finally, Villani's team suggested incorporating high-Z fillers into PLA to improve the attenuation range.

Taking together these studies, a visible interest in developing a workflow for evaluating 3D printed medical QC devices can be perceived specially on replacing commercial PMMA with AM options manufactured in house or in non-commercial establishments able to provide a geometrical flexible, dosimetrically predictable and cost-effective alternative for healthcare practitioners.

1.5. Ethics and standards for 3D printing in medicine

The integration of 3D printing technologies into healthcare has introduced new questions regarding regulatory, safety, and ethical challenges that demand a comprehensive evaluation and development of a framework. With the fast growing and implementation of 3D technologies in medicine, the regulatory systems must as well evolve to keep pace with such development and expanding applications [154]. Over 40 companies worldwide compete to commercialize bioprinting and many of them offer materials and inks that mimic natural tissue [110]. The use of these specialized materials carries distinct regulatory implications. One of the main concerns on safety matters is the biocompatibility of materials. The International Organization of Standards have addresses this in its published set of standards for compatibility evaluations ISO 10,993 [155]. However, the properties of the raw materials used in printing tend to change after processing. Therefore, evaluation of the materials before the printing process may not be the ideal testing as AM can alter the material's properties. Moreover, 3D-printed implants require the same validation as any other medical implant in terms of sterility, degradation profile, and shelf life [156]. The American Society for Testing and Materials International (ASTM International) works together with ISO to provide best guidance to biological testing. Most of the 3D bioprinted medical devises are overseen by the ASTM International ISO-10993 Serie and others and during the first half of 2021 two regulatory developments were achieved: ISO TC261 (ISO/ASTM DTR 52916 and ISO/PWI TR 5092) and ASTM standards in ASTM F3001-14, ASTM WK72659, and ASTM WK67583 [110].

There are two pathways for allowing the marketing of medical devices (a) conventional 510(k) and (b) pre-marketing approval (PMA). The FDA states that a 510 (k) approved device has "demonstrated that it is safe and effective, i.e. substantially equivalent to a legally marketed device" this approval requires reduced clinical trials and takes less time than PMA [157]. PMA pathway involves more strict regulatory requirements and thorough clinical trials. 501 (k) comes, in many cases, as a more desired path to commercialization. The Federal Food, Drug, and Cosmetic Act states that a 3D printed patient-specific anatomy used in a medical device (such as implants), the entire workflow of the printing process is classified as part of the device-specific tool and must be included in the regulatory submission of the device [157]. However, the lack of clarity on what constitutes a custom device is an issue in several international regulations. Medical devices produced through AM are often treated as custom-made by agencies of UK, EU, Australia, and Canada [158]. The FDA has sustained workshops on additive manufacturing of medical devices covering the topics of design, printing, and post-printing considerations, materials, printing parameters, mechanical and physical assessments, and biological considerations including compatibility, sterility and cleaning [157].

The newest EU regulation on medical devices, effective since May 26th, 2021, has been highly criticized for not addressing 3D printing issues or personalized medical devices [159]. After these attacks, the response was to release a separate document answering open questions regarding this issue [160]. Petterson et al. summarizes the key questions for liability in 3D printing context as (1) what the attributable liabilities are, (2) the demarcation of liability between different actors, (3) the definition of defective product, (4) determining who the manufacturer is. Whilst realistically 100% safety of a product is not expected, appropriate standards need to be set. Production of medical devices in healthcare facilities is disregarded by regulatory entities as long as the product is not produced on a large-scale or transferred to another legal entity, and there is no existing product in the market that can cover the needs at the appropriate performance levels [161]. About custom-made 3D printing medical devices, the questions and answers document released states that industrial manufacturing processes, including 3D printing, may be used for custom-made parts as long as they are not mass-produced [160].

Petterson et al. also consider that the cautious approach of the EU legislature towards these topics have led to uncertainties regarding 3D printing regulations and may be interpreted as a hostile stare upon innovation. New methods, however, continue to be developed where law permits and adapts where it does not, exerting pressure over the relevant institutions and authorities towards explicit regulations on applications of innovative techniques on applications of 3D printing in healthcare for personalized medicine and rapid prototyping.

2. Methodology

To study the feasibility of fabricating a 3D printed medical phantom using PMMA, it was necessary to outline the experimental approach and technical processes involved in the fabrication. For this, characterization of the material, selection of the equipment and software to use, and development of a refined printed protocol was of outmost importance, as well as the analysis of the procedures used to test, evaluate and assess the geometrical accuracy and radiological behavior of the printed prototype. Firstly, determining whether printing with PMMA allows indeed replicates the attenuation characteristics of a commercial PMMA phantom used in clinical quality assurance protocols. Some of the key variables identified for evaluation include infill density, printing settings, homogeneity, and Hounsfield Unit (HU) values, as well as the appearance of artifacts and edge effects in the imaging process.

2.1. Materials

Polymethyl methacrylate, commonly known as PMMA is a synthetic resin produced from the polymerization of methyl methacrylate [162]. This transparent thermoplastic is widely used in medical physics for its radiological properties. It is capable of mimicking soft tissue in CT imaging and is the goal standard among water-equivalent phantom materials. According to the compositional comparison of **Table 1**, PMMA demonstrates a favorable balance between physical and radiological properties. It is primarily composed of carbon (60.0%), oxygen (32.0%), and hydrogen (8%) making it an organic polymer, and it has a mass density of 1170 kg/m^3 which is slightly higher than water (1000 kg/m^3). This together, with its effective atomic number (Z_{eff}) of 6.24, allow the material to deliver Hounsfield Unit (HU) values in the range of soft tissue, ideal for QA tests involving tissue material equivalents. Furthermore, its near-neutral neutron number (N) aligns with other water-equivalent phantoms.

Beyond all its aforementioned characteristics, PMMA is compatible with fused deposition modeling (FDM) 3D printing technologies making it ideal for the evaluation of the feasibility of fabricating a 3D printed phantom for QA in CT. The material, in its printable form, is a filament of 1.75 mm of diameter, recommended extrusion temperature between 245 ℃ and 255 ℃ and bed temperature of 100 ℃ to 120 ℃, compatible to be used with the printer chosen, Zortrax M300. It is intended to be used as an external material setting in the printer in the section glass-type filament due to its transparency and rigidity. PMMA filament is characterized by being strong, rigid and lightweight, as well as impact resistance, it is soluble in acetone, and not food safe. It has a specific gravity of 1.20 g/cm^3, Rockwell hardness of R 105, maximum tensile strength of 12.100 psi or 83.42 MPa, maximum compression strength of 17,000 psi or 117.21 MPa [163].

As a reference or standard value for the evaluation of the printed sample, a PMMA slab standard medical phantom from the Kaunas Oncology Hospital is also used. This PMMA slab is part of the hospital’s routine QA tools for various radiation healthcare devices. Its average HU values, based on CBCT scanning, range from +100 to +140 HU.

(b) (b)

Fig. 8 (a) PMMA filament and (b) slab PMMA phantom [164]

For broader context, comparison with this phantom enables a direct evaluation of the printed device's radiological performance relative to an accepted clinical standard. It also permits testing of artifacts that may have been introduced in the printing process, and which could compromise the utility of the fabricated device in QA contexts. PMMA medical phantom slabs are crafted meticulously for reliable testing and calibration of automatic exposure control systems in radiography, and are constructed following local, national and international regulations.

2.2. Printing equipment and protocols

The printer used for the fabrication of the phantom was the Zortrax M300, which is a FDM 3D printer of professional grade suitable for building large volume parts and compatible with various filaments. This printer features a build volume of 300 x 300 x 300 mm, which provides sufficient space for the fabrication of the full-scale CT phantom without need for segmentation of the model which offers to reduce possible assembly errors. The technical specifications as provided by the printer manufacturer are as follows:

Table 6. Technical specifications and operational characteristics of the Zortrax M300 3D printer [165]

Technology	LPD (Layer Plastic Deposition) – depositing melting material layer by layer onto the build platform
Build volume	300 x 300 x 300 mm (11.8 x 11.8 x 11.8 in)
Layer resolution	20 - 290 microns
Minimal wall thickness	450 microns
Nozzle diameter	0.4 mm (standard)
Filament diameter	1.75 mm

Support	Mechanically removed – printed with the same material as the model
Maximum extruder temperature	290 ℃
Maximum platform temperature	105 ℃
Ambient operating temperature	20 - 30 ℃
Connectivity	SD card
Supported file type	.stl, .obj, .dxf, .3mf
Supported operating systems	Mac OS up to Catalina version / Windows 10 and newer versions
Software	Z-SUITE®

Initially, it was necessary to understand what the best infill configuration for the task of mimicking soft tissue's attenuation properties is. For this, experimental validation was conducted focused on evaluating how different infill densities affect radiological properties of 3D printed PMMA samples. To this end, simple cube geometries were designed using the Z-suit software and printed using three different infill densities: 10%, 50% and 100% so as to examine the influence of the internal material density in the attenuation profile which are a critical feature for potential phantom applications.

To ensure consistency, the same printing parameter was applied to all three models. These printing parameters were run on a Z-suit's external materials profile optimized for glass-like filaments which is the category, among the library's choices, that better describe PMMA. The printing was carried out following the standard settings:

- Nozzle diameter: 0.4 mm
- Layer thickness: 0.14 mm
- Extrusion temperature 254 ℃
- Platform temperature: 30 ℃
- Printing speed: 30 mm/s
- Infill pattern (10% and 50% samples): PATT.0 (default pattern)

Both the 10% and the 50% samples were printed successfully and without need of intervention or further refinement also showing good adhesion and geometric integrity. These prints serve the purpose of evaluating low and moderate infill configurations. However, the 100% infill exhibited substantial technical difficulties during printing. This model was particularly prone to material related issues such as warping during the cooling phase, uneven material deposition, and frequent nozzle clogging most likely due to the prolonged printing time. To address this challenges it was necessary to implement iterative modifications to the printing protocol, some of the printing parameters tunning involved adjusting the extrusion and platform temperatures, reducing the printing speed to improve interlayer bonding and thermal stability, frequent manual cleaning and replacement of the nozzle to combat clogging, and fine-tunning of the material feeding system as it presented challenges by getting stuck.

Despite these efforts, 100% infill prints remained a substantial challenge. Few samples reached the desired geometry characteristics. The best sample among the batch was selected to evaluate, together with the 10% and 50% infill cubes, its radiological properties through imaging analysis. The radiological performance of the samples was evaluated using cone-beam computed tomography

(CBCT) on a Halcyon linear accelerator (LINAC) to investigate the influence of infill densities in internal homogeneity and attenuation. The resulting images were submitted to a qualitative and quantitative analysis with particular emphasis on Hounsfield Units (HU) values as a measure of radiological properties. Regions of interest were drawn within each sample and voxel-level HU data was collected and subjected to statistical analysis allowing for a comparison of the attenuation properties of the printed PMMA sampled against the clinical standards.

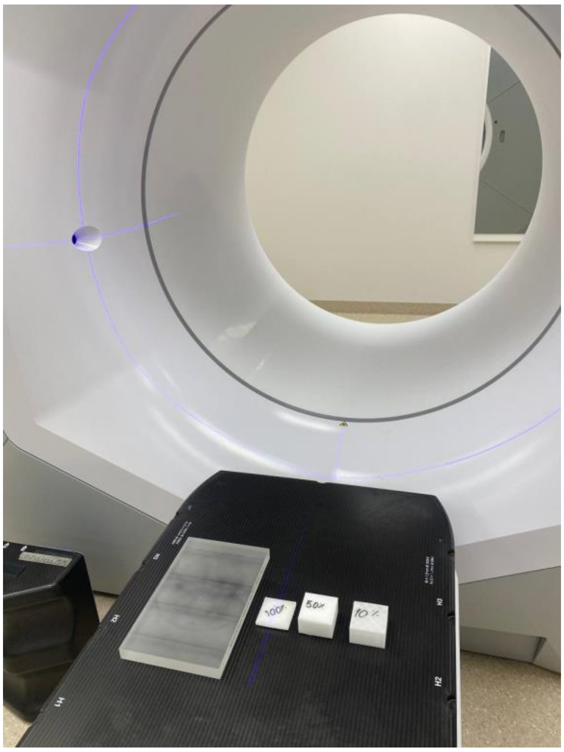

Fig. 9 Printed samples at different infill percentages to evaluate the correlation between infill density and radiological attenuation properties

It was hypothesized, during the printing phase, that increasing the surface area in contact with the printing bed could improve the process. Therefore, to test this hypothesis, a head CT phantom was selected to be fabricated using PMMA filament. Head CT phantoms are used in routine QA and QC procedures in medical imaging departments and are traditionally made with PMMA. Successfully printing this geometry in a single piece would not only validate the developed printing protocol but also prove the feasibility of producing custom phantom in-house in clinical institutions potentially reducing the cost of acquisition of the commercially available ones. The design of such model was made using AutoCAD for sketching the device following the geometry of the Kyoto Kagaku CT phantom which is widely used in clinical environments. This design features a cylindrical geometry of 16 cm diameter and 15 cm heigh with multiple internal cavities of 13.1 mm diameter. The final weight of the printed phantom was estimated to be around 4 kg.

The .stl file generated with AutoCAD was then imported to Z-SUITE® which is Zortrax's slicing software and serves the function of both slicer and printer manager allowing for detailed control over key printing parameters. Since the PMMA filament is not natively supported by the printer's materials library, the printing process was operated in external materials mode and glass-type materials chosen.

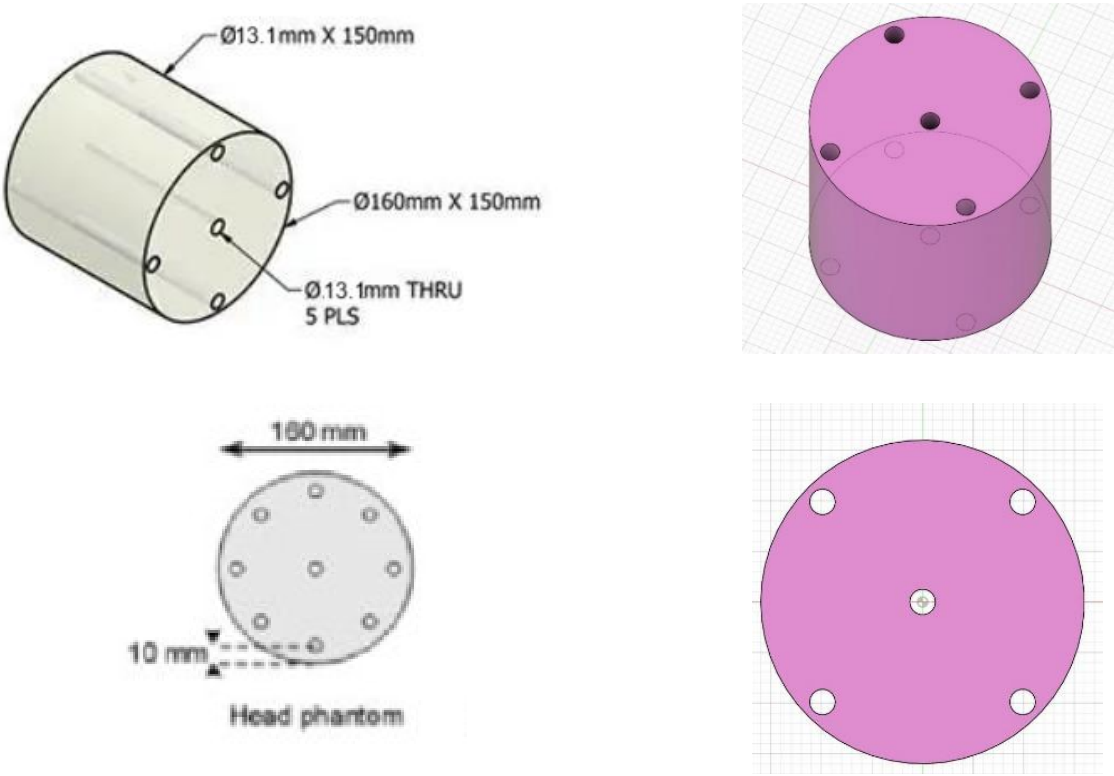

(a) (b)

Fig. 10 Head CT phantom (a) Kyoto Kagaky geometry (b) AutoCAD design

Despite the flexibility offered by the software for fine tuning of the printing parameters, the printing process proved to be a challenging aspect. In the preliminary testing of the printing parameters the samples were printed with geometric characteristics successful for the scans. However, no print attempt of the full head phantom, or even tests slabs over 2 cm tall could be completed. Printing consistently stopped at higher layers, typically after reaching highs of between 1.5-2 cm, where layer separation began to occur. The recurring issue was loss of adhesion between the upper layers, which is hypothesized as due to progressive cooling of the upper layers and the print environment, i.e. the temperature at the top layers is likely dropping below the glass transition point of PMMA causing poor adhesion and eventual structural failure. In response to this, numerous combinations of printing parameters were tested in an effort to optimize performance, this included adjustment to:

- Extrusion temperature ranging from 200 °C to 250 °C
- Platform temperature from 60 °C to 100 °C
- Printing speed from 20-60 mm/s
- Layer height between 0.14 mm and 0.19 mm
- Cooling fan control on/off

As a further solution attempt, a makeshift heated chamber enclosing the printer was tested, this was essentially a cardboard shell covering the printer to stabilize the ambience temperature and reduce thermal gradients. While this at first seemed to be a feasible solution, it was quickly discontinued as the internal temperature in the system was excessively high and could present a substantial risk for the printer's electronics and stepper motors which are not made for functioning under such conditions.

Therefore, after multiple tries and observations, it was strongly suggested that printing PMMA at 100% infill density and large vertical dimensions is not feasible on an open frame FDM like the Zortrax M300. These challenges reveal the limitations encountered in this study and open the field for further research on 3D printed CT phantoms development using different equipment and exploring alternative materials choices

During preliminary testing with the printed cubes, it was observed that the outer shell layers of the PMMA prints exhibited higher Hounsfield Unit values than the infill region. This effect was attributed to the way the printer works that makes this outer layer receive multiple passes of extruded material during printing. Whilst this may not represent a significant variable for the mechanical properties of the sample, it may compromise its radiological behavior introducing inhomogeneity and edge artifacts when used in image-based applications. Therefore, in a further effort to investigate this phenomenon, a test was carried out to evaluate whether the CT would be able to see this border behavior. For this purpose, the print samples were placed in a water tank and scanned using CBCT.

2.2.1. Assembly and evaluation of head phantom

To evaluate the feasibility and suitability of constructing a full-size phantom using 3D printed PMMA in parts and not as a single piece, the individual printed discs were glued together using acrylic glue. This assembled piece would then be evaluated under the same protocol as the individual pieces described in section 2.3 and the resulting images analyzed to assess structural integrity and radiological performance looking into questioning if the glueing process introduced artifacts or inconsistencies in HU distribution.

Fig. 11 Assembled phantom constructed by bonding individual PMMA printed discs using acrylic glue

2.3. Scanning equipment and protocols

To further investigate the shell-artifacts differences on HU values, the printed disc samples were placed in a water tank and scanned using cone-beam computed tomography (CBCT). Conducting the test in a water environment allows for better evaluation of the attenuation transition between PMMA and its surroundings, keeping in mind that water is the gold standard tissue mimicking material. The primary objective was to identify if the CBCT scan would be able to detect any border artifacts associated with the shell layer of the printed samples that could cause inhomogeneity in the interface between the water and the 3D printed PMMA disk. This was especially important to assess the influence of the outer layer over extrusion characteristic of printed pieces that could lead to false edge delineation during imaging. For this, two CBCT scans were performed using the Halcyon PVA systems at 100 kVp, 30 mA and a slice thickness of 2.00 mm: one scan of the printed samples in water, and a second with one of the printed samples is water alongside a PMMA slab. The first scan set up is presented in **Fig. 12.**

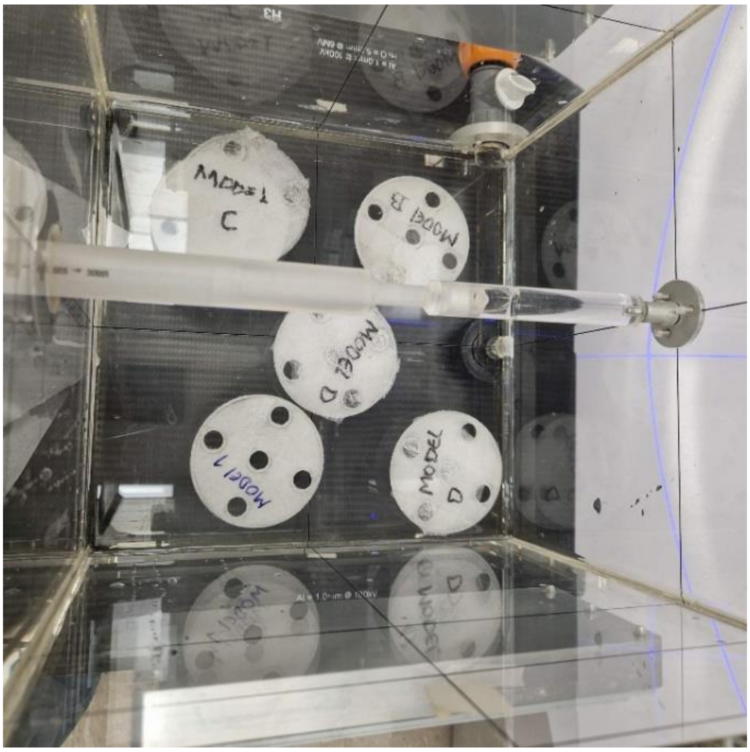

Fig. 12 CBCT scan test for border artifacts evaluation

2.4. Quantitative Analysis and evaluation

A quantitative analysis of the radiological characteristics of the printed samples was performed and the results were compared with a similar evaluation performed over water and a PMMA slab. This analysis included statistical evaluation of the Hounsfield Unit distribution of the different mediums using 3D slicer version 5.6.2. For this, regions of interest (ROI) within each material were defined and voxel level statistics were extracted. For evaluation of the border effects from one material to the next, line profile plots across the samples were drawn.

The ROI were drawn of equal volume within the different materials; each ROI was created using the segment editor module ensuring consistent shape and size minimizing the variability due to volume differences and allowing direct comparison between materials. The segment statistics module was then used to extract mean, minimum, maximum, median, and standard deviation of HU in each ROI. The results were exported to a .csv file and used for further analysis and visualization. Local variations and internal inhomogeneities were assessed by placing multiple ROI within each material **(Fig. 13** (a)).

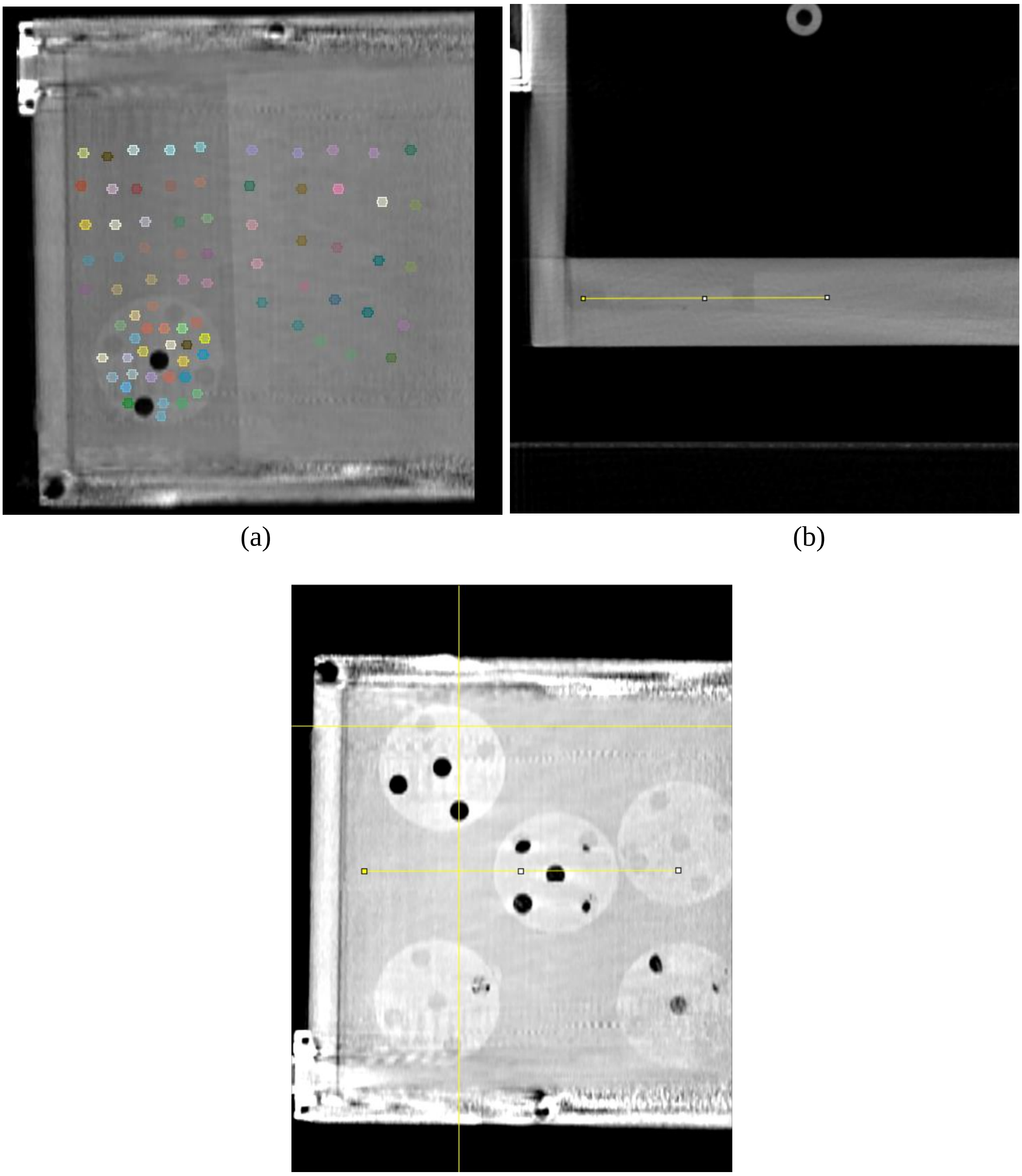

(a) (b)

(c)

Fig. 13 Multiple ROI were evaluated within each material to account for local variations and inhomogeneities and manually drawn line for line profile evaluation for assessment of border artifacts

For further analysis of edge-related effects, a line markup was drawn manually across the CT scan of the samples. In the first CT scan (**Fig. 13** (b)) the line was drawn going from water on one side, through the outer edge of the printed disc, across it, and out the opposite edge, back to water and reaching the PMMA slab, and a total of 244 evenly spaced points were sampled along this line using ImageJ's profile analysis tool and the corresponding HU values of such points were extracted and studied. For the second set of CT images (**Fig. 13** (c)), three distinctive line profiles were manually placed across different regions of the image. These lines were strategically drawn to include the different materials present in the image including the printed PMMA discs, the surrounding water, and the internal air pockets resulting from the partially sealed cylindrical holes within the disc. The objective is to thoroughly evaluate the existence of denser borders with higher HU values in the surface of the printed samples.

2.5. Alternative phantom fabrication approach

Given the challenges faced when printing with high-density PMMA, an alternative approach was proposed. Instead of fabricating a solid phantom fully made of printed PMMA, the possibility of having a phantom shell filled with water or gelatin was explored. As was widely explained in Section 1, water was the first tissue-substitute used through history for safe study of the effects of radiation on humans. On the other hand, gelatin is widely used to recreate or substitute tissue, and it is widely used in tissue engineering, in bioprinting technologies, as a bioadhesive hydrogel, and in biomedical technologies [166-170]. This natural origin protein derived from collagen hydrolysis has proven to possess intrinsic properties for the design of tissue substitutes made with biomaterials [170]. Furthermore, gelatin has caught the eye of bioprinting technologists as it has demonstrated better tissue mimicking features than other bioprintable materials [169]. Regarding its radiological behavior, gelatin has proven to have similar properties as soft tissue but shows limitations since these radiological characteristics change over time [171]. The design for the preliminary tests was a simple box geometry with 2 mm thick walls with dimension 10 x 10 x 2 cm (See **Fig. 14**).

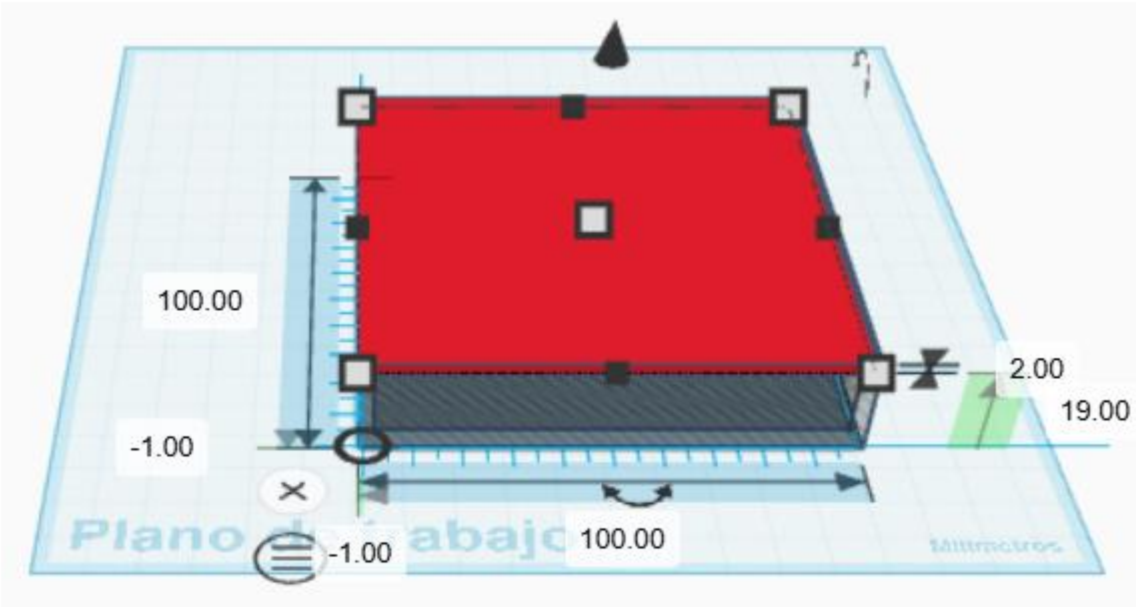

Fig. 14 Preliminary shell-phantom design

Despite the simplicity of the geometry, the initial attempt to print this shell-phantom was unsuccessful. Severe delamination was observed during and after printing with layers easily detaching from each other. The material could not maintain interlayer adhesion resulting in a fragile structure that lacked mechanical integrity and could not be handled without deformation. Therefore, this structure could not be used for testing. **Fig. 15** shows the evident problems mentioned regarding the printing process of the PMMA proof-of-concept shell phantom. Delamination was the major issue, it can be noticed that the phantom could not be handled without breaking apart (**Fig. 15** (a), and (b)). Furthermore, the printed sample that achieved the highest walls (**Fig. 15** (c)), promptly delaminated and exhibited cracks in the structure.

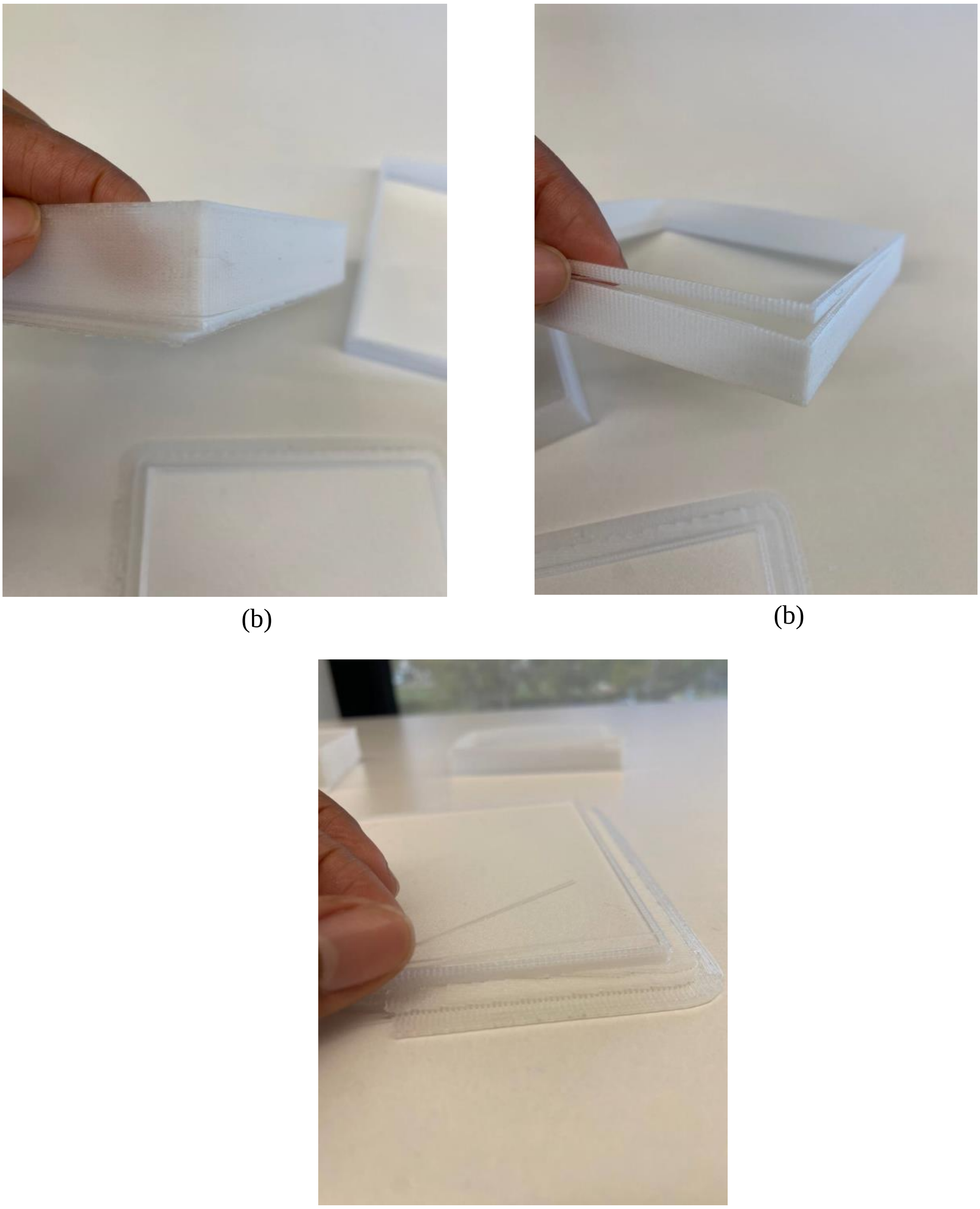

(b) (b)

(c)

Fig. 15 PMMA proof-of-concept shell phantom printing exhibited severe delamination and a fragile structure not suitable for testing

2.5.1. HIPS-Gelatin proof of concept phantom development and evaluation

Due to the challenges encountered, an alternative approach was proposed. Following the previous design proposal, it was suggested to fabricate the piece using High Impact Polystyrene (HIPS) shell and continue with the proposed protocol filling the model with water or gelatin. HIPS has been mentioned in considerations for materials for spectral CT phantoms since it can mimic CT numbers in applications where energy dependence is relevant [172]. Also, printing can be performed with standard protocols. It shows a relative difference of +3 HU to -15 HU to adipose tissue according to Ma et al investigations [172]. Additionally, this material is easily available, compatible with FDM AM, and with the laboratory's printer. Therefore, this strategy holds a promising potential to bypass the printability limitations of PMMA and still achieve suitable CT radiological performance and internal homogeneity.

A preliminary phantom design was printed under the same geometrical specifications in HIPS and two variants of the setting were prepared by filling the shell with either commercially available food-grade gelatin or water and submitted both to CT imaging testing to evaluate the radiological behavior and homogeneity. The gelatin was prepared following manufacturer instructions and allowed to fully set before imaging irradiation. Through CT imaging scan HU values consistency, internal homogeneity, and soft tissue equivalence were assessed. This test served as a proof of concept to evaluate the feasibility of the HIPS-filled phantom approach before advancing to more complex geometries.

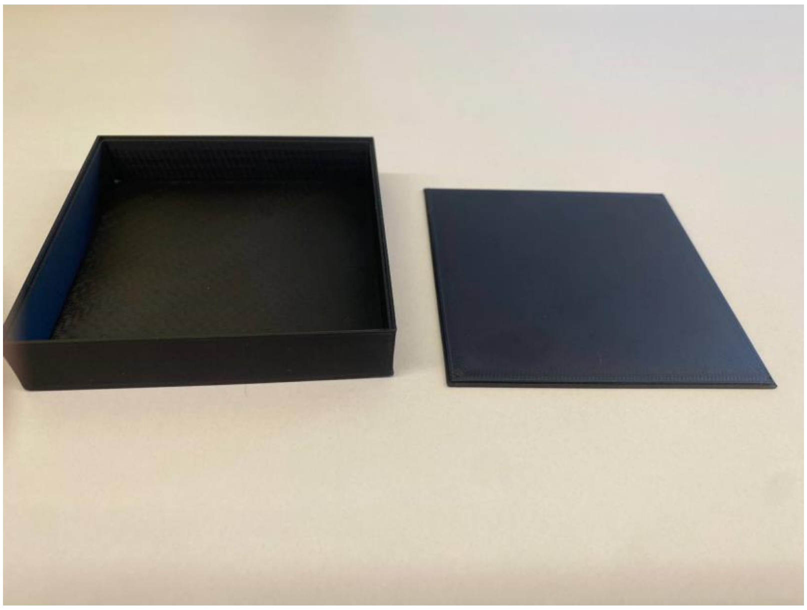

Fig. 16 Printed HIPS proof-of-concept shell phantom

The assessment of the radiological properties of this sample was conducted using the Halcyon – PVA system at Kaunas Oncology Hospital. The imaging protocol was designed to evaluate the attenuation behavior of the composite phantom and determine the approach suitability for the development of complex geometries. The scan was performed with a Cone Beam CT in Head mode with a tube voltage of 100 kVp, exposure of 138.90 mAs, slice thickness of 2.00 mm, and a matrix resolution of 512 × 512 pixels, and the phantom were positioned in air, contrary to the previous scanning of samples which were conducted in water. The phantom was also scanned with both infills, first water and then gelatin. The resulting images were analyzed to examine uniformity of HU distribution within the phantom volume and verify whether this design could reproduce values within the soft-tissue range.

2.5.2. Fabrication and imaging of HIPS head CT shell phantom

Following the proof-of-concept test with the simple geometry box, the next step involved recreating the more complex geometry of the head CT phantom (**Fig. 10**) shell using high impact polystyrene

(HIPS). The geometry of the phantom was based on the previously designed PMMA model with a diameter of 8 cm and a height of 10 cm. The design was printed as a shell, hollow in the inside to be filled with the tissue-equivalent materials. For the evaluation, two configurations were prepared: the first with the phantom filled with water, and a second one with commercially available food-grade gelatin which again was prepared following the manufacturer instructions and was allowed to fully set before scanning.

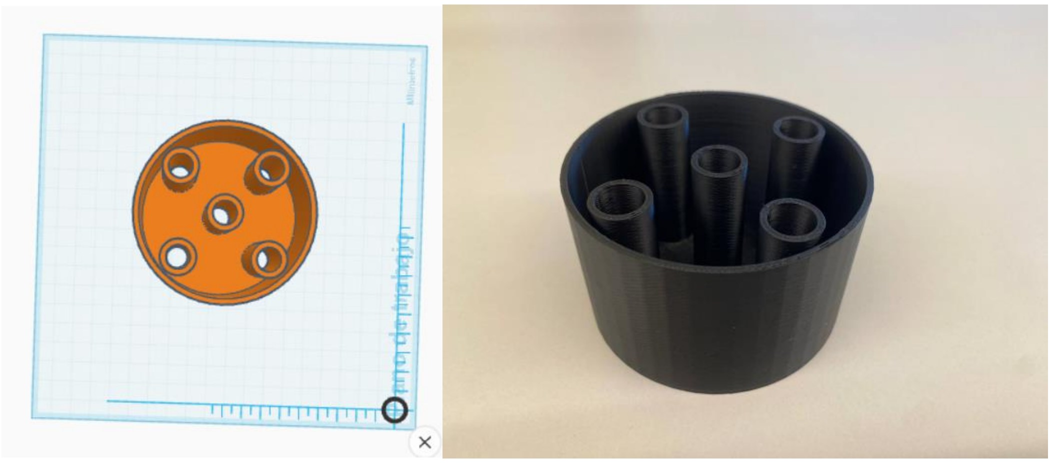

Fig. 17 HIPS head CT shell phantom design and final printed sample

The phantom was scanned following the same settings used previously using the Halcyon – PVA system to produce a total of 193 images. The objective of this evaluation was to assess the internal homogeneity and the attenuation profile of the multimaterial phantom particularly in the interface between HIPS and the infill. The image was analyzed to detect any visible border artifact, significant density gradient or issue that could compromise the QA utility.

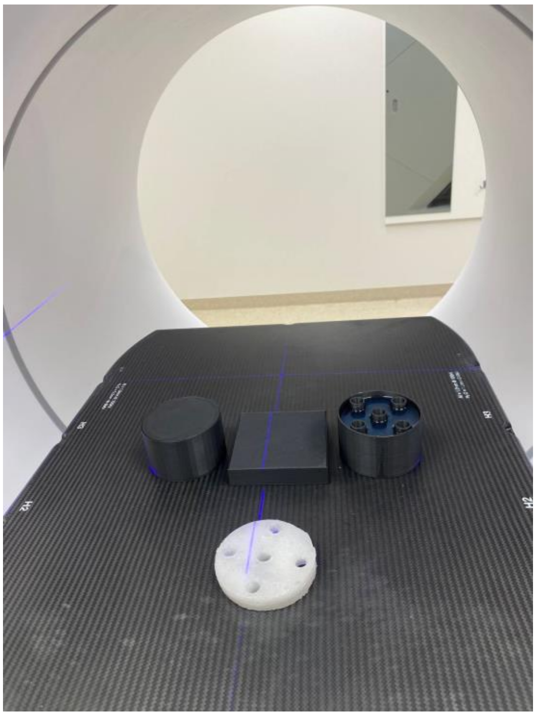

Fig. 18 From left to right (1) dose evaluation phantom (2) proof of concept phantom and PMMA assembled phantom (3) 3D printed HIP phantom positioned in the CT scanner couch for imaging

2.5.3. Dose uniformity test with cylindrical phantom

Evaluation of the dose attenuation uniformity of the HIPS-gelatin phantom configuration was proposed and for this a cylindrical shell phantom was designed, printed, and filled with gelatin. The goal of this test was to assess whether the internal composition of the phantom displayed any dose inhomogeneities that could limit its use in clinical settings. While the geometry of the dose phantom generally mimics the ones of the real head CT phantom and the general configuration of the previous HIPS-gelatin phantom, it is fully void inside.

The model consists of a cylindrical phantom of 8 cm diameter and 10 cm tall, matching the external geometry of the previously printed phantoms. The inner space of the model is completely empty so radiochromic films can be placed inside arrange so as to copy the ionization chamber positions during QA protocols. Once again HIPS was chosen as printing material because of its previously demonstrated radiological characteristics and its compatibility with fused deposition modeling technology.

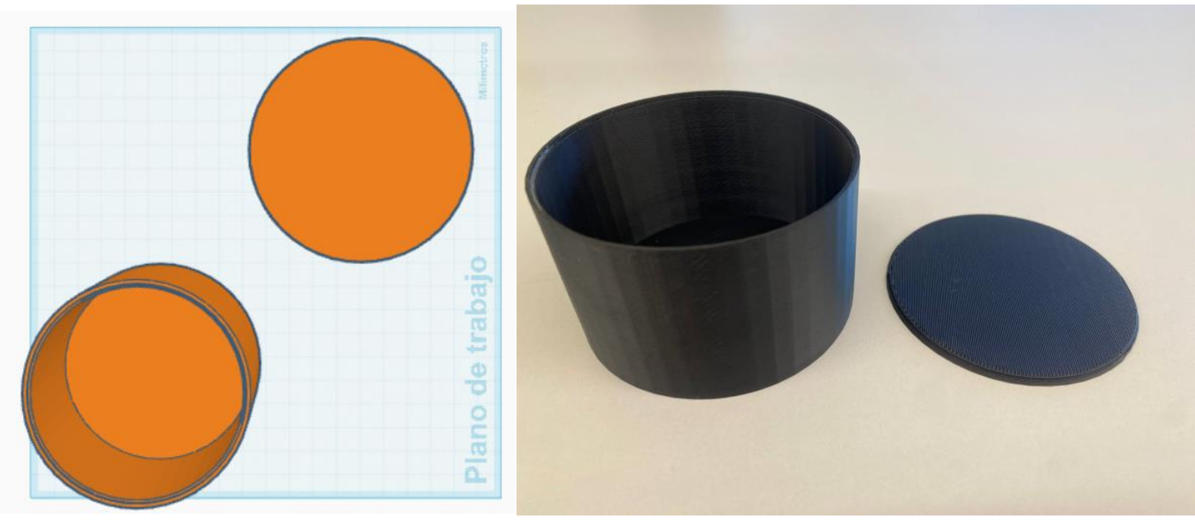

Fig. 19 Design and final printed HIPS phantom model for dose uniformity evaluation

To evaluate dose uniformity, the phantom was filled with commercially available food-grade gelatin that was allowed to set and radiochromic films were placed within the phantom. Radiochromic films are a self-developed dosimeter that, upon irradiation, undergoes a color change proportional to the absorbed dose. These films were positioned in the same positions where the gamma camara would typically be used in QA protocols which would be inside the pre-designed cylindrical cavities intended for dose measurement.

The phantom arrangement was irradiated with a 2 Gy dose using a Gulmay Medical D3225 Orthovoltage unit typically used in superficial and orthovoltage therapy procedures. After irradiation the films were scanned using a regular phone camera and the grayscale values were analyzed using ImageJ to interpret the films response. Rather than calculating the absolute dose, the analysis focused on assessing visual homogeneity of the dose distribution across the film. The goal was to detect patterns, darker or lighter areas, or other distributions that could suggest non-uniform dose distribution and inconsistencies within the printed structure.

Fig. 20 The cylindrical HIPS-gelatin phantom was exposed to a 2 Gy dose for evaluation of attenuation consistency using radiochromic films

3. Results

As per the original design based on Kyoto Kagaku head CT phantom, the printed design included 5 cylindrical holes used for dose evaluation during QA protocols. These holes were designed to be open as the gamma camera is positioned in them to perform internal measurements. However, due to the layer adhesion issues during printing, some of these holes were partially sealed and in the scans it can be seen that air is trapped inside. Air pockets are visible in CT scanning as a very dark region within the sample indicating that water had not entered. While this finding does not serve any intended purpose in this particular case, it demonstrates the feasibility of incorporating air cavities into 3D printed PMMA devices which could be advantageous for future devices designs requiring such characteristics and thus expanding the applicability of this printing technique.

3.1. Evaluation of the correlation between infill density and radiological attenuation properties and shell effect in PMMA prints.

The evaluation of the printed PMMA samples involved scanning them using the Halcyon LINAC cone-beam computed tomography (CBCT) system. The three samples with infill densities of 10%, 50%, 100%, alongside a PMMA slab which served as a reference for comparative evaluation were scanned and analyzed (**Fig. 21**). A preliminary qualitative visual assessment of the three printed samples along with the commercial PMMA slab was conducted. From visual inspection it becomes evident that the 10% infill sample lacks the density necessary to be considered a viable phantom substitute. In the CT scan it appears almost completely black, indicating that it is mostly void or composed of air in the inside rather than material. Therefore, it is not suitable for mimicking soft tissue. On the other hand, the 50% infill cube, although slightly opaquer, still exhibits insufficient density and does not resemble the attenuation profile of the reference PMMA slab. In contrast, the 100% infill sample shows way better radiological attenuation and similarity with the commercial slab. It also appears homogeneous through its volume and not visible layering typically associated with additive manufacturing can be easily distinguished. These observations suggest that at least visually, the 100% infill configuration is the most promising sample in terms of structure and attenuation behavior.

To quantitative analyze the performance and uniformity of each printed sample, an image-by-image analysis of the HU was performed. For this, an evaluation of each axial CT image was carried out by extracting the average HU value across the sections of each printed sample. This method was applied to all relevant images covering the full volume of the 10%, 50%, and 100% printed samples as well as the PMMA reference slab. From this, two comparative graphs were plotted, one comparing the mean HU values between the 10% and 50% infill samples and the second one comparing the 100% infill sample against the commercial PMMA slab. This arrangement for comparison was selected given the similarity and trends in the attenuation behavior of each structure, this allows better visualization of how infill density impacts on the radiological behavior.

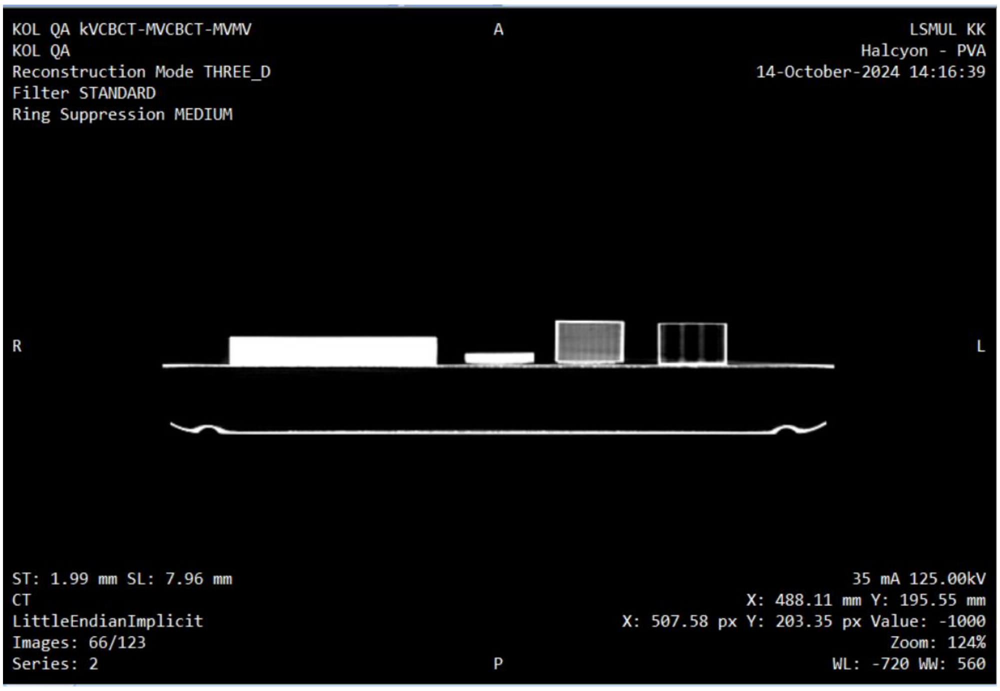

Fig. 21 CT scan of three samples with infill densities of (from right to left): 10%, 50%, 100%, and a PMMA slab

The first plot, exhibited in **Fig. 22**, compares the 10% and 50% infill samples. Both curves display extremely low HU values across their internal layers with an average of -705.8 HU for the 50% infill sample and -933.3 HU for the 10% infill sample. These results are consistent with low-density materials infills as they are mostly air. The 50% infill sample shows slightly higher HU throughout its profile than the 10% infill one. However, either of them is suitable for tissue mimicking replacement. Notably, both curves show a marked peak in the first and last segment, these regions achieved the higher HU in the whole volume and suggest that the density of the outer shell of the printed samples is denser than the infill regardless of the printing settings specifications for infill density.

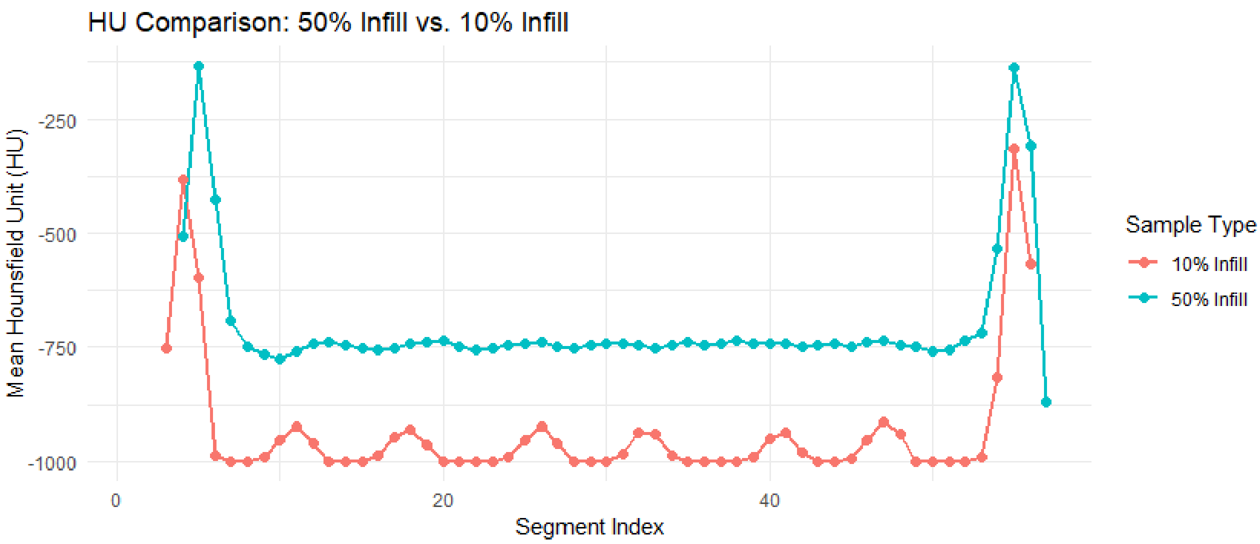

Fig. 22 Comparison of attenuation properties: 50% infill printed sample vs. 10% infill printed sample

The second plot, visible in **Fig. 23**, compares the 100% infill sample with the commercial PMMA slab. The commercial slab shows a stable HU distribution centered around +123 HU with minor fluctuations within its layers. The 100% infill sample also shows greater variations in its HU distribution with an average of +15.2 HU and maximum of +117.9 HU. The curve shows a U-shape profile where the central layers appear less dense than the outer layer, phonomenon that was previously saw in the low-infill samples. This shell effect may have implications for edge effects in imaging and should be further investigated. Despite this, the printed sample value falls within the acceptable range for soft tissue mimmicking. Its inner layer fluctuations suggest potential inconsistencies during the printing process such as thermal gradients or interlayer adhesion issues that shall be evaluated in further detail.

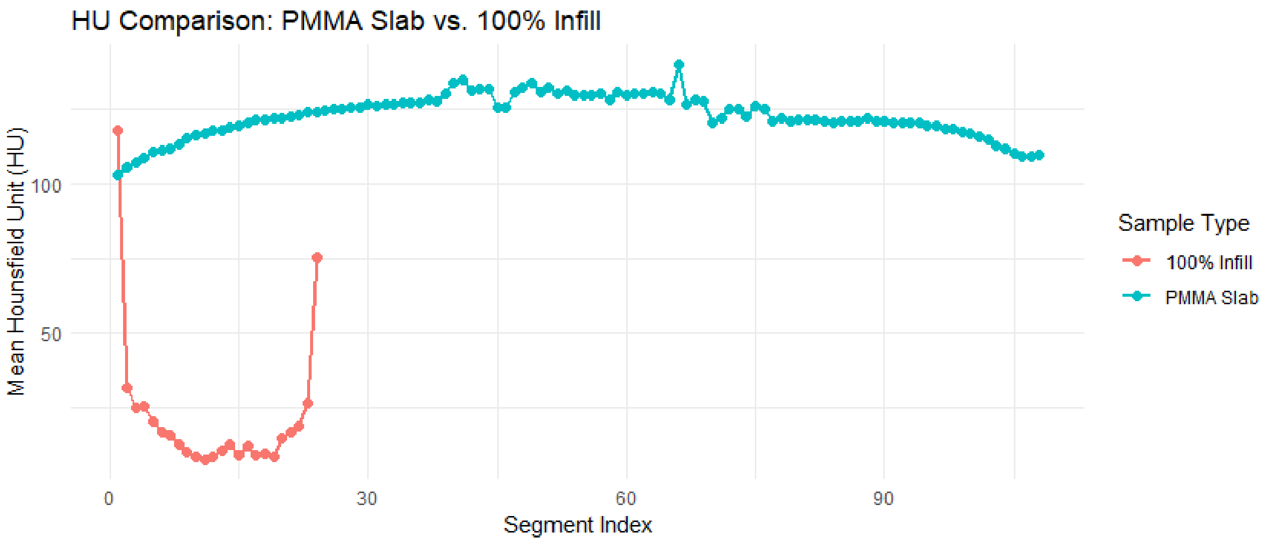

Fig. 23 Comparison of attenuation properties: PMMA commercial slab vs. 100% infill printed sample

All printed samples, regardless of the infill percentage, exhibited higher HU values in their outermost layers which suggest increased density in these layers or print surface which can by hypothesized is due to over extrusion at the initial layers or a reconstruction artifact in CT scanning.

Despite the many advantages offered, printing with PMMA using FDM technology presented several technical challenges. The material's viscosity showed to be prone to increasing the risk of nozzle clogging, particularly during long printing sessions or if the printing temperature was not yet set as required. To overcome this inconvenience, regular nozzle cleaning and periodic replacement were required. Moreover, 100% infill prints have the tendency to deform, shrink, and warp during the cooling face. To try to counteract these effects, several corrective measures were adopted: the bed temperature was increased to allow for better material adhesion as poor adhesion resulted in delamination and distorted prints, extrusion parameters were carefully optimized through trial and error to enable stable material flow, the printing speed was also corrected to a slower one to allow for better interlayer adhesion. Modification of the design of the printed piece proved to be useful as increasing the surface area in contact with the printer bed reduced deformation defects. After these preliminary testing and parameter tuning, the printing protocol was established as:

Table 7. Printing protocol for 100% infill PMMA models

Parameter	Value
Printer	Zortrax M300
Material	Glass-type filament
Nozzle diameter	0.4 mm
Layer thickness	0.14 mm
Infill	100% (solid)
Extrusion temperature	245 ℃
Platform temperature	80 ℃
Printing speed	Adjusted as needed

Unfortunately, none of these configurations produced complete prints. In many cases, nozzle clogging, layer separation, or warping occurred mid-print, making the sample unusable. Several of these prints are shown in **Fig. 24**.

Fig. 24 Examples of 3D printed PMMA samples with 100% infill. All samples show material disruption at approximately 1.5-2 cm

3.2. Analysis of HU values within and between materials

Submerging the samples in water was proposed to reduce the influence of edge-related artifacts and ensure a relevant evaluation of the radiological behavior of the samples. Therefore, all scans used for quantitative analysis of the samples were performed under water. This approach significantly reduced the appearance of artificial HU peaks reported in previous studies as water creates a uniform soft-tissue equivalent that improves transitions between materials and avoids misinterpretations.

A thorough analysis of the HU distribution across the three different materials, PMMA slab, printed sample, and water, was conducted. **Fig. 25** shows a box plot graph where each point represents one ROI, each box is the interquartile range (IQR) or middle 50% of values, and the central line denoting the median HU per material is represented to give insight into material consistency and radiological performance. The PMMA slab acts as a reference standard and shows a median HU around 90-100, with most segments falling within a reasonably range, some low outliers are visible maybe attributed to image noise or artifacts. Whilst this material shows fair consistency with commercial expectations (+100 to +140 HU), slight variations indicate heterogeneity or scanner noise. The printed sample exhibits a slightly lower median and a broader distribution with values that range from 30 to 140 HU, slightly higher than PMMA slab. This spread may suggest infill inconsistencies or irregularities between layers. However, the central cluster falls well within the soft-tissue-equivalent range. This suggests that further investigation and post-processing techniques might help in improving its performance to make it more comparable to the reference PMMA standard.

On the other hand, the water regions display a way lower median of HU values centered near 0 as is expected. The broad spread which includes both positive and negative values, could be a result of partial volume effects, or scanner noise. Regardless of this, the central tendency remains consistent with the known radiological characteristics of water under CT. Overall, this quantitative study confirms that 3D printed PMMA approximates to the radiological behavior of commercial PMMA with slightly greater variability. It is suggested that post processing of the samples like heat treatment, or chemical dipping could improve the bonding between layers and increase the achievable HU values.

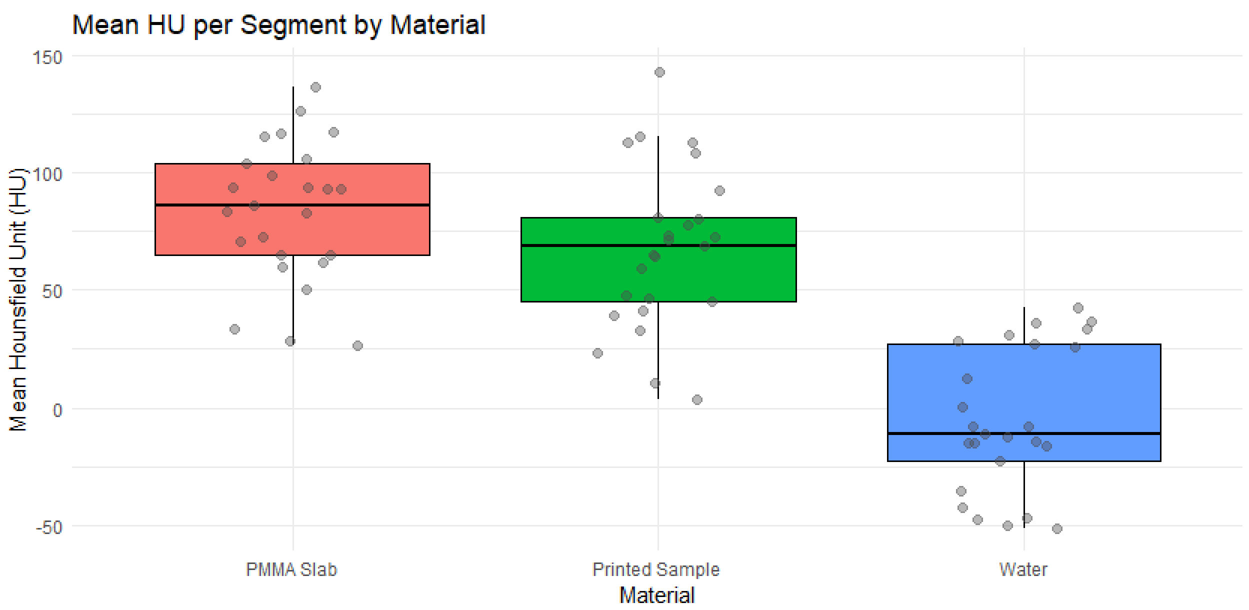

Fig. 25 Distribution of HU values for commercial PMMA, printed sample, and water

Later, a line profile analysis was conducted to evaluate any variation in HU across the printed disk with particular interest in assessing whether a denser outer shell exist as it was hypothesized in previous studies. A line of approximately 136.2 mm line was manually placed across the CT images in the two separate scans (**Fig. 13** (b)). Evenly spaced points were samples along the line and their corresponding HU values were extracted, the result of this profile evaluation is shown in **Fig. 27**.

The initial portion of the line presents the lowest values which is consistent with water. Then, the transition into the printed disc is clearly visible given the sharp increase in HU values at around 25 mm and peak around 80-120 HU. The value is maintained across the central disc portion which goes from approximately 25 to the 95 mm mark. The internal region of the disc seems to show considerably variations in HU values which again is consistent with the finds in the previous study of this section which suggested that print inhomogeneities, or CT noise was present. However, no abrupt spikes or sharply defined higher density outer shell regions are observed and the object shows a relatively uniform internal structure than challenges the hypothesis of the existence of a denser outer shell proposed in previous works.

A second drop in HU values is seen around the 95 mm mark, consistent with the ren-entry into a water region. Finally, beyond the 110 mm mark, the profile value range between 110 HU and 130 HU which perfectly aligns with the expected values of commercial PMMA slabs. This final region validates the presence of the reference phantom slab and supports the overall interpretation of the profile.

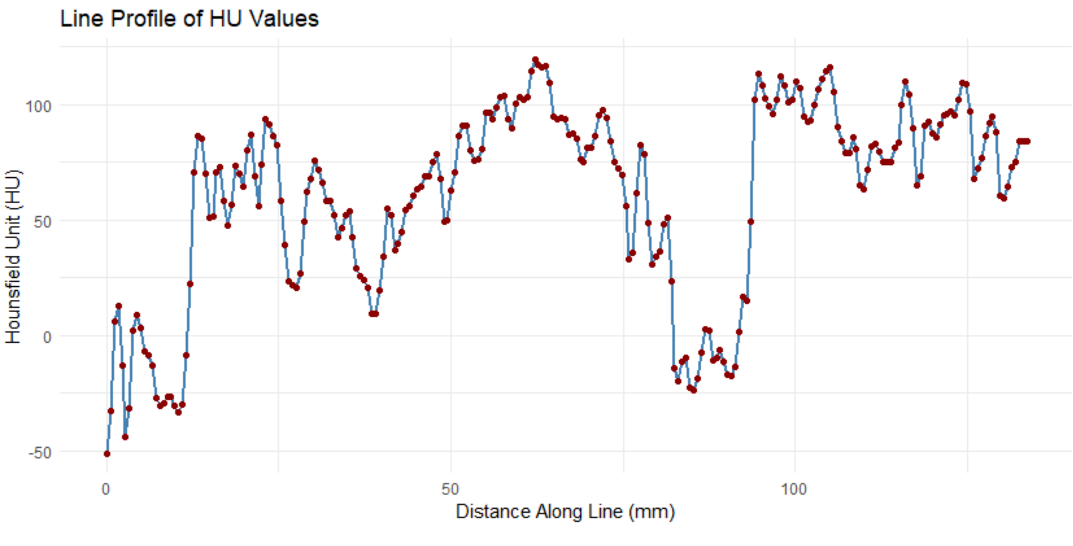

Fig. 26 Line profile of Hounsfield Unit (HU) values sampled along a 136.2 mm line drawn across the different materials of the CT scan corresponding to **Fig. 13** (b)

The second scan (**Fig. 13** (c)) includes multiple printed PMMA disc samples submerged in a water tank. In this scan three line-profile were drawn across separate discs to assess consistency in the evaluation of the potential boundary artifacts. The line profiles were analyzed following the same protocol as before. A line of 136.2 mm was drawn in the areas of interest and the HU were assessed over evenly separated points of this line. The results are exhibit in **Fig. 27**.

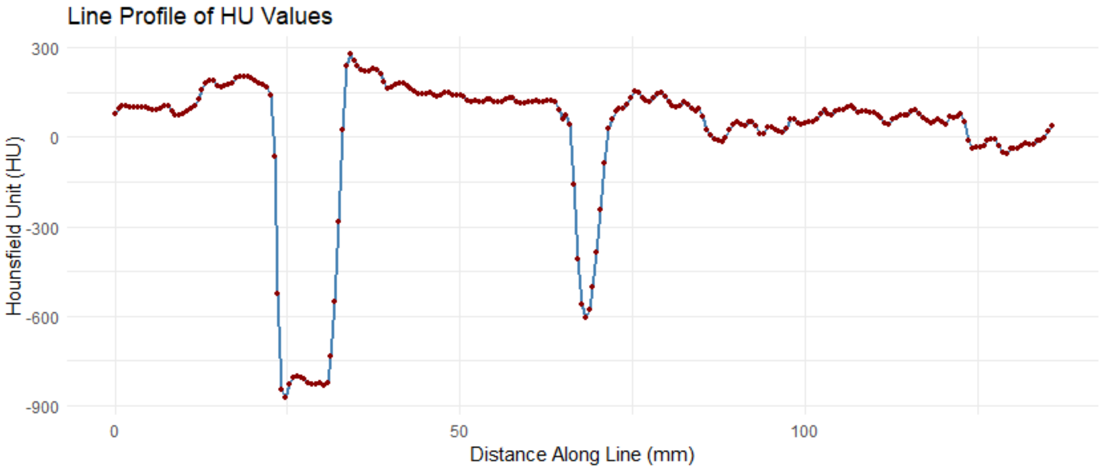

(a)

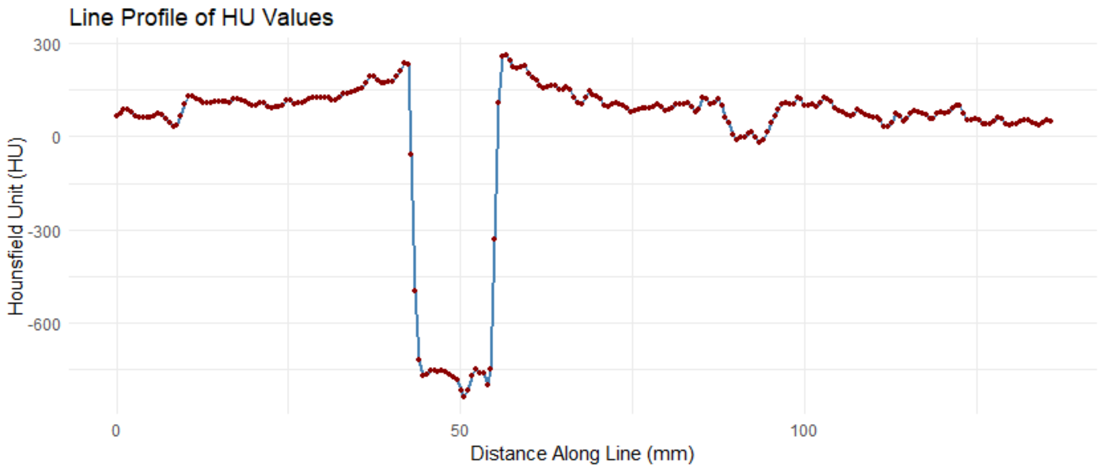

(b)

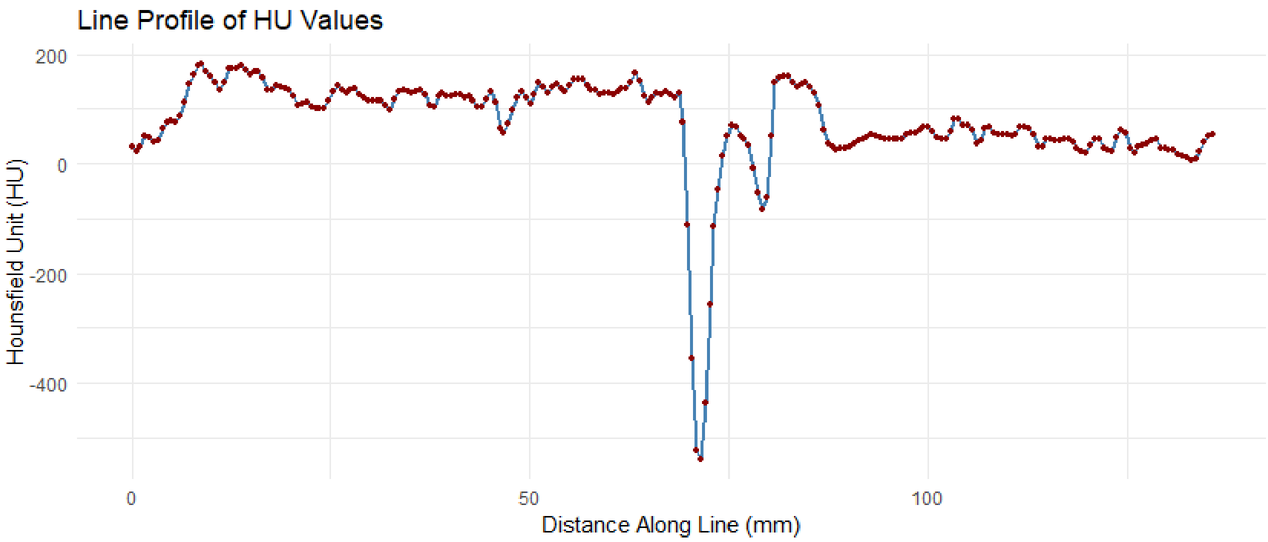

(c)

Fig. 27 Line profile of Hounsfield Unit (HU) values sampled along a 136.2 mm line drawn across the different materials of the CT scan corresponding to **Fig. 13** (c).

The general patterns in this set of plots show consistent radiological behavior in the water regions where the HU values cluster around 0 HU providing a reliable baseline. The internal regions exhibit values ranging from +50 HU to +150 HU which aligns perfectly with the expected values for PMMA. However, the PMMA disc regions show inhomogeneous behavior and greater variability than what has been observed in commercial PMMA. This result, while not ideal for the purpose of medical application, aligns with previous observations and sustains the suggestion that post-processing of the printed samples may improve consistency in HU values. Notably **Fig. 27** (a) and **Fig. 27** (b) exhibit sharp positive peaks in HU at the borders between the printed disc and the air-filled cavities. Interestingly, these peaks are absent in the water-printed sample borders.

This behavior seen in different discs suggests that the previously identified denser outer shell in the printed samples is most likely the result of a CT reconstruction artifact and not a physical border caused by the 3D printing technique. The denser layer seems to particularly appear in the transition from air to a solid object producing an overestimation of the HU values in the region due to how the CT reconstruction algorithms interpolate edge voxels. The absence of this effect in the PMMA-water border, visible in the qualitative evaluation of the first CT imaging in **Fig. 27**, further support this interpretation.

To further investigate the nature of these edge effects, additional attenuation profiles were plotted along the borders in the regions of transition between printed PMMA material and air, and printed PMMA material and water. This more detailed analysis, showed in **Table 8**, revealed that the sharp edges artifacts are consistently present in the air-material zones while significantly absent in the water-material borders, reinforcing the conclusion that this effect is due to CT reconstruction artifacts rather than physical densities differences.

All things considered, this profile confirms that HU values vary in a predictable manner across the present materials, the print disc shows radiological properties consisting with PMMA but also shows variations that could be associated with inhomogeneity, and most importantly, there is no evidence of a denser outer shell that previous observations suggested but attributes the previous observations to image reconstruction artifacts in the air-material boundaries. These findings serve as a recommendation in further studies in radiological properties of materials to use a medium material for true analysis of the structures and to avoid possible misconstructions during the imaging process that leads to misinterpretations.

3.3. Assembled phantom evaluation

To explore the feasibility of assembling a full-scale phantom by gluing the printed components, a prototype was fabricated by stacking and gluing several PMMA printed discs. This approach aimed to achieve the desired z-axis geometry that was limited by the 100% printing restrictions. However, the resulting phantom displayed notable shortcomings both in structural and radiological characteristics. A visual evaluation of the CT image (**Fig. 28**) easily reveals a clearly layered structure alternating bands of higher and lower density materials creating the appearance of a “layered cake” that correspond to the PMMA and the glue used to adhere the components.

Table 8 Evaluation of border effects in air-printed PMMA (left) and water-printed PMMA (right) transition areas

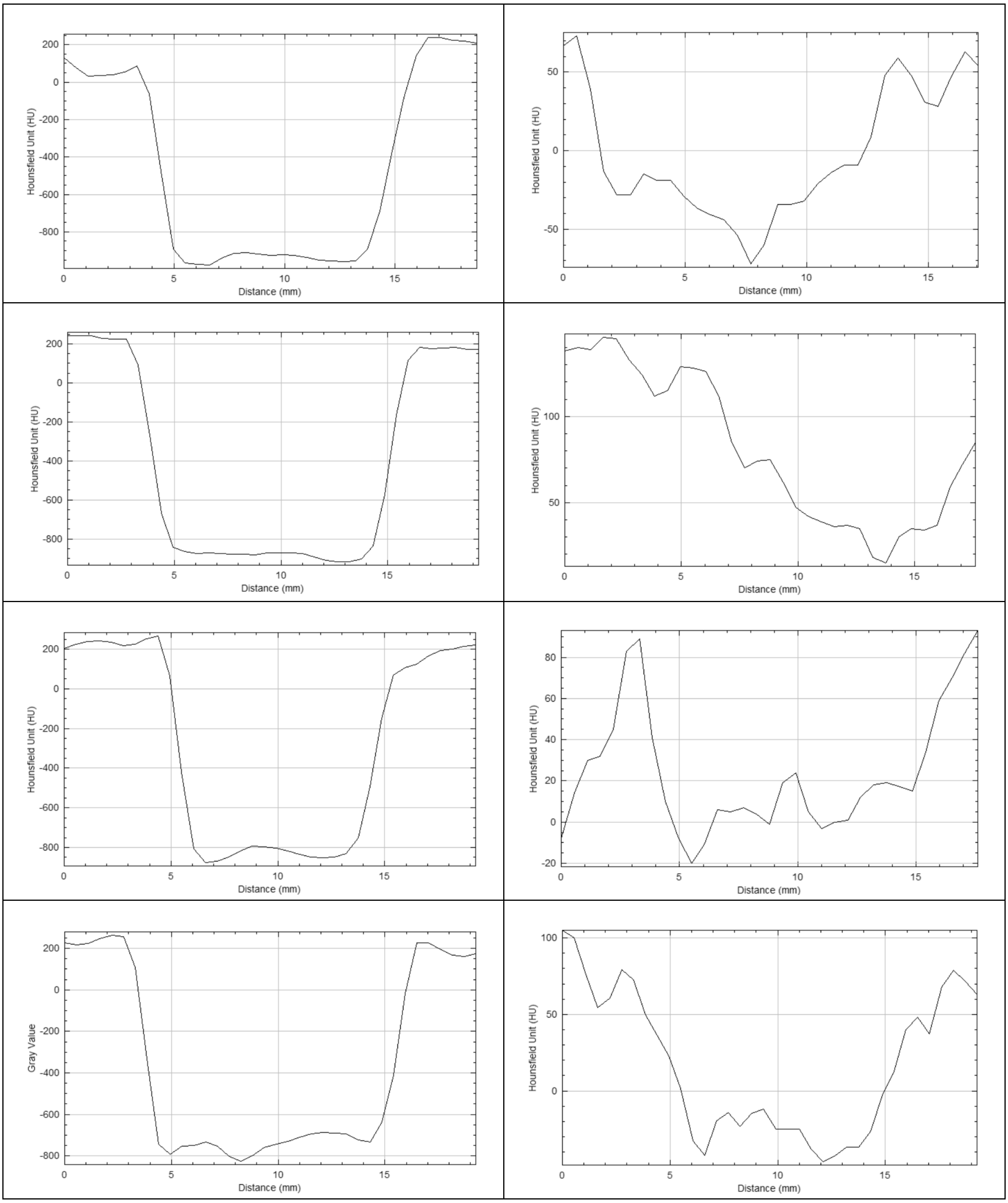

A HU profile analysis was also conducted to further validate the visual assessment (**Fig. 29**). The plot shows pronounce variations in the attenuation values along the length of the scanned phantom. The acrylic adhesive used for the assembly shows higher values, surpassing the PMMA segments surprisingly. This “layered cake” effect goes against the goals of the in-house build phantom of resembling homogeneity and radiological uniformity and therefore it is not suitable for clinical uses. These findings highlight the crucial limitations on multi-part assembly for phantom fabrication. This technique seems unsuitable to produce clinically relevant phantoms as it clearly demonstrates non-uniformity and density layering but also reinforces the importance of single-piece constructions or alternative methods such as multimaterial composition that exhibit same or very similar radiological characteristics.

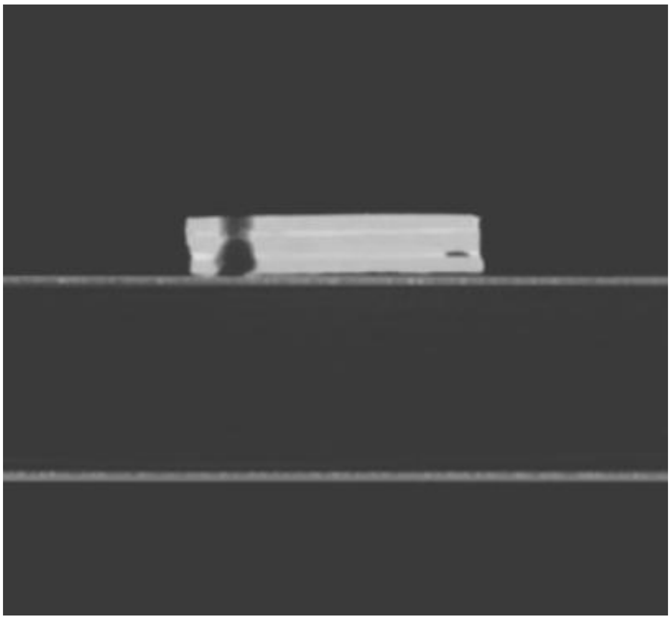

Fig. 28 CT image of the assembled phantom made of printed PMMA discs and acrylic glue

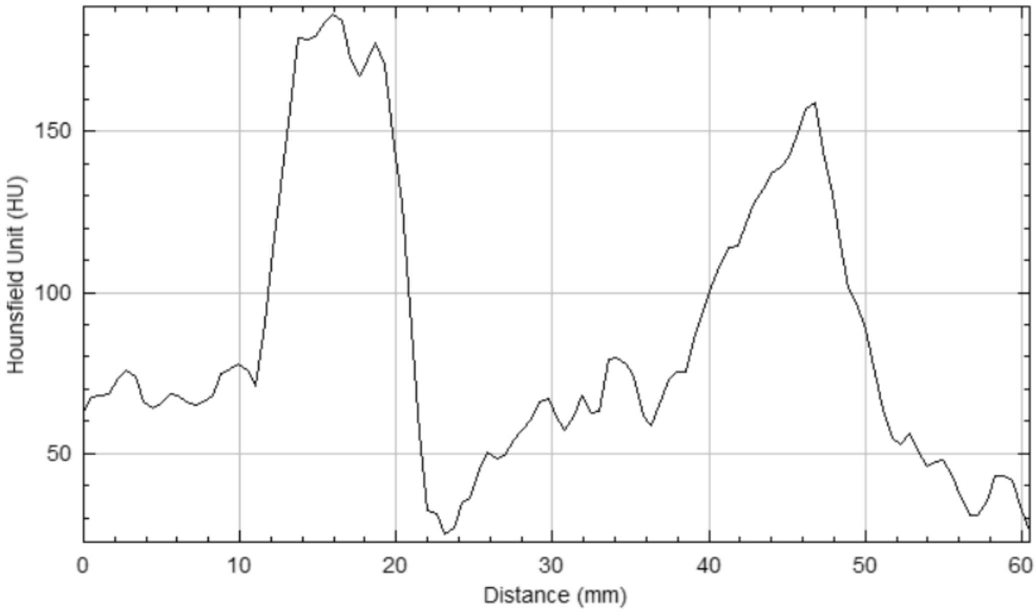

Fig. 29 HU values profile of assembles phantom made with printed PMMA prints and acrylic glue

3.4. Multimaterial HIPS phantoms assessment

3.4.1. Proof -of-concept evaluation of HIPS-water phantom

This proof-of-concept phantom served as a foundational test to evaluate the feasibility of fabricating multimaterial structures with 3D printed HIPS shell and a homogeneous filler. The first configuration was a HIPS-water phantom. Water was chosen due to its proven radiological similarities to soft tissue and availability. Then, a second configuration was developed to further explore the versatility of this approach, this second configuration consisted of the same 3D HIPS shell now filled with commercially available food-grade gelatin which was already established has similar radiological properties to tissue and water. This progression from water to gelatin allows us to investigate different materials applicability in imaging studies.

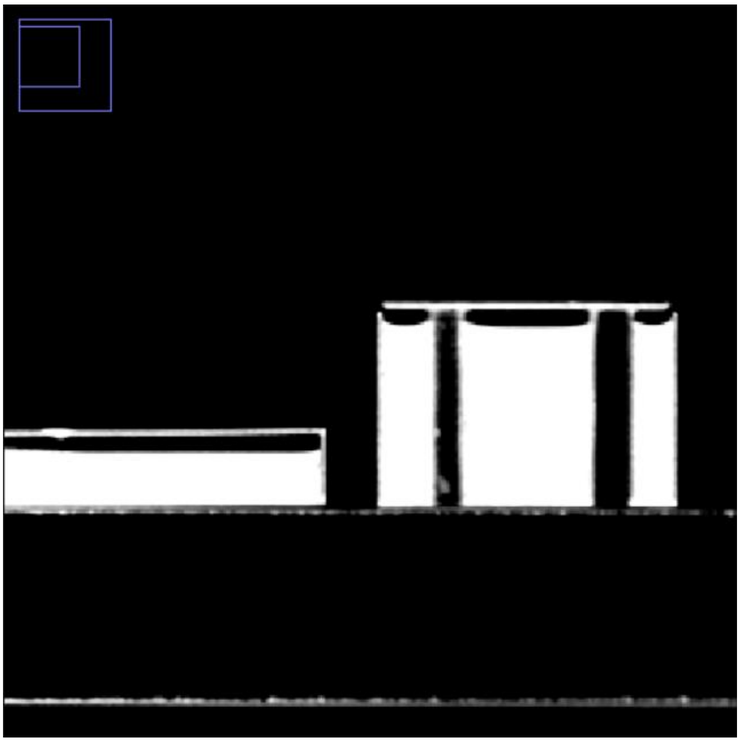

Fig. 30 Axial CT slice showing the proof-of-concept phantom (left) and the head CT phantom (right) both fabricated using HIPS shells and filled with water

A visual evaluation of the axial CT image shown in **Fig. 30** and located on the left side reveals a simple and radiological coherent geometry. The phantom consists of a box made in 3D printed HIPS and filled with water. The external boundaries appear well defined with no sign of warping or deformation which indicates successful printing and dimensional stability. Internally, the phantom shows uniform grayscale distribution with no visual air bubbles or other alien bodies or layering effects. This uniformity suggests promising radiological performance. Moreover, there is no visible material layering, stratification or artifacts visible. The visual evaluation of this simple model demonstrates enough uniformity to move to a detailed quantitative evaluation.

As a complement to the visual assessment, a qualitative evaluation was performed. Firstly, a line profile was carried out to evaluate the edge and material transition effects. For this, a straight line was manually drawn across the phantom in the Axial CT image and the HU values were extracted across its length. The results are shown in **Fig. 31** and it is consistent with expectations. The plot begins near

– HU which is consistent with air outside the phantom. Upon entering the printed HIPS shells, a sharp increase is observed which rapidly stabilizes around 0 HU which is characteristic of water. The curve does not exhibit any notable boundary between shell and infill which supports the uniformity visual assessment. This lack of boundary in the HIPS-water transition is highly important as it indicated that the CT scanner interpretates the structure as a unified, homogeneous entity and not a composite of discrete materials. Therefore, no material interface artifacts can be attributed to this configuration.

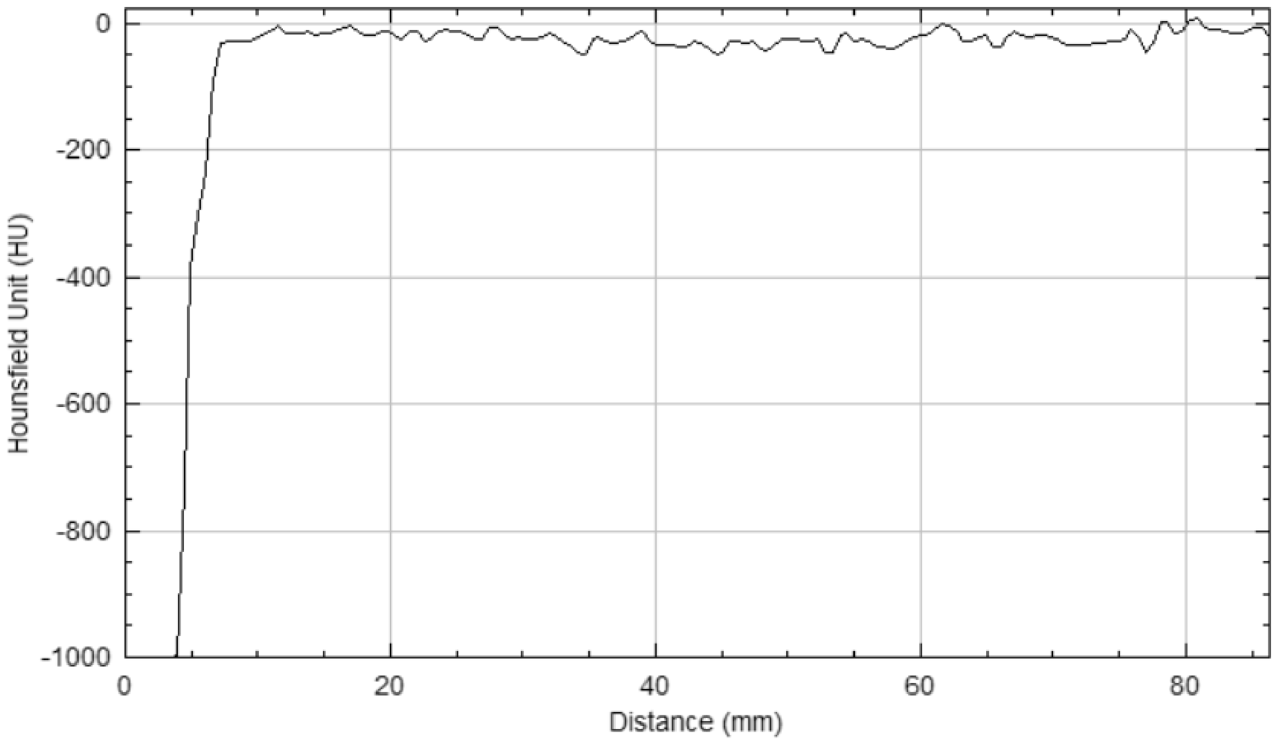

Fig. 31 Line profile of the multimaterial HIPS-water proof-of-concept phantom for evaluation of material interface

Furthermore, the interior of the phantom shows minor fluctuations that indicate good uniformity throughout the volume and shows that the phantom does not exhibit density variations or imaging artifacts either in its core or its outer shell reinforcing the viability of this approach for producing simple phantom geometries with relevant radiological features. A more exhaustive analysis of the internal properties and characteristics of the HIPS-water configuration was performed and is displayed in **Fig. 32**. The first plot (**Fig. 32** (a)) exhibits the attenuation profile across the interior of the HIPS-water phantom and reveals that the HU values fluctuate from around -10 HU and -45 HU. However, sharp peaks or voids are not observed which suggest general homogeneity. Furthermore, the variations observed are relatively small in magnitude and not relevant. The lack of pikes and voids also supports the visual assessment that suggested that no significant air bubbles, material inclusions, or layering artifacts are present in the volume. The gentle oscillations in the curve are well within the acceptable limits, sustaining the suitability of the HIPS-water configuration as a tissue-mimicking material system for phantoms particularly in cases where consistency and uniformity are crucial parameters.

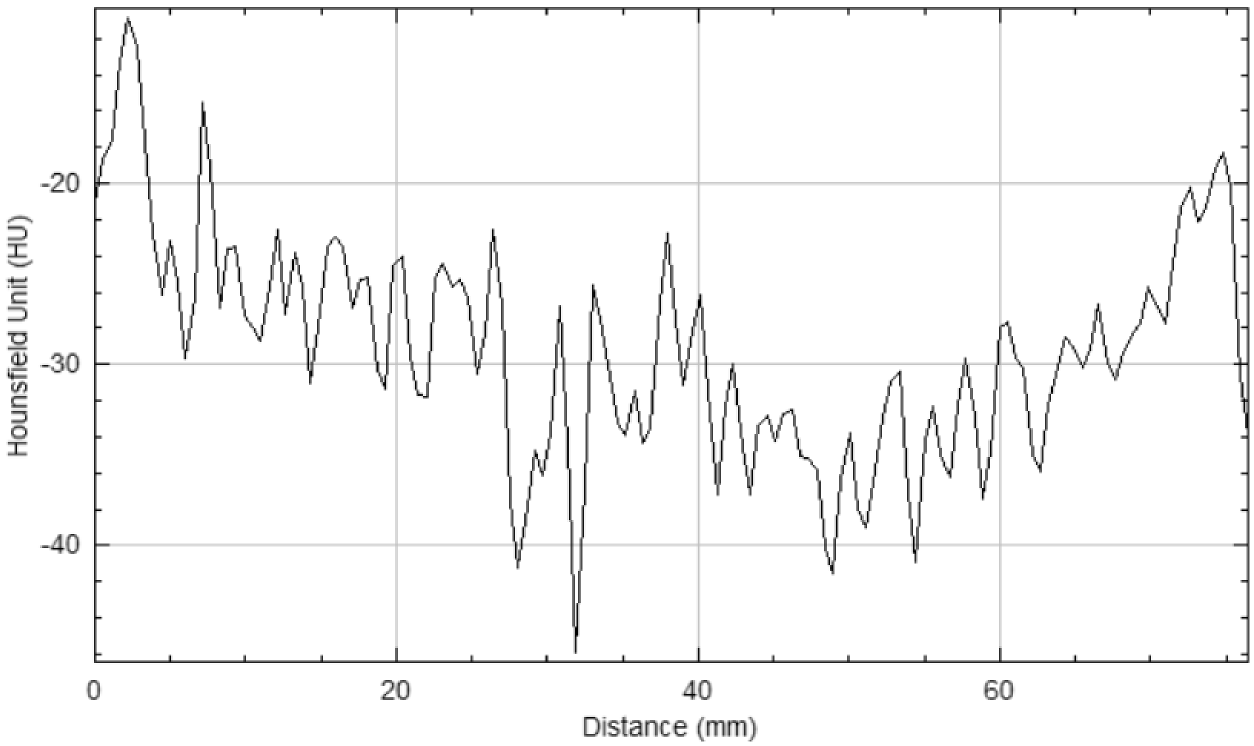

(a)

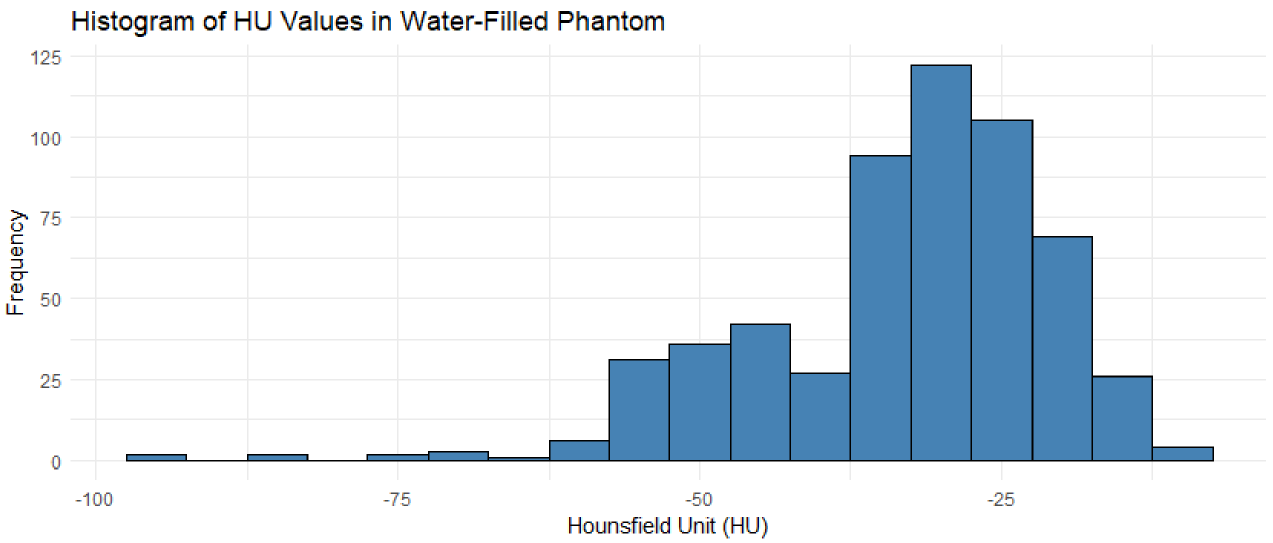

(b)

Fig. 32 Evaluation of internal radiological behavior of the HIPS-water proof-of-concept phantom (a) ROI profile showing the mean attenuation characteristics of the phantom (b) histogram of HU values within the internal volume.

Fig. 32 (b) shows the histogram of the distribution of HU values within the proof-of-concept HIPS-water phantom. For this analysis grayscale intensity values were extracted over several rectangular regions of interest (ROI) over the inner volume of the sample. The distribution of the data appears approximately normal with the majority of the values concentrated around -30 HU indicating that the dominant attenuation values are slightly below the expected value of 0 HU for water. Despite the large right skew, the histogram shows a well centered distribution suggesting high degree of radiological uniformity. The values fall within a range of 40 HU and there is not a notable secondary peak indicating reliable attenuation performance for medical imaging applications.

3.4.2. Proof -of-concept evaluation of HIPS-gelatin phantom

In **Fig. 33** the leftmost object corresponds to the proof-of-concept phantom filles with gelatin. Visually the phantom looks very similar to its water-filled counterpart and appears to have consistent gray scale distribution suggesting good homogeneity. The interface between the HIPS shell and the inner gelatin infill appears smooth and with no noticeable difference supporting good compatibility between the printed shell and the gelatin infill.

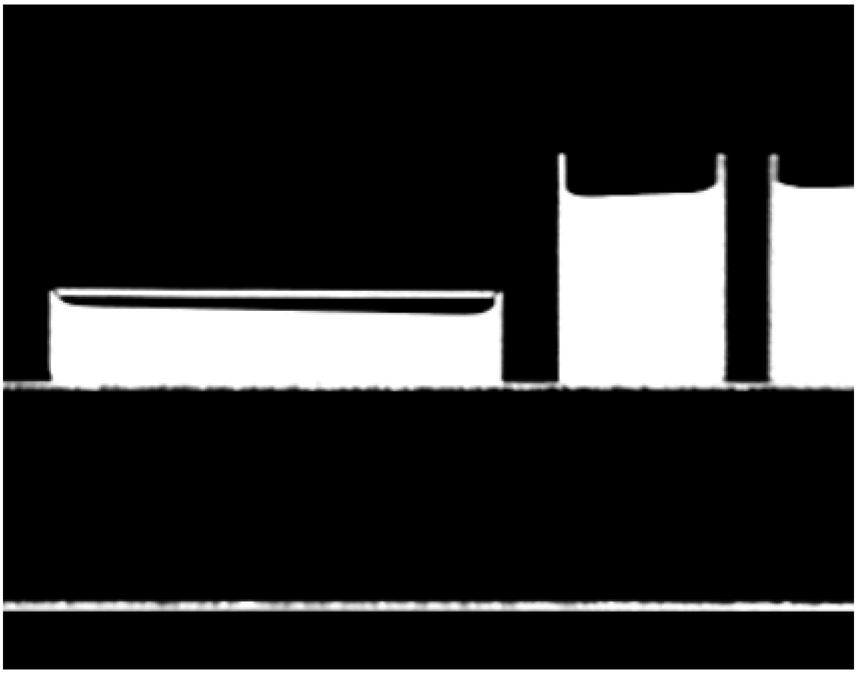

Fig. 33 Axial CT slice showing the proof-of-concept phantom (left) and the head CT phantom (right) both fabricated using HIPS shells and filled with gelatin.

Notably, gelatin appears concave in its surface which is common for this material and it is due to surface tension during setting and does not have any implication on the internal homogeneity. Again, there is no internal layering or structural separation that could create air bubbles or translate as geometry defects. Also, the phantom appears cohesive and uniform.

The attenuation profile of a line cross-section for the gelatin filled phantom was manually drawn and was obtained to assess for the radiological behavior across the multimaterial border (**Fig. 34** (a)). The values being near -1000 HU which corresponds to the surrounding air region outside of the phantom. As the line enters the structure there is a rapid sharp increase that quickly stabilizes around -10 HU through the internal volume. The stability of the values within the volume indicates excellent homogeneity and most importantly, both left and right multimaterial transition areas show smooth boundaries and continuous material interface between the HIPS shell and the gelatin. This is essential for applications where uniform CT number distribution is key. The lack of internal peaks or valleys further supports the suitability of gelatin to mimic uniform soft-tissue. In general, this profile supports that gelatin filling maintains radiological uniformity and shows no border effects

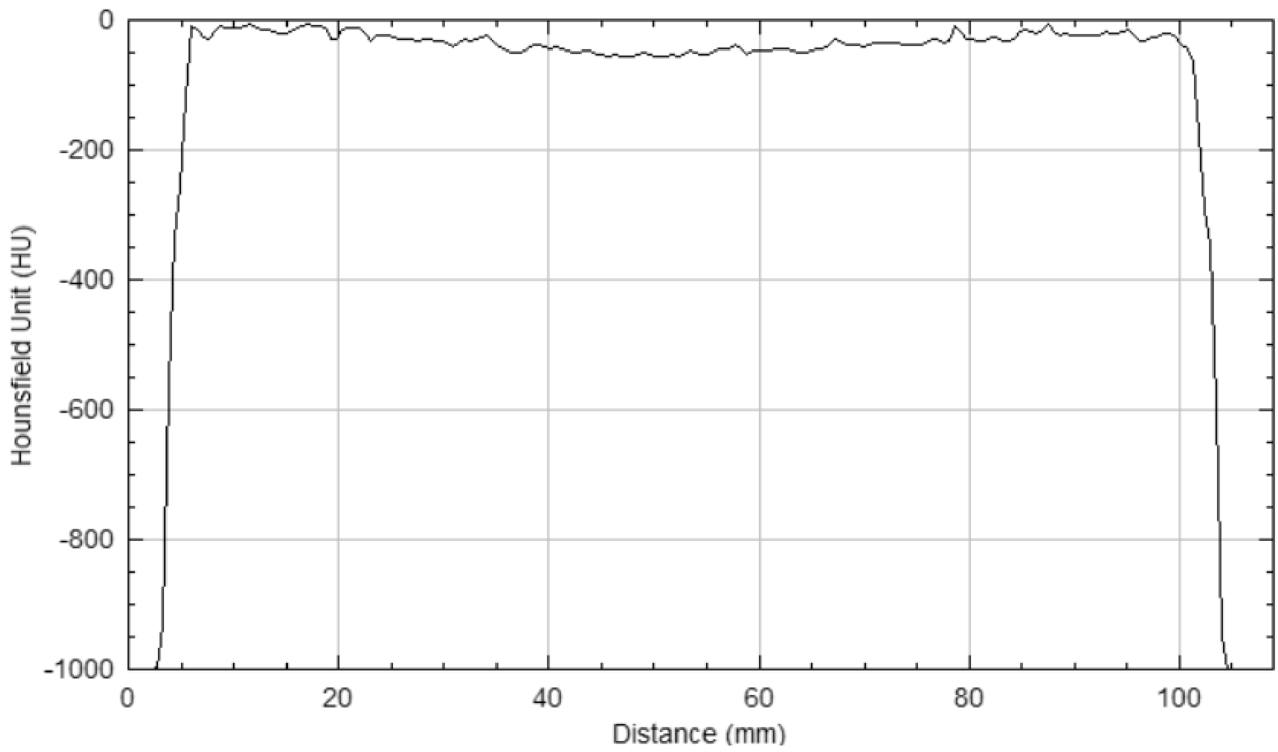

Fig. 34 Line profile of the multimaterial HIPS-gelatin proof-of-concept phantom for evaluation of material interface.

It is also worth noting that the line profile displays a slight concave shape with marginally higher HU values than in the central region. While this variation is minor, it can be further investigated in the inner volume profile and HU distributions histograms of this HIPS-gelatin phantom. A ROI was taken from the inner volume of the phantom, its HU profile was plotted, and it is visible in **Fig. 35** (a). This graph reveals a concave shape attenuation pattern across the gelatin filled proof-of-concept phantom with HU values ranging from around -20 HU to -50 HU in the central region suggesting potential density gradient in the material. This effect could be attributed to cooling induced effects during the gelatin cooling process.

The HU histogram obtained from the phantom inner volume (**Fig. 35** (b)) displays a wide distribution ranging from approximately -50 HU to +20 HU. This variation indicates inhomogeneities within the material. While the values remain within the tissue mimicking range, these findings suggest that further refinement in the infill preparation process is needed. The histogram reveals a bimodal distribution rather than a single sharp peak where a significant part of the values range in the negatives and there is rise in frequency observed between 0 and + 20 HU. Al these results suggest local variations or minor structural inconsistencies. These variations in distribution reveal limited homogeneity within the gelatin infill and could be attributed to possible temperature inconsistencies during the gelatination process, chances in the concentration gradient of the gelatin during the cooling phase or other material related issues.

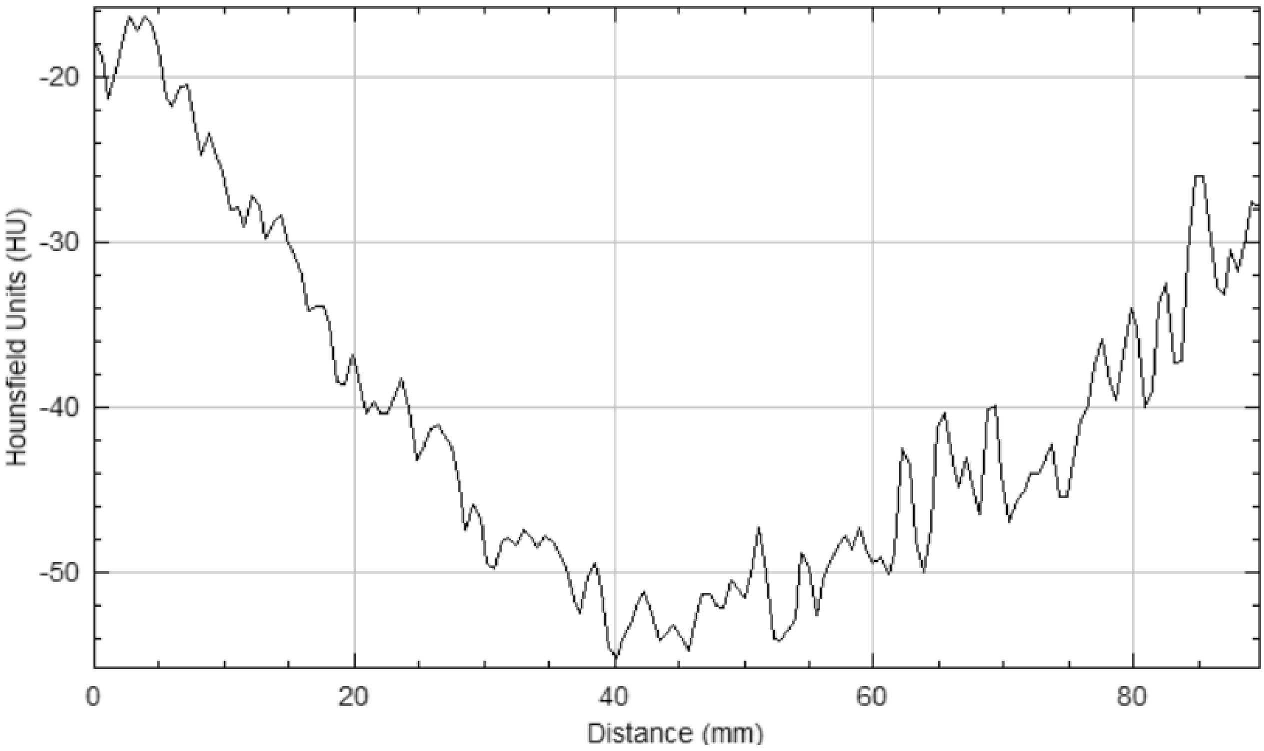

(a)

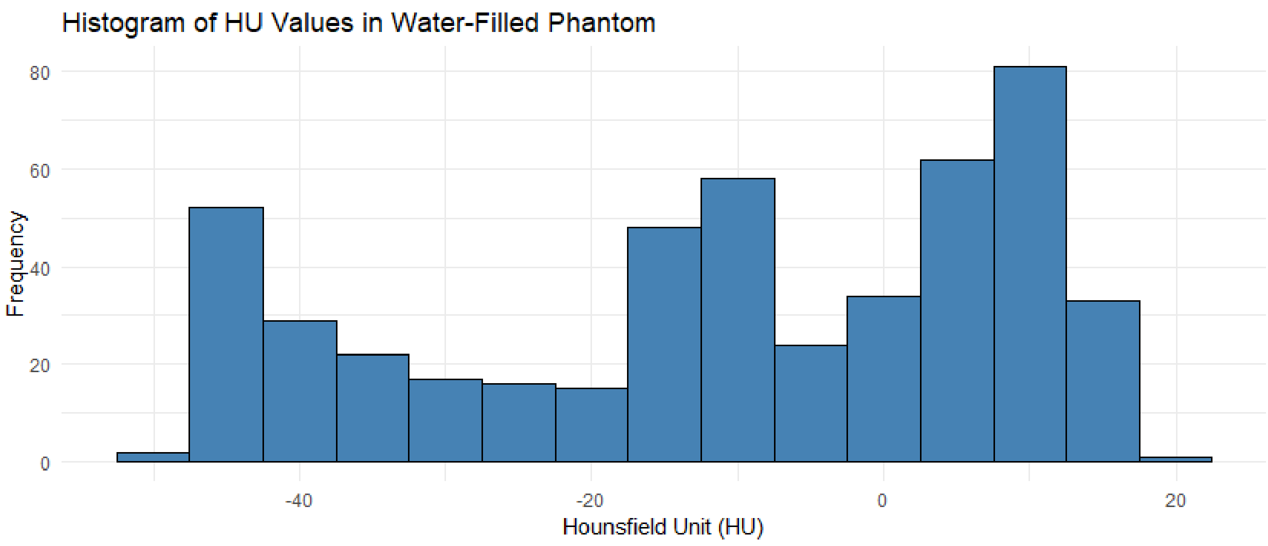

(b)

Fig. 35 Evaluation of internal radiological behavior of the HIPS-gelatin proof-of-concept phantom (a) ROI profile showing the mean attenuation characteristics of the phantom (b) histogram of HU values within the internal volume.

3.4.3. Evaluation of a multimaterial Head CT phantom

Fig. 30 (right) and **Fig. 33** (right) show the head CT phantom filled with water and gelatin respectively. In both cases the outer shell was 3D printed with HIPS and appears consistent with clearly defined edges and no visible warping or deformation. Both multimaterial arrangements display uniform internal structure with no intensity gradients, boundary or edge effects, or visible air bubbles. There is no visible separation between the shell and infill material and therefore the interface displays smoothly. Despite minor differences, both fillers show homogeneity upon visual inspection and absence of major artifacts. To quantitatively assess the internal radiological consistency of the multimaterial head phantom the line profile of both arrangements was performed. The attenuation profiles depicted in **Fig. 36** provides a detailed comparison of the internal uniformity of both samples.

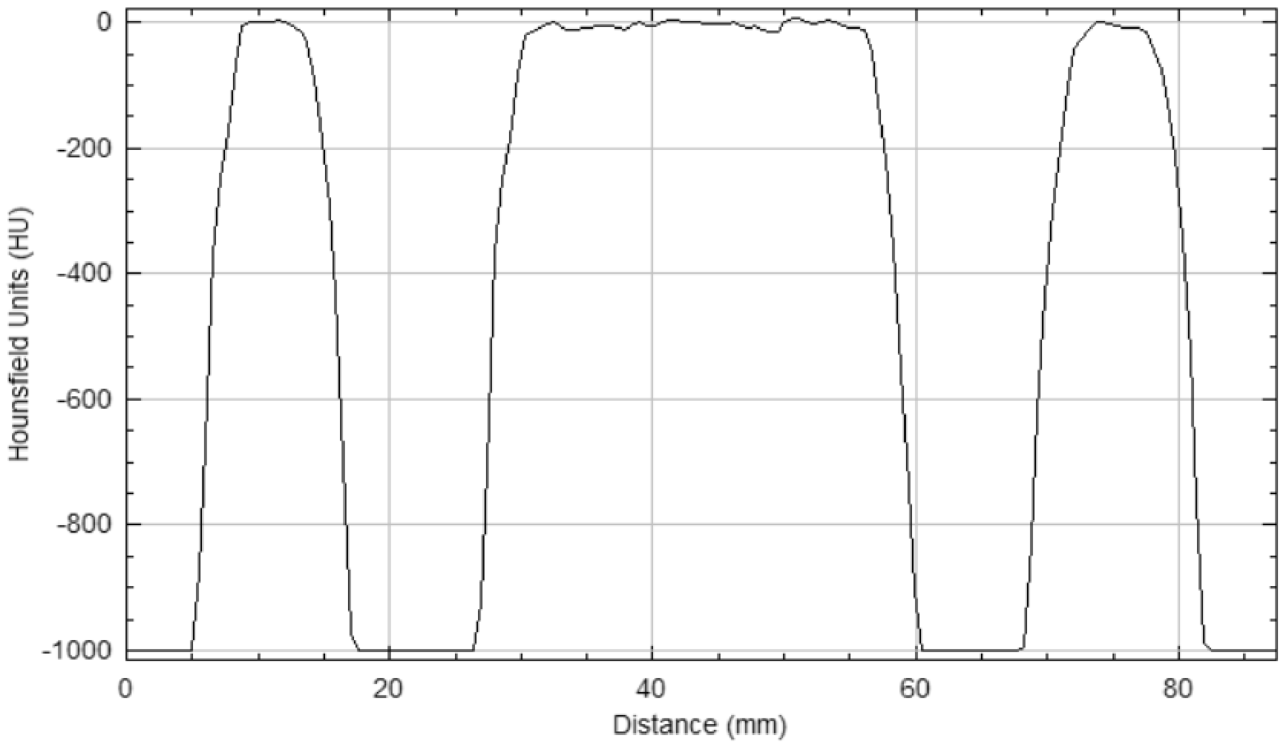

(a)

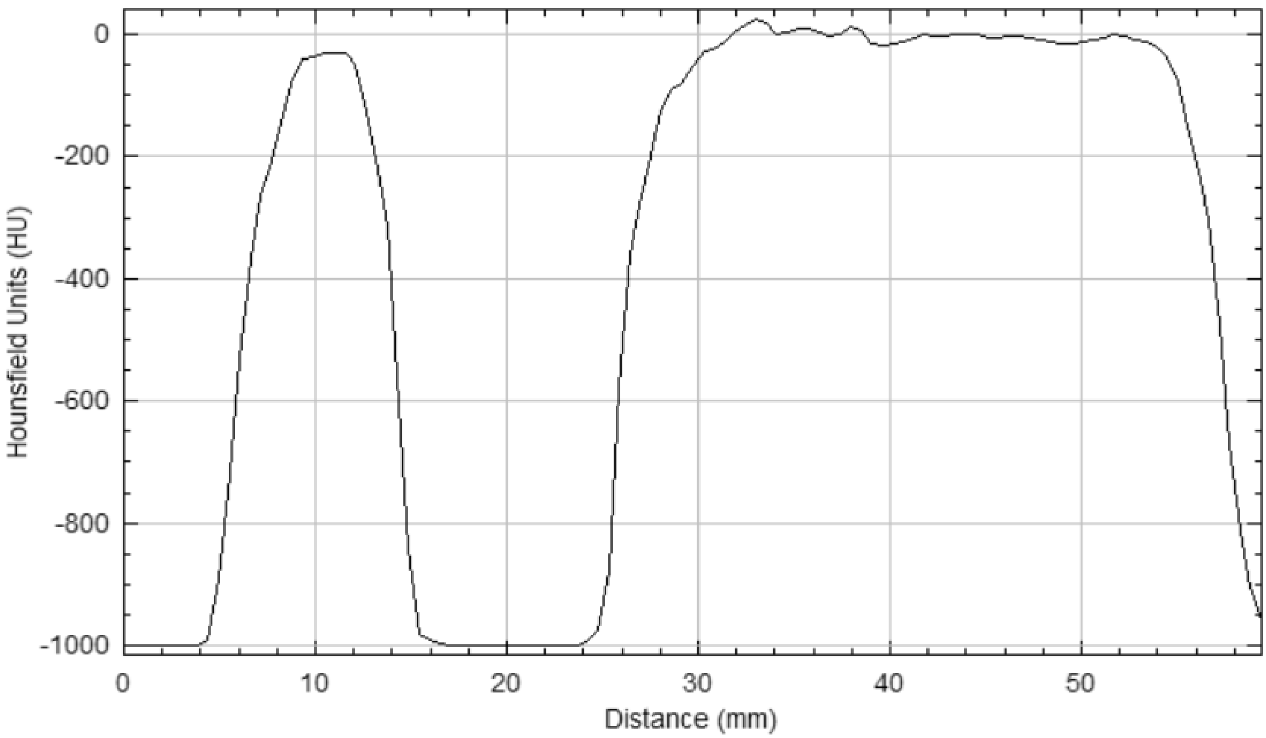

(b)

Fig. 36 Line attenuation profile analysis of the head CT phantoms filled with (a) water and (b) gelatin

The water-filled phantom shows a central plateau around +0 HU consistent with the expected attenuation values for water. The transition from air to HIPS and to water is well defined, there are no visible spikes or abnormalities showing good agreement with the expected behavior. On the other hand, the gelatin-filled phantom shows a similar profile shape, the second plateau values show slightly higher values than water and exhibits general consistency with no sharp dips or edge artifacts. Furthermore, both materials successfully mimic soft tissue radiological behavior, and the displayed homogeneity supports their applicability in clinical testing.

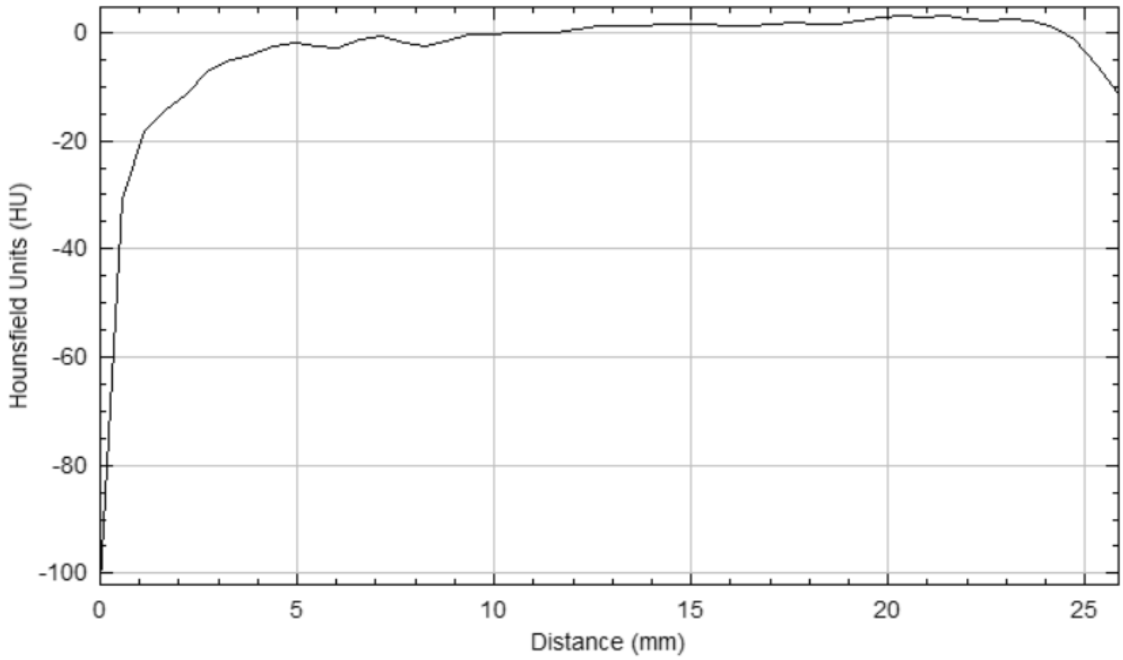

(b)

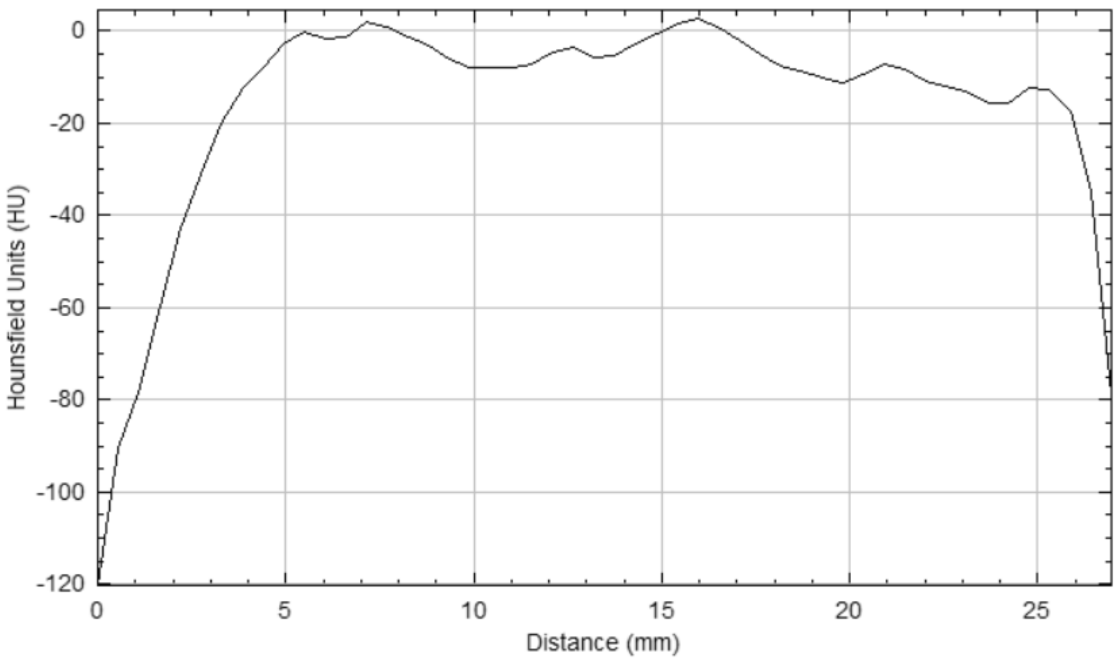

(b)

Fig. 37 Mean attenuation profile across a rectangular ROI within the head CT phantom filled with (a) water and (b) gelatin

The profile graphs of **Fig. 37** show the attenuation behavior of an ROI within the filler area of the head CT phantom. In the water phantom the HU values quickly stabilized around 0 HU after going through the outer shell where it reaches values around -120 HU. In the gelatin infill phantom, the same behavior is repeated but the CT numbers show greater oscillation than water but still insignificant. The values in gelatin range from -20 HU to -40 HU across the central region. The general structure is homogeneous in both cases with no spikes or valleys. The edge gradients at the beginning and end of the profiles can be attributed to the natural radiological properties of HIPS which can reach HU values of up to -130 HU. However, its presence does not impact the central uniformity.

Both phantoms' configurations demonstrate good internal consistency and attenuation characteristics suitable for phantom construction. While water exhibits greater uniformity, gelatin is easier to handle and good tissue-mimicking properties making it an excellent candidate for phantom construction.

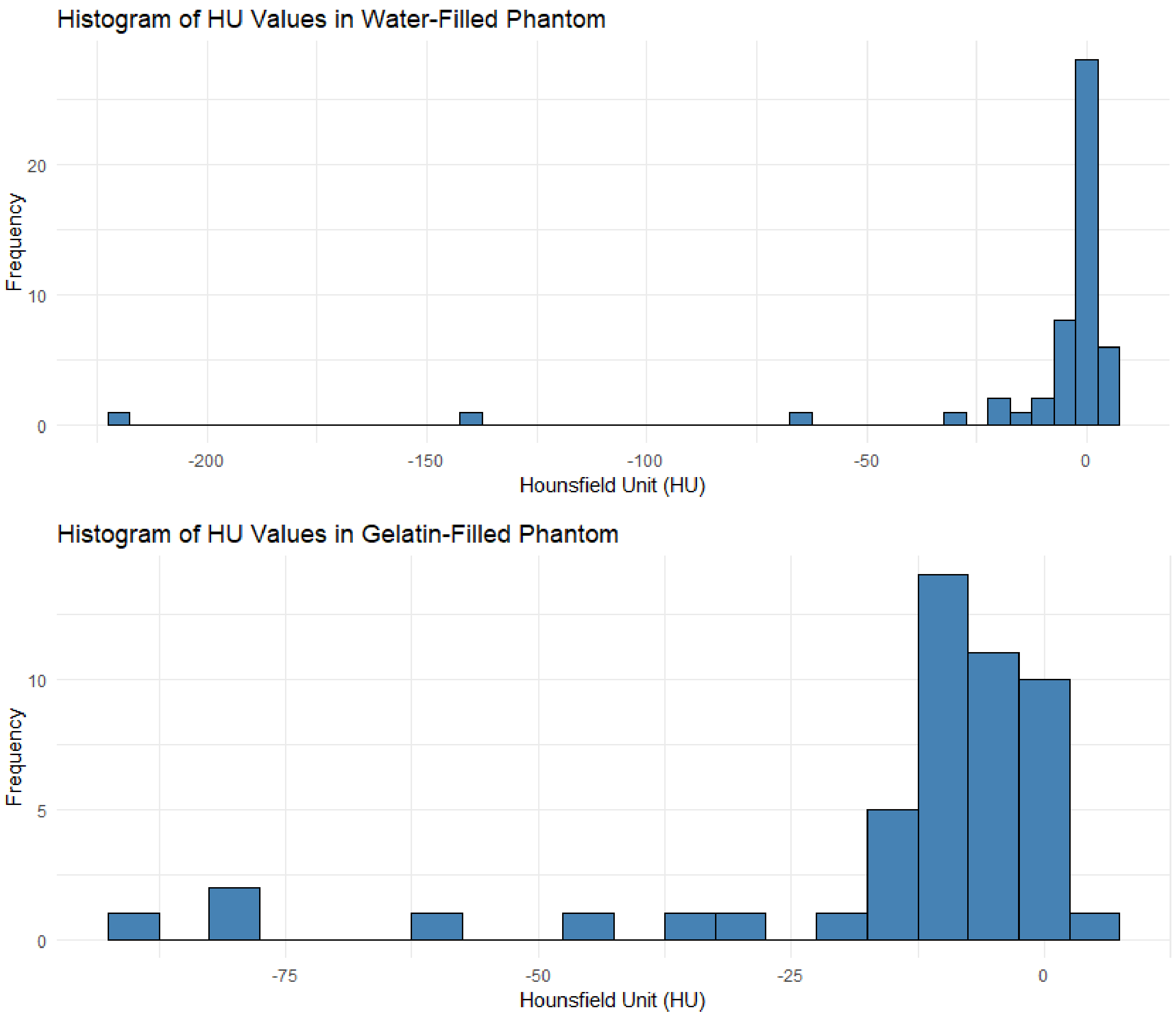

Fig. 38 Histogram of HU values within the internal volume for both multimaterial head Ct phantom configurations

The internal distribution of HU values within each phantom is shown as histograms to provide a statistical overview of their behavior (**Fig. 38**). The water phantom exhibits a concentrated distribution around 0 HU as expected. It displays a single sharp and narrow peak and the majority of the values range between -10 HU and +10 HU suggesting good degree of internal homogeneity and making water reliable for phantom evaluations. The few outliners present could be attributed to minor air gaps, but they do not produce a significant effect on the overall characterization.

In contrast, the gelatin phantom’s histogram reveals a broader distribution with data ranging from around -80 HU to +10 HU with a noticeable left skew. While this pattern implies greater internal variability than water, the central tendency still falls within soft tissue mimicking materials with a lower homogeneity than the water configuration. These results support the superiority of water in terms of radiological consistency but also point out gelatin as a potential substitute that offers more versatility and is easier to handle than liquid water. Further optimization of gelatin preparation could be studied to improve uniformity for broader applications of this technique.

3.4.4. HIPS-gelatin dose evaluation

The multimaterial phantom assembly of section 2.5.3 was as well scanned after placement of the radiochromic films. In **Fig. 39** it is clearly visible the symmetrically positioned radiochromic films following the original design of a CT QA phantom. No overlapping is observed. These films were analyzed after irradiation with a 2 Gy dose to evaluate the homogeneity of the dose imparted.

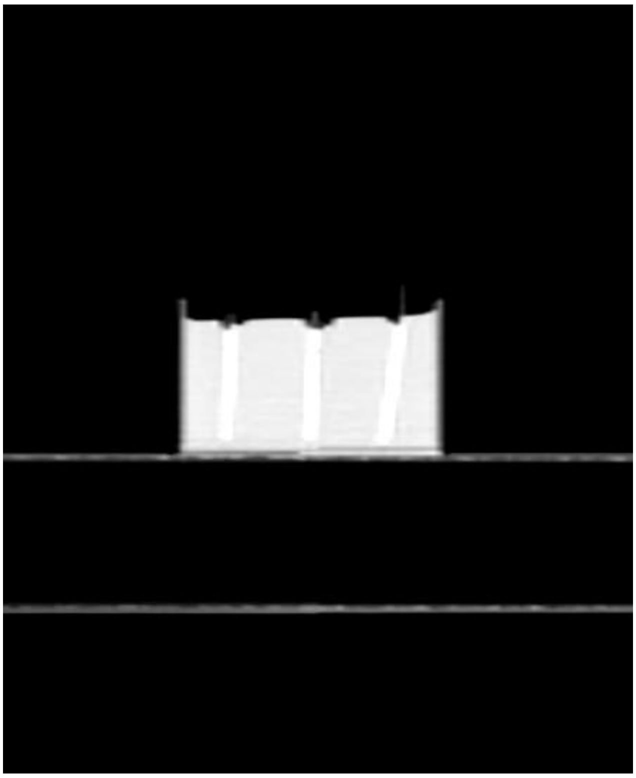

Fig. 39 CT scan of cylindrical phantom showing the radiochromic films positioning

To assess the homogeneity of the dose distribution in the radiochromic films two ROIs were analyzed in each film placed inside the phantom during the 2 Gy irradiation. The mean gray value, standard deviation and median of ROI were recorded and summarized in **Table 9**. The intra film analysis shows moderate consistency within each film. For example, F3 shows nearly identical means of 34.67 and 34.92 and comparable standard deviation suggestive a relatively homogeneous dose distribution. However, when comparing the films between them we find greater differences. F2 and F5 show significant differences. F2 ranges from 32.78 to 39.58 in mean gray value, and F5 from 32.31 to 38.21. This finds indicate possible inhomogeneities or inconsistencies.

Table 9. Homogeneity analysis of irradiated films in HIPS-gelatin phantom

Film	ROI	Mean Gray Value	Standard Deviation	Median
F1	1	32.382	2.025	32
	2	37.852	3.162	38
F2	1	32.781	1.922	33
	2	39.580	4.033	38
F3	1	34.673	2.989	34
	2	34.920	2.511	35
F4	1	39.724	2.189	40
	2	34.066	2.254	34
F5	1	38.207	3.221	39
	2	32.314	1.951	32

Mean gray values across films range from 32.31 to 39.72 with standard deviations between 1.92 and 4.03. These differences suggest some level of variation in the dose absorbed among the five positions. While these variations do not indicate extreme non-uniformity, they do suggest that uniformity is not ideal. Nonetheless, the overall dispersion is relatively contained and the results support basic feasibility of the HIFIPS-gelatin approach, but also leave room for refinement.

Conclusions

1. 3D printing with PMMA using FDM technology is feasible for fabricating samples with radiologically relevant properties at small-scale. The printed samples exhibited HU values comparable to those of commercial PMMA slabs, and it is suggested that post-processing can help achieve values that more closely relate to those of the printed sample’s commercial counterpart. However, the printing process remains technically challenging at 100% infill and larger vertical dimensions. Adhesion issues and layer separation represent a severe limitation in the achievable printed dimensions. This establishes clear boundaries for what is achievable with the current setup and suggests that equipment modification or alternative printing technologies should be explored as they may be required for future designs. Heated chambers or industrial-grade printers may also be of significant help with more complex phantom geometries. These findings open the door to broader medical and scientific applications.
2. The printing protocol developed for FDM printing of PMMA at 100% infill enabled the production of radiologically evaluable test samples slabs but also revealed key limitations specifically regarding adhesion loss, layer separation, and thermal instability which restrict the maximum achievable printing height in the Z-axis. These constraints highlight the need for controlled printing environments and possible hardware modifications and improvements such as considering the use of a heated chamber or enclosed industrial grade printers to achieve more complex geometries. Nevertheless, the protocol provides a functional foundation for future developments and research in efforts involving PMMA based 3D printing. The protocol was successfully developed and provided samples of up to 3 cm height despite the constraints and the samples achieved relevant radiological attenuation properties.
3. The use of homogeneous multimaterial phantoms with homogeneous infills was analyzed through a 3D printed HIPS shell phantom with two different infills and proved to be a viable approach for constructing composite phantoms for imaging applications. Qualitative and quantitative assessment of the HIPS-water and HIPS-gelatin arrangement revealed that both settings produce tissue equivalent attenuation. Water demonstrated an exceptional homogeneity while gelatin showed no significant internal irregularities confirming their applicability in quality assurance procedures. Additionally, dose response analysis using radiochromic film placed inside a gelatin-filled cylindrical phantom confirmed spatially consistent dose deposition across multiple internal regions. These findings support the integration of multimaterial homogeneous fillers 3D printed phantom designs as an alternative to fully printed models and also suggest that refinement and improvement could be achieved.

Recommendations

The study supports additive manufacturing as a method to develop customizable, cost-effective phantoms for medical imaging and medical applications but also highlights technical limitations. Based on this the following recommendations are proposed for future developments and applications of 3D printed technologies in medical physics:

1. Further efforts should be made to explore printing temperature-controlled environments. Semi-open frame printers such as the Zortrax M300 are not ideal for printing PMMA at 100% infill at large heights due to temperature gradient. Considerations should be made towards utilizing industrial grade enclosed printers to improve stability. Post processing techniques such as thermal or chemical treatments should also be considered to improve the achievable attenuation profile of the samples.
2. Continuing developing composite phantoms that combine printed technologies across a wide range of clinical applications. While PMMA offers relevant radiological properties, it also shows significant printing challenges. Other materials can be explored as a more practical alternative. Multimaterial phantoms designs should continue to be explored specially when complex geometries are needed as they offer high customization and broad characteristics.
3. Finally, it is strongly recommended in materials evaluation regarding radiological properties that measurements are conducted within a material medium such as water rather than air, to avoid CT reconstruction artifacts that may arise in the air-material boundaries and lead to misleading interpretation of the attenuation profile of the samples.

List of references

1. ZUBER, Siti Hajar; YUSOF, Mohd Fahmi Mohd; HASHIKIN, Nurul Ab Aziz; SAMSON, Damilola Oluwafemi; AZIZ, Mohd Zahri Abdul, et al. Rhizophora spp. as potential phantom material in medical physics applications – A review. *Radiation Physics and Chemistry*, vol. 189 (2021), pp. 109731. Available from: https://www.sciencedirect.com/science/article/pii/S0969806X21003819. [viewed May 11, 2025].

2. ARIB, Mehenna; MEDJADJ, Toufik and BOUDOUMA, Youcef. Study of the influence of phantom material and size on the calibration of ionization chambers in terms of absorbed dose to water. *Journal of Applied Clinical Medical Physics*, vol. 7 (2006), no. 3, pp. 55–64.

3. SAMSON, D. O.; JAFRI, MZ Mat; SHUKRI, A.; HASHIM, R.; SULAIMAN, O., et al. Measurement of radiation attenuation parameters of modified defatted soy flour–soy protein isolate-based mangrove wood particleboards to be used for CT phantom production. *Radiation and environmental biophysics*, vol. 59 (2020), no. 3, pp. 483–501.

4. HALEEM, Abid; JAVAID, Mohd; SUMAN, Rajiv and SINGH, Ravi Pratap. 3D Printing Applications for Radiology: An Overview. *The Indian Journal of Radiology & Imaging*, vol. 31 (2021), no. 1, pp. 10–17. Available from: https://www.ncbi.nlm.nih.gov/pmc/articles/PMC8299499/. [viewed May 12, 2025].

5. ACHILLAS, Charisios; TZETZIS, Dimitrios and AND RAIMONDO, Maria Olga. Alternative production strategies based on the comparison of additive and traditional manufacturing technologies. *International Journal of Production Research*, vol. 55 (2017), no. 12, pp. 3497–3509. Available from: https://doi.org/10.1080/00207543.2017.1282645. [viewed May 12, 2025].

6. MA, C-M; JIANG, S. B.; PAWLICKI, T.; CHEN, Y.; LI, J. S., et al. A quality assurance phantom for IMRT dose verification. *Physics in medicine & biology*, vol. 48 (2003), no. 5, pp. 561–572. Available from: http://iopscience.iop.org/0031-9155/48/5/301..

7. IAEA. *Absorbed Dose Determination in External Beam Radiotherapy*. International Atomic Energy Agency, 2024. Available from: https://www.perlego.com/book/4462044/absorbed-dose-determination-in-external-beam-radiotherapy-an-international-code-of-practice-for-dosimetry-based-on-standards-of-absorbed-dose-to-water-pdf..

8. RAJU, T. N. The Nobel chronicles. 1979: Allan MacLeod Cormack (b 1924); and Sir Godfrey Newbold Hounsfield (b 1919). *Lancet (London, England)*, vol. 354 (1999), no. 9190, pp. 1653. Available from: https://pubmed.ncbi.nlm.nih.gov/10560712/. [viewed May 11, 2025].

9. ALSOUFI, Mohammad S. and ELSAYED, Abdulrhman E. Surface Roughness Quality and Dimensional Accuracy—A Comprehensive Analysis of 100% Infill Printed Parts Fabricated by a Personal/Desktop Cost-Effective FDM 3D Printer. *Materials Sciences and Applications*, vol. 09 (2018), no. 01, pp. 11. Available from: http://www.scirp.org/journal/PaperInformation.aspx?PaperID=81581&#abstract. [viewed May 12, 2025].

10. DEWERD, Larry and KISSICK, Michael. *The Phantoms of Medical and Health Physics : Devices for Research and Development.* 1st ed. New York, NY: Springer New York, 2013. Available from: https://library.biblioboard.com/viewer/2aa6edca-bbad-11ea-92f3-0a28bb48d135..

11. *What is Radiotherapy?* [2023Oct 4]. Available from: https://www.cancerresearchuk.org/about-cancer/treatment/radiotherapy/what-is-radiotherapy. [viewed 4/12/2025].

12. KLEIN, Jeffrey; POHL, Jennifer; VINSON, Emily N.; BRANT, William E. and HELMS, Clyde A. *Brant and Helms' Fundamentals of Diagnostic Radiology*. 5th ed. Philadelphia: Wolters Kluwer,

2018. Available from: https://ebookcentral.proquest.com/lib/[SITE_ID]/detail.action?docID=6023363..
13. LIU, Haikuan; GU, Jianwei; CARACAPPA, Peter F. and XU, X. George. Comparison of two types of adult phantoms in terms of organ doses from diagnostic CT procedures. *Physics in Medicine and Biology*, vol. 55 (2010), no. 5, pp. 1441–1451. Available from: http://iopscience.iop.org/0031-9155/55/5/012..
14. WEGNER, Marie; GARGIONI, Elisabetta and KRAUSE, Dieter. Classification of phantoms for medical imaging. *Procedia CIRP*, vol. 119 (2023), pp. 1140–1145. Available from: https://dx.doi.org/10.1016/j.procir.2023.03.154..
15. V.E. Kouloulias. Quality assurance in radiotherapy. *European Journal of Cancer* (2003), no. 39, pp. 415–422.
16. JOHANSSON, K. A.; HORIOT, J. C.; VAN DAM, J.; LEPINOY, D.; SENTENAC, I., et al. Quality assurance control in the EORTC cooperative group of radiotherapy. 2. Dosimetric intercomparison. *Radiotherapy and oncology*, vol. 7 (1986), no. 3, pp. 269–279. Available from: https://www.ncbi.nlm.nih.gov/pubmed/3809589..
17. JOHANSSON, K. -A; HORIOT, J. C.; VAN DAM, J.; LEPINOY, D.; SENTENAC, I., et al. Quality assurance control in the EORTC cooperative group ofradiotherapy. *Radiotherapy and oncology*, vol. 7 (1986), no. 3, pp. 269–279. Available from: https://dx.doi.org/10.1016/S0167-8140(86)80038-X..
18. HORIOT, J. C. Response to Seelentag and Garavaglia: 'Minimum requirements for quality assurance in radiotherapy'. *Radiotherapy and oncology*, vol. 32 (1994), no. 2, pp. 185. Available from: https://dx.doi.org/10.1016/0167-8140(94)90107-4..
19. MCGARRY, Conor K.; GRATTAN, Lesley J.; IVORY, Aoife M.; LEEK, Francesca; LINEY, Gary P., et al. Tissue mimicking materials for imaging and therapy phantoms: a review. *Physics in medicine & biology*, vol. 65 (2020), no. 23. Available from: https://www.ncbi.nlm.nih.gov/pubmed/32998112..
20. KARGAR SHAKER LANGAROODI, Roghayeh ABTAHI, Seyed Mohammad Mahdi and AKBARI, Mohammad Esmaeil . Investigation of the radiological properties of various phantoms for their application in low energy X-rays dosimetry.
21. LENNIE, Eve; TSOUMPAS, Charalampos and SOURBRON, Steven. Multimodal phantoms for clinical PET/MRI. *EJNMMI Physics*, vol. 8 (2021), no. 1, pp. 62–62. Available from: https://link.springer.com/article/10.1186/s40658-021-00408-0..
22. VALLADARES, Alejandra; BEYER, Thomas and RAUSCH, Ivo. Physical imaging phantoms for simulation of tumor heterogeneity in PET, CT, and MRI: An overview of existing designs. *Medical Physics*, vol. 47 (2020), no. 4, pp. 2023–2037. Available from: https://onlinelibrary.wiley.com/doi/abs/10.1002%2Fmp.14045..
23. CAMERON, Matthew; CORNELIUS, Iwan; CUTAJAR, Dean; DAVIS, Jeremy; ROSENFELD, Anatoly, et al. Comparison of phantom materials for use in quality assurance of microbeam radiation therapy. *Journal of synchrotron radiation*, vol. 24 (2017), no. 4, pp. 866–876. Available from: https://onlinelibrary.wiley.com/doi/abs/10.1107%2FS1600577517005641..
24. AGENCY, International A. E. *Commissioning and Quality Assurance of Computerized Planning Systems for Radiation Treatment of Cancer. Technical Reports Series No. 430.* 1st ed. Lanham: International Atomic Energy Agency, 2004. Available from: https://ebookcentral.proquest.com/lib/[SITE_ID]/detail.action?docID=5266622..
25. ICRU. Tissue substitutes in radiation dosimetry and measurement(Report 44). *International Commission on Radiation Units and Measurements* (1989).

26. HILL, Robin; KUNCIC, Zdenka and BALDOCK, Clive. The water equivalence of solid phantoms for low energy photon beams. *Medical Physics*, vol. 37 (2010), no. 8, pp. 4355–4363. Available from: http://dx.doi.org/10.1118/1.3462558..
27. HILL, Robin; HEALY, Brendan; HOLLOWAY, Lois; KUNCIC, Zdenka; THWAITES, David, et al. Advances in kilovoltage x-ray beam dosimetry. *Physics in medicine & biology*, vol. 59 (2014), no. 6, pp. R183–R231. Available from: https://iopscience.iop.org/article/10.1088/0031-9155/59/6/R183..
28. *Magnetic Resonance Imaging (MRI).* Available from: https://www.nibib.nih.gov/science-education/science-topics/magnetic-resonance-imaging-mri. [viewed Apr 14, 2025].
29. HATTORI, Kengo; IKEMOTO, Yusuke; TAKAO, Wataru; OHNO, Seiichiro; HARIMOTO, Takashi, et al. Development of MRI phantom equivalent to human tissues for 3.0-T MRI. *Medical physics (Lancaster)*, vol. 40 (2013), no. 3, pp. 032303–n/a. Available from: http://dx.doi.org/10.1118/1.4790023..
30. BRAY, Freddie; FERLAY, Jacques; SOERJOMATARAM, Isabelle; SIEGEL, Rebecca L.; TORRE, Lindsey A., et al. Global cancer statistics 2018: GLOBOCAN estimates of incidence and mortality worldwide for 36 cancers in 185 countries. *CA: A Cancer Journal for Clinicians*, vol. 68 (2018), no. 6, pp. 394–424. Available from: https://onlinelibrary.wiley.com/doi/abs/10.3322%2Fcaac.21492..
31. SUNG, Hyuna; FERLAY, Jacques; SIEGEL, Rebecca L.; LAVERSANNE, Mathieu; SOERJOMATARAM, Isabelle, et al. Global Cancer Statistics 2020: GLOBOCAN Estimates of Incidence and Mortality Worldwide for 36 Cancers in 185 Countries. *CA: A Cancer Journal for Clinicians*, vol. 71 (2021), no. 3, pp. 209–249. Available from: https://onlinelibrary.wiley.com/doi/abs/10.3322%2Fcaac.21660.
32. European Commission. European Guidelines on Quality Criteria for Computed Tomography. European Communities. *Report EUR*, vol. 16262 (1999).
33. JUDY P. F. Phantoms for performance evaluation and quality assurance of CT scanners. *AAPM Report*, vol. 1 (1977), pp. 1–2.
34. American College of Radiology. *Computed Tomography: Quality Control Manual.* Reston, VA: American College of Radiology, 2017.
35. International Atomic Energy Agency. *Quality assurance programme for computed tomography : diagnostic and therapy applications.* International Atomic Energy Agency, 2012.
36. JOHNSTON, Ashley; MAHESH, Mahadevappa; UNERI, Ali; RYPINSKI, Tatiana A.; BOONE, John M., et al. Objective image quality assurance in cone-beam CT: Test methods, analysis, and workflow in longitudinal studies. *Medical physics (Lancaster)*, vol. 51 (2024), no. 4, pp. 2424–2443. Available from: https://onlinelibrary.wiley.com/doi/abs/10.1002%2Fmp.16983..
37. SAMEI, Ehsan; BAKALYAR, Donovan; BOEDEKER, Kirsten L.; BRADY, Samuel; FAN, Jiahua, et al. Performance evaluation of computed tomography systems: summary of AAPM Task Group 233. *Medical physics*, vol. 46 (2019), no. 11, pp. e735–e756.
38. BISSONNETTE, Jean-Pierre; BALTER, Peter A.; DONG, Lei; LANGEN, Katja M.; LOVELOCK, D. Michael, et al. Quality assurance for image-guided radiation therapy utilizing CT-based technologies: a report of the AAPM TG-179. *Medical physics*, vol. 39 (2012), no. 4, pp. 1946–1963.
39. SUPANICH, Mark; SIEWERDSEN, Jeff; FAHRIG, Rebecca; FARAHANI, Keyvan; GANG, Grace Jianan, et al. AAPM Task Group Report 238: 3D C-arms with volumetric imaging capability. *Medical physics*, vol. 50 (2023), no. 8, pp. e904–e945.

40. GALA, H.; TORRESIN, A.; DASU, A.; RAMPADO, O.; DELIS, H., et al. Quality control in cone-beam computed tomography (CBCT). EFOMP-ESTRO-IAEA protocol (2017).
41. BAMBA, J.; ARAKI, K.; ENDO, A. and OKANO, T. Image quality assessment of three cone beam CT machines using the SEDENTEXCT CT phantom. *Dentomaxillofacial Radiology*, vol. 42 (2013), no. 8, pp. 20120445.
42. JAFFRAY, David A.; SIEWERDSEN, Jeffrey H.; WONG, John W. and MARTINEZ, Alvaro A. Flat-panel cone-beam computed tomography for image-guided radiation therapy. *International Journal of Radiation Oncology* Biology* Physics*, vol. 53 (2002), no. 5, pp. 1337–1349.
43. Jeffrey H. SIEWERDSEN; Y. Chan; M. A. Rafferty; D. J. Moseley; David A. Jaffray, et al. Cone-Beam CT with a Flat-Panel Detector on a Mobile C-Arm: Preclinical Investigation in Image-Guided Surgery of the Head and Neck*In: Medical Imaging 2005: Visualization, Image-Guided Procedures, and Display*, pp. 789–797.SPIE, 2005.
44. FAHRIG, Rebecca; GANGULY, Arundhuti; STARMAN, Jared D. and STROBEL, Norbert K. C-arm CT with XRIIs and digital flat panels: a review. *Developments in X-Ray Tomography IV*, vol. 5535 (2004), pp. 400–409.
45. BOONE, John M.; NELSON, Thomas R.; LINDFORS, Karen K. and SEIBERT, J. Anthony. Dedicated breast CT: radiation dose and image quality evaluation. *Radiology*, vol. 221 (2001), no. 3, pp. 657–667.
46. CARRINO, John A.; AL MUHIT, Abdullah; ZBIJEWSKI, Wojciech; THAWAIT, Gaurav K.; STAYMAN, J. Webster, et al. Dedicated cone-beam CT system for extremity imaging. *Radiology*, vol. 270 (2014), no. 3, pp. 816–824.
47. DE OLIVEIRA, Marcus VL; WENZEL, Ann; CAMPOS, Paulo SF and SPIN-NETO, Rubens. Quality assurance phantoms for cone beam computed tomography: a systematic literature review. *Dentomaxillofacial Radiology*, vol. 46 (2017), no. 3, pp. 20160329.
48. WATANABE, Hiroshi; HONDA, Eiichi; TETSUMURA, Akemi and KURABAYASHI, Tohru. A comparative study for spatial resolution and subjective image characteristics of a multi-slice CT and a cone-beam CT for dental use. *European Journal of Radiology*, vol. 77 (2011), no. 3, pp. 397–402.
49. FRIEDMAN, Saul N.; FUNG, George SK; SIEWERDSEN, Jeffrey H. and TSUI, Benjamin MW. A simple approach to measure computed tomography (CT) modulation transfer function (MTF) and noise-power spectrum (NPS) using the American College of Radiology (ACR) accreditation phantom. *Medical physics*, vol. 40 (2013), no. 5, pp. 051907.
50. SIEWERDSEN, J. H.; UNERI, A.; HERNANDEZ, A. M.; BURKETT, G. W. and BOONE, J. M. Cone-beam CT dose and imaging performance evaluation with a modular, multipurpose phantom. *Medical physics*, vol. 47 (2020), no. 2, pp. 467–479.
51. *Lithuanian Hygiene Standard Hn 78: 2009 "Quality Control Requirements and Evaluation Criteria in Medical X-Ray Diagnostics"*. Vilnius: Official Gazette 2009, No. 137-6025, Oct 19, 2025. Available from: https://e-seimas.lrs.lt/portal/legalAct/lt/TAD/TAIS.358448/WGKWTFGsHA. [viewed May 8, 2025].
52. International Society of Radiographers and Radiological Technologists (ISRRT). *ISRRT Guidance Document on QA/QC in CT*. , July, 2019. Available from: https://www.isrrt.org/wp-content/uploads/2023/07/UPDATED2-QAQC-IN-CT-ISRRT-FLOW-CHART-AND-CT-QC-TEST-GUIDANCE-CHART.pdf..
53. KHALLOUQI, A.; HALIMI, A. and EL RHAZOUANI, O. Comparative dosimetry of an epoxy resin pediatric head phantom and PMMA phantom for CT imaging. *Radiation Physics and Chemistry*,

vol. 216 (2024), pp. 111350. Available from: https://www.sciencedirect.com/science/article/pii/S0969806X23005960. [viewed Apr 12, 2025].
54. ESPINOSA, María del Mar; DOMÍNGUEZ, Iris A.; ROMERO, L.; JIMÉNEZ, Mariano and DOMÍNGUEZ, Manuel. Additive Manufacturing Technologies: An Overview about 3D Printing Methods and Future Prospects. *Complexity*, vol. 2019 (2019), no. 2019, pp. 1–30. Available from: https://search.emarefa.net/detail/BIM-1133324..
55. CONNER, Brett P.; MANOGHARAN, Guha P.; MARTOF, Ashley N.; RODOMSKY, Lauren M.; RODOMSKY, Caitlyn M., et al. Making sense of 3-D printing: Creating a map of additive manufacturing products and services. *Additive Manufacturing*, vol. 1-4 (2014), pp. 64–76. Available from: https://dx.doi.org/10.1016/j.addma.2014.08.005..
56. ATTARAN, Mohsen. The rise of 3-D printing: The advantages of additive manufacturing over traditional manufacturing. *Business Horizons*, vol. 60 (2017), no. 5, pp. 677–688. Available from: https://dx.doi.org/10.1016/j.bushor.2017.05.011..
57. ALBRIGHT, Brian. *Wohlers Report 2025 shows 9.1% AM Industry Growth.* Thu, 03 Apr 2025 15:22:00 -0400]. Available from: https://www.digitalengineering247.com/article/wohlers-report-2025-shows-9.1-am-industry-growth. [viewed Apr 26, 2025].
58. WONG, Kaufui V. and HERNANDEZ, Aldo. A review of additive manufacturing. *International scholarly research notices*, vol. 2012 (2012), no. 1, pp. 208760.
59. KAFLE, Abishek; LUIS, Eric; SILWAL, Raman; PAN, Houwen Matthew; SHRESTHA, Pratisthit Lal, et al. 3D/4D Printing of Polymers: Fused Deposition Modelling (FDM), Selective Laser Sintering (SLS), and Stereolithography (SLA). *Polymers*, vol. 13 (2021), no. 18, pp. 3101. Available from: https://www.mdpi.com/2073-4360/13/18/3101. [viewed May 2, 2025].
60. KARAKURT, Ilbey and LIN, Liwei. 3D printing technologies: techniques, materials, and post-processing. *Current opinion in chemical engineering*, vol. 28 (2020), pp. 134–143. Available from: https://dx.doi.org/10.1016/j.coche.2020.04.001..
61. *What is SLA Printing? the Original Resin 3D Print Method.* Available from: https://www.hubs.com/knowledge-base/what-is-sla-3d-printing/. [viewed Apr 26, 2025].
62. MELCHELS, Ferry P. W.; FEIJEN, Jan and GRIJPMA, Dirk W. A review on stereolithography and its applications in biomedical engineering. *Biomaterials*, vol. 31 (2010), no. 24, pp. 6121–6130. Available from: https://www.clinicalkey.es/playcontent/1-s2.0-S0142961210005661..
63. BAGHERI, Ali and JIN, Jianyong. Photopolymerization in 3D Printing. *ACS applied polymer materials*, vol. 1 (2019), no. 4, pp. 593–611. Available from: http://dx.doi.org/10.1021/acsapm.8b00165..
64. MONDSCHEIN, Ryan J.; KANITKAR, Akanksha; WILLIAMS, Christopher B.; VERBRIDGE, Scott S. and LONG, Timothy E. Polymer structure-property requirements for stereolithographic 3D printing of soft tissue engineering scaffolds. *Biomaterials*, vol. 140 (2017), pp. 170–188. Available from: https://www.clinicalkey.es/playcontent/1-s2.0-S014296121730399X..
65. HON, K. K. B.; LI, L. and HUTCHINGS, I. M. Direct writing technology—Advances and developments. *CIRP Annals*, vol. 57 (2008), no. 2, pp. 601–620. Available from: https://dx.doi.org/10.1016/j.cirp.2008.09.006..
66. *What is FDM (Fused Deposition Modeling) 3D Printing?* . Available from: https://www.hubs.com/knowledge-base/what-is-fdm-3d-printing/. [viewed Apr 26, 2025].
67. ALIHEIDARI, Nahal; CHRIST, Josef; TRIPURANENI, Rajasekhar; NADIMPALLI, Siva and AMELI, Amir. Interlayer adhesion and fracture resistance of polymers printed through melt extrusion additive manufacturing process. *Materials & Design*, vol. 156 (2018), pp. 351–361. Available from: https://dx.doi.org/10.1016/j.matdes.2018.07.001..

68. SUKINDAR, Nor Aiman; ARIFFIN, M. K. A.; BAHARUDIN, B. T. Hang Tuah; JAAFAR, Che Nor Aiza and ISMAIL, Mohd Idris Shah. ANALYZING THE EFFECT OF NOZZLE DIAMETER IN FUSED DEPOSITION MODELING FOR EXTRUDING POLYLACTIC ACID USING OPEN SOURCE 3D PRINTING. *Jurnal teknologi. A, Pembuatan, bahan termaju, tenaga dan pengangkutan*, vol. 78 (2016), no. 10. Available from: http://psasir.upm.edu.my/id/eprint/55059/1/Analyzing%20the%20effect%20of%20nozzle%20diameter%20in%20fused%20deposition%20modeling%20for%20extruding%20.pdf..
69. FERRETTI, Patrich; LEON-CARDENAS, Christian; SANTI, Gian Maria; SALI, Merve; CIOTTI, Elisa, et al. Relationship between FDM 3D Printing Parameters Study: Parameter Optimization for Lower Defects. *Polymers*, vol. 13 (2021), no. 13, pp. 2190. Available from: https://www.mdpi.com/2073-4360/13/13/2190. [viewed May 2, 2025].
70. FDM_Technologies. Available from: https://3dprintwestern.com/wp-content/uploads/2018/11/FDM_Technologies.jpeg. [viewed Apr 26, 2025].
71. *Sla 3d Printing.* [2017-03-06]. Available from: https://3dcolors.fr/sla-3d-printing/. [viewed Apr 26, 2025].
72. Overview of Electron Beam Melting Technology - MET3DP. -10-16, 2023. Available from: https://met3dp.com/overview-of-electron-beam-melting-technology/. [viewed Apr 27, 2025].
73. BIAMINO, S.; PENNA, A.; ACKELID, U.; SABBADINI, S.; TASSA, O., et al. Electron beam melting of Ti–48Al–2Cr–2Nb alloy: Microstructure and mechanical properties investigation. *Intermetallics*, vol. 19 (2011), no. 6, pp. 776–781. Available from: https://dx.doi.org/10.1016/j.intermet.2010.11.017..
74. GAYTAN, S. M.; MURR, L. E.; MEDINA, F.; MARTINEZ, E.; LOPEZ, M. I., et al. Advanced metal powder based manufacturing of complex components by electron beam melting. *Materials Technology*, vol. 24 (2009), no. 3, pp. 180–190. Available from: https://www.tandfonline.com/doi/abs/10.1179/106678509X12475882446133..
75. GALATI, Manuela. Chapter 8 - Electron beam melting process: a general overview*In: Additive Manufacturing*, pp. 277–301POU, Juan; RIVEIRO, Antonio and DAVIM, J. Paulo. Elsevier, 2021. Available from: https://www.sciencedirect.com/science/article/pii/B9780128184110000148. [viewed Apr 27, 2025].
76. LEDFORD, Christopher; ROCK, Christopher; CARRIERE, Paul; FRIGOLA, Pedro; GAMZINA, Diana, et al. Characteristics and Processing of Hydrogen-Treated Copper Powders for EB-PBF Additive Manufacturing. *Applied sciences*, vol. 9 (2019), no. 19, pp. 3993. Available from: https://www.proquest.com/docview/2533660884..
77. FOX, Jason C.; MOYLAN, Shawn P. and LANE, Brandon M. Effect of Process Parameters on the Surface Roughness of Overhanging Structures in Laser Powder Bed Fusion Additive Manufacturing. *Procedia CIRP*, vol. 45 (2016), pp. 131–134. Available from: https://dx.doi.org/10.1016/j.procir.2016.02.347..
78. MURR, Lawrence E.; MARTINEZ, Edwin; AMATO, Krista N.; GAYTAN, Sara M.; HERNANDEZ, Jennifer, et al. Fabrication of Metal and Alloy Components by Additive Manufacturing: Examples of 3D Materials Science. *Journal of Materials Research and Technology*, vol. 1 (2012), no. 1, pp. 42–54. Available from: https://dx.doi.org/10.1016/S2238-7854(12)70009-1..
79. KRUTH, J-P; MERCELIS, P.; VAN VAERENBERGH, J.; FROYEN, L. and ROMBOUTS, M. Binding mechanisms in selective laser sintering and selective laser melting. *Rapid Prototyping Journal*, vol. 11 (2005), no. 1, pp. 26–36. Available from: https://www.emerald.com/insight/content/doi/10.1108/13552540510573365/full/html..

80. WUDY, Katrin; LANZL, Lydia and DRUMMER, Dietmar. Selective Laser Sintering of Filled Polymer Systems: Bulk Properties and Laser Beam Material Interaction. *Physics procedia*, vol. 83 (2016), pp. 991–1002. Available from: https://dx.doi.org/10.1016/j.phpro.2016.08.104..
81. UÇAK, Necati; ÇIÇEK, Adem and ASLANTAS, Kubilay. Machinability of 3D printed metallic materials fabricated by selective laser melting and electron beam melting: A review. *Journal of Manufacturing Processes*, vol. 80 (2022), pp. 414–457. Available from: https://www.sciencedirect.com/science/article/pii/S152661252200408X. [viewed May 2, 2025].
82. MAZZANTI, Valentina; MALAGUTTI, Lorenzo and MOLLICA, Francesco. FDM 3D Printing of Polymers Containing Natural Fillers: A Review of their Mechanical Properties. *Polymers*, vol. 11 (2019), no. 7, pp. 1094. Available from: https://www.ncbi.nlm.nih.gov/pubmed/31261607..
83. PAGAC, Marek; HAJNYS, Jiri; MA, Quoc-Phu; JANCAR, Lukas; JANSA, Jan, et al. A review of vat photopolymerization technology: materials, applications, challenges, and future trends of 3D printing. *Polymers*, vol. 13 (2021), no. 4, pp. 598.
84. CHAROO, Naseem A.; BARAKH ALI, Sogra F.; MOHAMED, Eman M.; KUTTOLAMADOM, Mathew A.; OZKAN, Tanil, et al. Selective laser sintering 3D printing–an overview of the technology and pharmaceutical applications. *Drug development and industrial pharmacy*, vol. 46 (2020), no. 6, pp. 869–877.
85. SUSLICK, Kenneth S. Encyclopedia of physical science and technology. *Sonoluminescence and sonochemistry, 3rd edn.Elsevier Science Ltd, Massachusetts* (2001), pp. 1–20.
86. OSMANLIC, Fuad; WUDY, Katrin; LAUMER, Tobias; SCHMIDT, Michael; DRUMMER, Dietmar, et al. Modeling of laser beam absorption in a polymer powder bed. *Polymers*, vol. 10 (2018), no. 7, pp. 784.
87. LANTEAN, Simone; BARRERA, Gabriele; PIRRI, Candido Fabrizio; TIBERTO, Paola; SANGERMANO, Marco, et al. 3D printing of magnetoresponsive polymeric materials with tunable mechanical and magnetic properties by digital light processing. *Advanced Materials Technologies*, vol. 4 (2019), no. 11, pp. 1900505.
88. BUJ-CORRAL, Irene; DOMÍNGUEZ-FERNÁNDEZ, Alejandro and GÓMEZ-GEJO, Ana. Effect of Printing Parameters on Dimensional Error and Surface Roughness Obtained in Direct Ink Writing (DIW) Processes. *Materials*, vol. 13 (2020), no. 9, pp. 2157. Available from: https://www.mdpi.com/1996-1944/13/9/2157. [viewed May 2, 2025].
89. WANG, Xin; JIANG, Man; ZHOU, Zuowan; GOU, Jihua and HUI, David. 3D printing of polymer matrix composites: A review and prospective. *Composites Part B: Engineering*, vol. 110 (2017), pp. 442–458.
90. MUZAFFAR, Aqib; AHAMED, M. B.; DESHMUKH, Kalim; KOVÁŘÍK, Tomáš; KŘENEK, Tomáš, et al. 3D and 4D printing of pH-responsive and functional polymers and their composites*In: 3D and 4D printing of polymer nanocomposite materials*, pp. 85–117Elsevier, 2020.
91. MSALLEM, Bilal; SHARMA, Neha; CAO, Shuaishuai; HALBEISEN, Florian S.; ZEILHOFER, Hans-Florian, et al. Evaluation of the Dimensional Accuracy of 3D-Printed Anatomical Mandibular Models Using FFF, SLA, SLS, MJ, and BJ Printing Technology. *Journal of Clinical Medicine*, vol. 9 (2020), no. 3, pp. 817. Available from: https://www.ncbi.nlm.nih.gov/pubmed/32192099..
92. KIM, Dohyun; SHIM, Ji-Suk; LEE, Dasun; SHIN, Seung-Ho; NAM, Na-Eun, et al. Effects of post-curing time on the mechanical and color properties of three-dimensional printed crown and bridge materials. *Polymers*, vol. 12 (2020), no. 11, pp. 2762.
93. CHACÓN, J. M.; CAMINERO, M. A.; GARCÍA-PLAZA, E. and NÚÑEZ, P. J. Additive manufacturing of PLA structures using fused deposition modelling: Effect of process parameters on

mechanical properties and their optimal selection. *Materials & design*, vol. 124 (2017), pp. 143–157. Available from: https://dx.doi.org/10.1016/j.matdes.2017.03.065..
94. CHANTARAPANICH, Nattapon; PUTTAWIBUL, Puttisak; SITTHISERIPRATIP, Kriskrai; SUCHARITPWATSKUL, Sedthawatt and CHANTAWEROAD, Surapon. Study of the mechanical properties of photo-cured epoxy resin fabricated by stereolithography process. *Songklanakarin Journal of Science & Technology*, vol. 35 (2013), no. 1.
95. TOMANIK, Magdalena; ŻMUDZIŃSKA, Matylda and WOJTKÓW, Magdalena. Mechanical and structural evaluation of the PA12 desktop selective laser sintering printed parts regarding printing strategy. *3D printing and additive manufacturing*, vol. 8 (2021), no. 4, pp. 271–279.
96. SYRLYBAYEV, Daniyar; ZHARYLKASSYN, Beibit; SEISEKULOVA, Aidana; AKHMETOV, Mustakhim; PERVEEN, Asma, et al. Optimisation of Strength Properties of FDM Printed Parts—A Critical Review. *Polymers*, vol. 13 (2021), no. 10, pp. 1587. Available from: https://www.proquest.com/docview/2532758807..
97. TRIYONO, Joko; SUKANTO, Heru; SAPUTRA, Rizki Mica and SMARADHANA, Dharu Feby. The effect of nozzle hole diameter of 3D printing on porosity and tensile strength parts using polylactic acid material. *Open Engineering (Warsaw)*, vol. 10 (2020), no. 1, pp. 762–768. Available from: http://www.degruyter.com/doi/10.1515/eng-2020-0083..
98. Dongni GENG and Jichang Zhao. Analysis and Optimization of Warpage Deformation in 3D Printing Training Teaching--Taking Jilin University Engineering Training Center as an Example*In: 2018 International Workshop on Education Reform and Social Sciences (ERSS 2018)*, pp. 839–842.Atlantis Press, 2019.
99. UNKOVSKIY, Alexey; BUI, Phan Hai-Binh; SCHILLE, Christine; GEIS-GERSTORFER, Juergen; HUETTIG, Fabian, et al. Objects build orientation, positioning, and curing influence dimensional accuracy and flexural properties of stereolithographically printed resin. *Dental Materials*, vol. 34 (2018), no. 12, pp. e324–e333.
100. LIPSON, Hod and KURMAN, Melba. *Fabricated: The new world of 3D printing.* John Wiley & Sons, 2013.
101. SENTHILKUMARAN, K.; PANDEY, Pulak M. and RAO, PVM. Influence of building strategies on the accuracy of parts in selective laser sintering. *Materials & Design*, vol. 30 (2009), no. 8, pp. 2946–2954.
102. PILIPOVIĆ, Ana; BRAJLIH, Tomaž and DRSTVENŠEK, Igor. Influence of processing parameters on tensile properties of SLS polymer product. *Polymers*, vol. 10 (2018), no. 11, pp. 1208.
103. AJOKU, Uzoma; SALEH, Naguib; HOPKINSON, Neil; HAGUE, R. and ERASENTHIRAN, Poonjolai. Investigating mechanical anisotropy and end-of-vector effect in laser-sintered nylon parts. *Proceedings of the Institution of Mechanical Engineers, Part B: Journal of Engineering Manufacture*, vol. 220 (2006), no. 7, pp. 1077–1086.
104. *Metal 3D Printing Guide: Basics, Costs & Companies.* [2023-07-22]. Available from: https://www.unionfab.com/blog/2023/07/metal-3d-printing. [viewed Apr 26, 2025].
105. PEREIRA, Tanisha; KENNEDY, John V. and POTGIETER, Johan. A comparison of traditional manufacturing vs additive manufacturing, the best method for the job. *Procedia manufacturing*, vol. 30 (2019), pp. 11–18. Available from: https://doi.org/10.1016/j.promfg.2019.02.003..
106. *How Much does a 3D Printer Cost in 2024?* . Available from: https://kingroon.com/es-germany/blogs/3d-printing-guides/how-much-does-a-3d-printer-cost. [viewed Apr 26, 2025].
107. VENTOLA, C. Lee. Medical Applications for 3D Printing: Current and Projected Uses. *P&T (Lawrenceville, N.J.)*, vol. 39 (2014), no. 10, pp. 704–711. Available from: https://www.ncbi.nlm.nih.gov/pubmed/25336867..

108. JOFFE, L. Invisalign(R): early experiences. *Journal of orthodontics*, vol. 30 (2003), no. 4, pp. 348–352. Available from: http://jorthod.maneyjournals.org/cgi/content/abstract/30/4/348..
109. AIMAR, Anna; INNOCENTI, Bernardo and PALERMO, Augusto. The Role of 3D Printing in Medical Applications: A State of the Art. *Journal of Healthcare Engineering*, vol. 2019 (2019), no. 2019, pp. 1–10. Available from: https://search.emarefa.net/detail/BIM-1175251..
110. KALASKAR, Deepak M. *3D Printing in Medicine.* Woodhead Publishing, 2022. Available from: https://books.google.de/books?hl=en&lr=&id=qH9dEAAAQBAJ&oi=fnd&pg=PP1&dq=3D+printing+in+medicine&ots=UZbajz8RZN&sig=wVtauKyVMRlG9v0KM9QtRPf_QuY&redir_esc=y#v=onepage&q&f=false. [viewed May 3, 2025].
111. GARCIA, Justine; YANG, ZhiLin; MONGRAIN, Rosaire; LEASK, Richard L. and LACHAPELLE, Kevin. 3D printing materials and their use in medical education: a review of current technology and trends for the future. *BMJ simulation & technology enhanced learning*, vol. 4 (2017), no. 1, pp. 27.
112. HELGUERO, Carlos G.; MUSTAHSAN, Vamiq M.; PARMAR, Sunjit; PENTYALA, Sahana; PFAIL, John P., et al. Biomechanical properties of 3D-printed bone scaffolds are improved by treatment with CRFP. *Journal of Orthopaedic Surgery and Research*, vol. 12 (2017), pp. 195. Available from: https://www.ncbi.nlm.nih.gov/pmc/articles/PMC5741919/. [viewed May 3, 2025].
113. ASADI-EYDIVAND, Mitra; SOLATI-HASHJIN, Mehran; FARZAD, Arghavan and ABU OSMAN, Noor Azuan. Effect of technical parameters on porous structure and strength of 3D printed calcium sulfate prototypes. *Robotics and Computer-Integrated Manufacturing*, vol. 37 (2016), pp. 57–67. Available from: https://dx.doi.org/10.1016/j.rcim.2015.06.005..
114. KURENOV, Sergei N.; IONITA, Cirprian; SAMMONS, Dan and DEMMY, Todd L. *Three-Dimensional Printing to Facilitate Anatomic Study, Device Development, Simulation, and Planning in Thoracic Surgery.* Atlanta: NewsRx, Jun 3, 2015. Available from: https://search.proquest.com/docview/1683448059..
115. VUKICEVIC, Marija, PhD; MOSADEGH, Bobak, PhD; MIN, James K., MD and LITTLE, Stephen H., MD. Cardiac 3D Printing and its Future Directions. *JACC. Cardiovascular imaging*, vol. 10 (2017), no. 2, pp. 171–184. Available from: https://www.clinicalkey.es/playcontent/1-s2.0-S1936878X16310142..
116. JEON, Hyeryeon; KANG, Kyojin; PARK, Su A.; KIM, Wan D.; PAIK, Seung S., et al. *Generation of Multilayered 3D Structures of HepG2 Cells using a Bio-Printing Technique.* EDITORIAL OFFICE GUT & LIVER, Aug, 2016. Available from: https://repository.hanyang.ac.kr/handle/20.500.11754/75136..
117. RANDAZZO, Michael; PISAPIA, JaredM; SINGH, Nickpreet and THAWANI, JayeshP. 3D printing in neurosurgery: A systematic review. *Surgical neurology international*, vol. 7 (2016), no. 34, pp. 801–S809. Available from: https://www.ncbi.nlm.nih.gov/pubmed/27920940..
118. SAIJO, Hideto; IGAWA, Kazuyo; KANNO, Yuki; MORI, Yoshiyuki; KONDO, Kayoko, et al. Maxillofacial reconstruction using custom-made artificial bones fabricated by inkjet printing technology. *Journal of Artificial Organs*, vol. 12 (2009), no. 3, pp. 200–205. Available from: https://link.springer.com/article/10.1007/s10047-009-0462-7..
119. HUANG, Wenbin and ZHANG, Xiulan. 3D Printing: Print the Future of Ophthalmology. *Investigative ophthalmology & visual science*, vol. 55 (2014), no. 8, pp. 5380–5381. Available from: https://www.ncbi.nlm.nih.gov/pubmed/25159591..
120. CRAFTS, Trevor D.; ELLSPERMAN, Susan E.; WANNEMUEHLER, Todd J.; BELLICCHI, Travis D.; SHIPCHANDLER, Taha Z., et al. Three-Dimensional Printing and Its Applications in

Otorhinolaryngology–Head and Neck Surgery. *Otolaryngology-head and neck surgery*, vol. 156 (2017), no. 6, pp. 999–1010. Available from: https://journals.sagepub.com/doi/full/10.1177/0194599816678372..
121. AURICCHIO, Ferdinando and MARCONI, Stefania. 3D printing: clinical applications in orthopaedics and traumatology. *EFORT Open Reviews*, vol. 1 (2016), no. 5, pp. 121–127. Available from: https://eor.bioscientifica.com/view/journals/eor/1/5/2058-5241.1.000012.xml. [viewed May 3, 2025].
122. CHAE, Michael P.; ROZEN, Warren M.; MCMENAMIN, Paul G.; FINDLAY, Michael W.; SPYCHAL, Robert T., et al. Emerging Applications of Bedside 3D Printing in Plastic Surgery. *Frontiers in Surgery*, vol. 2 (2015), pp. 25–25. Available from: https://www.ncbi.nlm.nih.gov/pubmed/26137465..
123. WILLIAMS, Cylie; JAMES, Alicia; CHAE, Michael P. and HUNTER-SMITH, David J. 3D printing in clinical podiatry: a pilot study and review. *Journal of Foot and Ankle Research*, vol. 8 (2015), no. 2, pp. O41. Available from: https://doi.org/10.1186/1757-1146-8-S2-O41. [viewed May 3, 2025].
124. GUIBERT, Nicolas; MHANNA, Laurent; DIDIER, Alain; MORENO, Benjamin; LEYX, Pierre, et al. Integration of 3D printing and additive manufacturing in the interventional pulmonologist's toolbox. *Respiratory Medicine*, vol. 134 (2018), pp. 139–142. Available from: https://www.sciencedirect.com/science/article/pii/S0954611117304043. [viewed May 3, 2025].
125. ZEIN, Nizar N.; HANOUNEH, Ibrahim A.; BISHOP, Paul D.; SAMAAN, Maggie; EGHTESAD, Bijan, et al. Three-dimensional print of a liver for preoperative planning in living donor liver transplantation. *Liver Transplantation: Official Publication of the American Association for the Study of Liver Diseases and the International Liver Transplantation Society*, vol. 19 (2013), no. 12, pp. 1304–1310. Available from: https://pubmed.ncbi.nlm.nih.gov/23959637/. [viewed May 3, 2025].
126. SOLIMAN, Youssef; FEIBUS, Allison H. and BAUM, Neil. 3D Printing and Its Urologic Applications. *Reviews in Urology*, vol. 17 (2015), no. 1, pp. 20–24. Available from: https://www.ncbi.nlm.nih.gov/pmc/articles/PMC4444770/. [viewed May 3, 2025].
127. HANGGE, Patrick; PERSHAD, Yash; WITTING, Avery A.; ALBADAWI, Hassan and OKLU, Rahmi. Three-dimensional (3D) printing and its applications for aortic diseases. *Cardiovascular Diagnosis and Therapy*, vol. 8 (2018), no. Suppl 1, pp. S19–S25. Available from: https://www.ncbi.nlm.nih.gov/pmc/articles/PMC5949593/. [viewed May 3, 2025].
128. BOGUE, Robert. 3D printing: the dawn of a new era in manufacturing?. *Assembly Automation*, vol. 33 (2013), no. 4, pp. 307–311.
129. LAMICHHANE, Shrawani; BASHYAL, Santosh; KEUM, Taekwang; NOH, Gyubin; SEO, Jo Eun, et al. Complex formulations, simple techniques: Can 3D printing technology be the Midas touch in pharmaceutical industry?. *Asian journal of pharmaceutical sciences*, vol. 14 (2019), no. 5, pp. 465–479.
130. HUANBUTTA, Kampanart; BURAPAPADH, Kanokporn; SRIAMORNSAK, Pornsak and SANGNIM, Tanikan. Practical Application of 3D Printing for Pharmaceuticals in Hospitals and Pharmacies. *Pharmaceutics*, vol. 15 (2023), no. 7, pp. 1877. Available from: https://www.mdpi.com/1999-4923/15/7/1877. [viewed May 3, 2025].
131. FARAH, Shady; ANDERSON, Daniel G. and LANGER, Robert. Physical and mechanical properties of PLA, and their functions in widespread applications—A comprehensive review. *Advanced Drug Delivery Reviews*, vol. 107 (2016), pp. 367–392.

132. TAGAMI, Tatsuaki; HAYASHI, Naomi; SAKAI, Norihito and OZEKI, Tetsuya. 3D printing of unique water-soluble polymer-based suppository shell for controlled drug release. *International journal of pharmaceutics*, vol. 568 (2019), pp. 118494.
133. CHENG, Yiliang; QIN, Hantang; ACEVEDO, Nuria C.; JIANG, Xuepeng and SHI, Xiaolei. 3D printing of extended-release tablets of theophylline using hydroxypropyl methylcellulose (HPMC) hydrogels. *International journal of pharmaceutics*, vol. 591 (2020), pp. 119983.
134. TAGAMI, Tatsuaki; ITO, Erina; KIDA, Risako; HIROSE, Kiyomi; NODA, Takehiro, et al. 3D printing of gummy drug formulations composed of gelatin and an HPMC-based hydrogel for pediatric use. *International journal of pharmaceutics*, vol. 594 (2021), pp. 120118.
135. COHEN, Adir; LAVIV, Amir; BERMAN, Phillip; NASHEF, Rizan and ABU-TAIR, Jawad. Mandibular reconstruction using stereolithographic 3-dimensional printing modeling technology. *Oral Surgery, Oral Medicine, Oral Pathology, Oral Radiology, and Endodontology*, vol. 108 (2009), no. 5, pp. 661–666. Available from: https://www.sciencedirect.com/science/article/pii/S1079210409003680. [viewed May 3, 2025].
136. SING, Swee Leong; AN, Jia; YEONG, Wai Yee and WIRIA, Florencia Edith. Laser and electron-beam powder-bed additive manufacturing of metallic implants: A review on processes, materials and designs. *Journal of Orthopaedic Research: Official Publication of the Orthopaedic Research Society*, vol. 34 (2016), no. 3, pp. 369–385. Available from: https://pubmed.ncbi.nlm.nih.gov/26488900/. [viewed May 3, 2025].
137. HELSEN, Jef A. and BREME, H. J. *Metals as Biomaterials*. Wiley, 1998. Available from: https://books.google.de/books/about/Metals_as_Biomaterials.html?id=a0dRAAAAMAAJ&redir_esc=y. [viewed May 3, 2025].
138. ANDANI, Mohsen Taheri; SHAYESTEH MOGHADDAM, Narges; HABERLAND, Christoph; DEAN, David; MILLER, Michael J., et al. Metals for bone implants. Part 1. Powder metallurgy and implant rendering. *Acta Biomaterialia*, vol. 10 (2014), no. 10, pp. 4058–4070. Available from: https://www.sciencedirect.com/science/article/pii/S1742706114002724. [viewed May 3, 2025].
139. FRAZIER, William E. Metal Additive Manufacturing: A Review. *Journal of Materials Engineering and Performance*, vol. 23 (2014), no. 6, pp. 1917–1928. Available from: https://doi.org/10.1007/s11665-014-0958-z. [viewed May 3, 2025].
140. ROWLEY, Jon A.; MADLAMBAYAN, Gerard and MOONEY, David J. Alginate hydrogels as synthetic extracellular matrix materials. *Biomaterials*, vol. 20 (1999), no. 1, pp. 45–53. Available from: https://www.sciencedirect.com/science/article/pii/S0142961298001070. [viewed May 3, 2025].
141. LARCHER, Alessandro; MUTTIN, Fabio; PEYRONNET, Benoit; DE NAEYER, Geert; KHENE, Zine-Eddine, et al. The learning curve for robot-assisted partial nephrectomy: impact of surgical experience on perioperative outcomes. *European urology*, vol. 75 (2019), no. 2, pp. 253–256.
142. PLOCH, Caitlin C.; MANSI, Chris SSA; JAYAMOHAN, Jayaratnam and KUHL, Ellen. Using 3D printing to create personalized brain models for neurosurgical training and preoperative planning. *World neurosurgery*, vol. 90 (2016), pp. 668–674.
143. MERY, Francisco; ARANDA, Francisco; MÉNDEZ-ORELLANA, Carolina; CARO, Iván; PESENTI, José, et al. Reusable low-cost 3D training model for aneurysm clipping. *World Neurosurgery*, vol. 147 (2021), pp. 29–36.
144. HIGGINS, Monica; LEUNG, Steve and RADACSI, Norbert. 3D printing surgical phantoms and their role in the visualization of medical procedures. *Annals of 3D Printed Medicine*, vol. 6 (2022),

pp. 100057. Available from: https://www.sciencedirect.com/science/article/pii/S2666964122000133. [viewed May 3, 2025].
145. GLYBOCHKO, Peter Vitalevich; RAPOPORT, Leonid Mikhailovich; ALYAEV, Yuri Gennadevich; SIROTA, Eugene Sergeevich; BEZRUKOV, Eugene Alexeevich, et al. Multiple application of three-dimensional soft kidney models with localized kidney cancer: A pilot study. *Urologia Journal*, vol. 85 (2018), no. 3, pp. 99–105.
146. HATAMIKIA, Sepideh; GULYAS, Ingo; BIRKFELLNER, Wolfgang; KRONREIF, Gernot; UNGER, Alexander, et al. Realistic 3D printed CT imaging tumor phantoms for validation of image processing algorithms. *Physica Medica*, vol. 105 (2023), pp. 102512. Available from: https://www.sciencedirect.com/science/article/pii/S1120179722027089. [viewed May 3, 2025].
147. HAZELAAR, Colien; VAN EIJNATTEN, Maureen; DAHELE, Max; WOLFF, Jan; FOROUZANFAR, Tymour, et al. Using 3D printing techniques to create an anthropomorphic thorax phantom for medical imaging purposes. *Medical physics*, vol. 45 (2018), no. 1, pp. 92–100.
148. SRAMEK, Michael; SHI, Yuan; QUINTANILLA, Erick; WU, Xiaotian; PONUKUMATI, Aravind, et al. Tumor phantom for training and research in transoral surgery. *Laryngoscope Investigative Otolaryngology*, vol. 5 (2020), no. 4, pp. 677–682.
149. CAVALIERE, Carlo; BALDI, Dario; BRANCATO, Valentina; AIELLO, Marco and SALVATORE, Marco. A customized anthropomorphic 3D-printed phantom to reproducibility assessment in computed tomography: an oncological case study. *Frontiers in Oncology*, vol. 13 (2023). Available from: https://www.frontiersin.orghttps://www.frontiersin.org/journals/oncology/articles/10.3389/fonc.2023.1123796/full. [viewed May 3, 2025].
150. OH, Se An; KIM, Min Jeong; KANG, Ji Su; HWANG, Hyeon Seok; KIM, Young Jin, et al. Feasibility of Fabricating Variable Density Phantoms Using 3D Printing for Quality Assurance (QA) in Radiotherapy. *Progress in Medical Physics*, vol. 28 (2017), no. 3, pp. 106–110. Available from: http://click.ndsl.kr/servlet/LinkingDetailView?cn=JAKO201733348352101&dbt=JAKO&org_code=O481&site_code=SS1481&service_code=01..
151. DANCEWICZ, O. L.; SYLVANDER, S. R.; MARKWELL, T. S.; CROWE, S. B. and TRAPP, J. V. Radiological properties of 3D printed materials in kilovoltage and megavoltage photon beams. *Physica Medica*, vol. 38 (2017), pp. 111–118. Available from: https://www.clinicalkey.es/playcontent/1-s2.0-S1120179717301643..
152. QIU, Jianfeng; HOU, Kun; DYER, Brandon A.; CHEN, Jyh-Cheng; SHI, Liting, et al. Constructing Customized Multimodal Phantoms Through 3D Printing: A Preliminary Evaluation. *Frontiers in Physics*, vol. 9 (2021). Available from: https://www.frontiersin.orghttps://www.frontiersin.org/journals/physics/articles/10.3389/fphy.2021.605630/full. [viewed May 8, 2025].
153. VILLANI, D.; RODRIGUES, O. and CAMPOS, L. L. Dosimetric characterization of 3D printed phantoms at different infill percentages for diagnostic X-ray energy range. *Radiation Physics and Chemistry*, vol. 172 (2020), pp. 108728. Available from: https://www.sciencedirect.com/science/article/pii/S0969806X19309223. [viewed May 8, 2025].
154. LANARO, Matthew; LUU, Amelia; LIGHTBODY-GEE, Archibald; HEDGER, David; POWELL, Sean K., et al. Systematic design of an advanced open-source 3D bioprinter for extrusion and electrohydrodynamic-based processes. *The International Journal of Advanced Manufacturing Technology*, vol. 113 (2021), no. 9, pp. 2539–2554. Available from: https://doi.org/10.1007/s00170-021-06634-1. [viewed May 3, 2025].

155. HOLLISTER, Scott J. and WEATHERWAX, Kevin J. Regulatory Considerations in the Design and Manufacturing of Implantable 3D-Printed Medical Devices.
156. PUGLIESE, Raffaele; BELTRAMI, Benedetta; REGONDI, Stefano and LUNETTA, Christian. Polymeric biomaterials for 3D printing in medicine: An overview. *Annals of 3D Printed Medicine*, vol. 2 (2021), pp. 100011. Available from: https://www.sciencedirect.com/science/article/pii/S2666964121000060. [viewed May 3, 2025].
157. DI PRIMA, Matthew; COBURN, James; HWANG, David; KELLY, Jennifer; KHAIRUZZAMAN, Akm, et al. Additively manufactured medical products–the FDA perspective. *3D printing in medicine*, vol. 2 (2016), pp. 1–6.
158. Kenny Dalgarno. The Impact and Potential for 3D Printing and Bioprinting in the Medical Devices Industry. *Medical Device white paper series*, pp. 1–25.
159. HOURD, Paul; MEDCALF, Nicholas; SEGAL, Joel and WILLIAMS, David J. A 3D bioprinting exemplar of the consequences of the regulatory requirements on customized processes. *Regenerative medicine*, vol. 10 (2015), no. 7, pp. 863–883.
160. *EU Medical Device Coordination Group Questions and Answers on Custom-made Devices & Considerations on Adaptable Medical Devices and Patient-Matched Medical Devices.*
161. PETTERSSON, Ante B. V.; BALLARDINI, Rosa Maria; MIMLER, Marc; LI, Phoebe; SALMI, Mika, et al. Core Legal Challenges for Medical 3D Printing in the EU. *Healthcare*, vol. 12 (2024), no. 11, pp. 1114. Available from: https://www.ncbi.nlm.nih.gov/pmc/articles/PMC11171897/. [viewed May 3, 2025].
162. *Polymethyl Methacrylate (PMMA) | Britannica.* [2025-04-22]. Available from: https://www.britannica.com/science/polymethyl-methacrylate. [viewed May 5, 2025].
163. *Ultimate Guide to PMMA/Acrylic Filament 3D Printing - 3DSourced.* [2023-03-29]. Available from: https://www.3dsourced.com/rigid-ink/pmma-filament-acrylic/. [viewed May 5, 2025].
164. ANTONOVIC, Laura; GUSTAFSSON, Håkan; ALM CARLSSON, Gudrun and CARLSSON TEDGREN, Åsa. Evaluation of a lithium formate EPR dosimetry system for dose measurements around Ir-192 brachytherapy sources. *Medical physics (Lancaster)*, vol. 36 (2009), no. 6, pp. 2236. Available from: https://urn.kb.se/resolve?urn=urn:nbn:se:liu:diva-19422..
165. *Specification of Zortrax M Series 3D Printers | Zortrax Support Center*. [2016-07-07]. Available from: https://support.zortrax.com/m-series-specification/. [viewed May 5, 2025].
166. BUPPHATHONG, Sasinan; QUIROZ, Carlos; HUANG, Wei; CHUNG, Pei-Feng; TAO, Hsuan-Ya, et al. Gelatin Methacrylate Hydrogel for Tissue Engineering Applications—A Review on Material Modifications. *Pharmaceuticals*, vol. 15 (2022), no. 2, pp. 171. Available from: https://www.ncbi.nlm.nih.gov/pmc/articles/PMC8878046/. [viewed May 15, 2025].
167. NACU, Isabella; BERCEA, Maria; NIȚĂ, Loredana Elena; PEPTU, Cătălina Anișoara; BUTNARU, Maria, et al. 3D bioprinted scaffolds based on functionalized gelatin for soft tissue engineering. *Reactive and Functional Polymers*, vol. 190 (2023), pp. 105636. Available from: https://www.sciencedirect.com/science/article/pii/S1381514823001396. [viewed May 15, 2025].
168. SOUFIVAND, Anahita Ahmadi and BUDDAY, Silvia. Predicting the hyperelastic properties of alginate-gelatin hydrogels and 3D bioprinted mesostructures. *Scientific Reports*, vol. 13 (2023), no. 1, pp. 21858. Available from: https://www.nature.com/articles/s41598-023-48711-3. [viewed May 15, 2025].
169. LUKIN, Izeia; EREZUMA, Itsasne; MAESO, Lidia; ZARATE, Jon; DESIMONE, Martin Federico, et al. Progress in Gelatin as Biomaterial for Tissue Engineering. *Pharmaceutics*, vol. 14 (2022), no. 6, pp. 1177. Available from: https://www.mdpi.com/1999-4923/14/6/1177. [viewed May 15, 2025].

170. ECHAVE, Mari C.; SAENZ DEL BURGO, Laura; PEDRAZ, Jose L. and ORIVE, Gorka. Gelatin as Biomaterial for Tissue Engineering. *Current Pharmaceutical Design*, vol. 23 (2017), no. 24, pp. 3567–3584. Available from: https://pubmed.ncbi.nlm.nih.gov/28494717/. [viewed May 15, 2025].
171. MCGARRY, Conor K.; GRATTAN, Lesley J.; IVORY, Aoife M.; LEEK, Francesca; LINEY, Gary P., et al. Tissue mimicking materials for imaging and therapy phantoms: a review. *Physics in medicine & biology*, vol. 65 (2020), no. 23. Available from: https://www.ncbi.nlm.nih.gov/pubmed/32998112..
172. MA, Xiangjie; FIGL, Michael; UNGER, Ewald; BUSCHMANN, Martin and HOMOLKA, Peter. X-ray attenuation of bone, soft and adipose tissue in CT from 70 to 140 kV and comparison with 3D printable additive manufacturing materials. *Scientific Reports*, vol. 12 (2022), no. 1, pp. 14580. Available from: https://www.nature.com/articles/s41598-022-18741-4. [viewed May 15, 2025].